Inclined plunging jet

R.M. Keij

Study of an inclined plunging jet
and its velocity profile at increasing water depths

TU Delft

Inclined plunging jet

by

R.M. Keij

to obtain the degree of Master of Science
at the Delft University of Technology,
to be defended publicly on Tuesday May 30, 2023 at 01:00 PM.

Student number:	4440072	
Project duration:	May 27, 2022 – May 30, 2023	
Thesis committee:	Dr. ir. A.J Nobel	Boskalis
	Dr. ir. A.M Talmon	TU Delft, supervisor
	Prof. dr. ir. C. van Rhee,	TU Delft
	Dr. ir. G.H Keetels	TU Delft

TU Delft

Preface

This thesis represents months of research, analysis, and the jetting of water in a closed circuit, most of it in the comfort of my cozy little office as pictured below. It has been a very interesting journey from which I learned a lot about the undertaking and timely execution of experiments. With this thesis, I aim to contribute to the engaging world of water jets and their subsequent erosion.

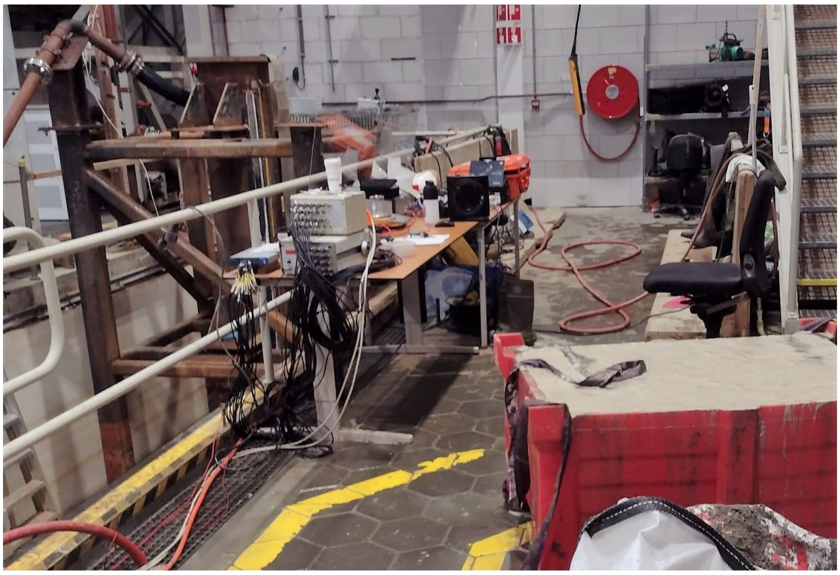

For the support during the entire process, which is condensed into this report, I would like to thank Arno Nobel, for providing me with guidance, feedback, insightful remarks, and for the many hours he spent helping me while working in the laboratory, both on the shore and in the flume.

I would also like to thank Mark van Biesheuvel, who was part of the brainstorming and the execution of some tests described in this report. Finally, I would like to express my appreciation to Arno Talmon and Cees van Rhee for being involved and joining in reflecting on the data.

Thank you all for your invaluable contributions to this thesis and for your support throughout my academic journey.

R.M. Keij
Papendrecht, May 2023

Abstract

This report aims to determine the optimal settings for the most efficient removal of sand adhering to the side of a dredging vessel where a water pool has formed on top. In the tests the scenario of an inclined jet traveling through the air, then continuing some distance underwater, and then eroding sand was reproduced. Where air was entrained into the jet in air and creates an air sheath around the jet when the waterline is penetrated. The velocity of the jet at different water depths was determined using the measured stagnation pressure and density, by use of a pitot tube and conductivity sensors respectively. This was done for four different set-ups under a 40-degree angle; one which had 1.80 meters of straight pipe upstream of the nozzle (straight), one with an S-bend after 0.8 meters, and then the other 1 meter of pipe before the nozzle (middle bend), one with the S-bend directly before the nozzle (end bend) and the last one again entirely straight but with an inclined rubber flap covering the nozzle (flap). From these four set-ups, the velocity was determined at the possible erosion locations, using the literature the erosion velocity at these water depths was calculated. As shown in Figure 1 the velocities of the different jets are clustered in two groups, both following a plotted trend line. The best set-up is a straight jet with a slightly larger velocity than the middle bend set-up. At larger depths, the performance of these two seemed 50% higher than that of the end bend and flap set up.

The velocity of the two worse-performing jets might have been overestimated due to interpretation issues of the velocity at low water percentage, which was significantly more present in the two lower-performing jets than in the two best-performing jets. Further research is needed to interpret the conductivity sensors more accurately and create a more detailed velocity profile.

A secondary test was done where the erosion of the entirely straight set-up was determined with a submerged sand container at increasing water depths. The measured erosion was approached most accurately by [van Rijn et al., 2019]. It was theorized that the increase in entrained air would reduce the erosion velocity of the jet, but this turned out not to be the case.

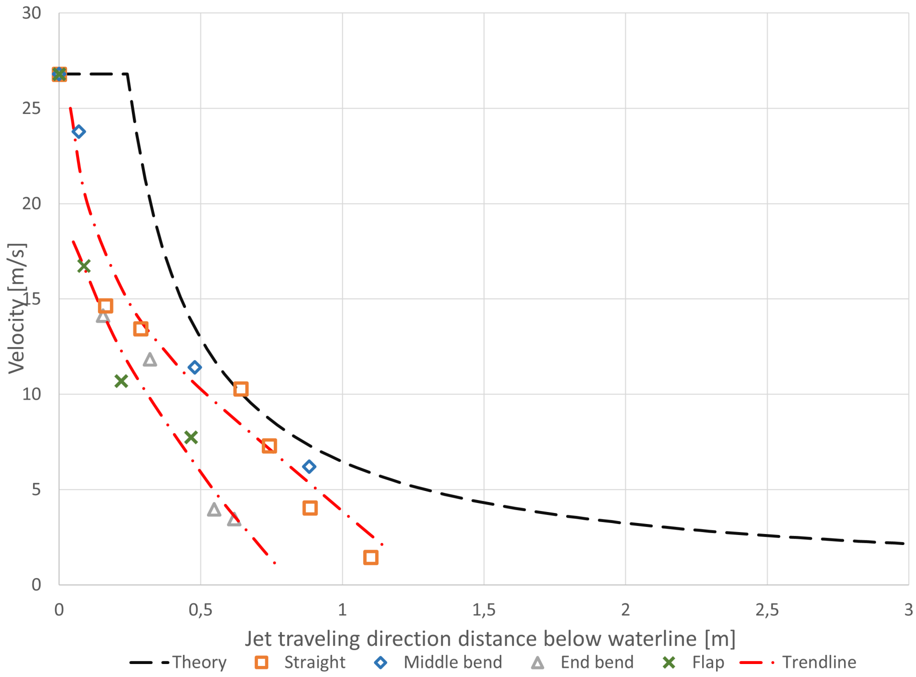

Figure 1: Flow velocity in the four set-ups under water

Nomenclature

α	Dimensionless empirical parameter	[-]
Δ	Specific density	$[-]$
ϵ	Percentage of conducting liquid	$[\frac{kg}{m^3}]$
μ	Dynamic viscosity of the fluid	$[\frac{kg}{m*s}]$
ϕ'	Modified pick up flux	$[-]$
ϕ_p	Pick-up flux	$[-]$
ρ_g	Density of the gas	$[\frac{kg}{m^3}]$
ρ_s	Density of the sand	$[\frac{kg}{m^3}]$
ρ_w	Density of the water	$[\frac{kg}{m^3}]$
σ	Surface tension	$[\frac{N}{m}]$
$\sigma_{carrier}$	Conductivity of the carrier fluid	$[-]$
σ_{eff}	Conductivity of the mixture	$[-]$
σ_{Liquid}	Conductivity of the liquid	$[-]$
σ_m	Conductivity of the mixture	$[-]$
τ_b	Bed shear stress	$[\frac{N}{m^2}]$
θ	Shields parameter	[-]
θ_{cr}	Critical shields parameter	[degrees]
θ_j	Angle of the jet at the waterline	[degrees]
θ_n	Angle of the nozzle	[degrees]
c_b	Near bed concentration	$[-]$
C_d	Empirical parameter	$[-]$
C_L	Coherence length of a jet	$[m]$
c_{sand}	Volumetric concentration of sand	$[-]$
C_t	In situ electrical conductivity of a porous rock	$[\frac{kg}{m^3}]$
C_w	Fluid saturation	$[-]$
D	Particle parameter	$[m]$
D^*	Local width of the jet	$[m]$
D_*	Dimensionless particle parameter	$[-]$
D_{10}	Particle size for which 10 percent is finer	$[m]$

D_{15}	Particle size for which 15 percent is finer	$[m]$
D_1	Diameter of a sheath around a plunging jet	$[m]$
D_2	Depth of a sheath parallel to a plunging jet	$[m]$
D_{50}	Median particle size	$[\mu m]$
D_j	Diameter of the jet at the waterline	$[m]$
D_n	Diameter of the nozzle	$[m]$
D_p	Diameter of the inlet pipe	$[m]$
E	Pick up flux	$[\frac{kg}{m^2 s}]$
f	Friction factor	$[-]$
F_*	Densiometric Froude number	$[-]$
Fr	Froude number	$[-]$
g	Gravitational acceleration	$[\frac{m}{s^2}]$
H_n	Height of the nozzle above the waterline	$[m]$
H_p	Theoretical bubble depth	$[m]$
I	Theoretical bubble depth	$[\frac{kgm}{s}]$
k	Sand permeability	$[\frac{m}{s}]$
k_0	Turbulence kinetic energy	$[\frac{kgm^2}{s^2}]$
L	Distance from the jet nozzle	$[m]$
L_a	Aeration length of the jet	$[m]$
L_b	Break up length	$[m]$
L_o	Break up onset location	$[m]$
M_s	Mass flux	$[\frac{kg}{s}]$
n_0	Porosity of the settled original bed	$[-]$
N_f	Nozzle factor	$[-]$
n_x	Scaling factor of different parameters	$[-]$
P	Production	$[\frac{m^3}{s}]$
p	Pressure	$[\frac{N}{m^2}]$
Q_w	Water discharge at jet nozzle	$[\frac{m^3}{s}]$
r_i	Initial radius	$[m]$
R_p	Particle Reynolds number	$[-]$
r_r	Resulting radius	$[m]$
Re	Reynolds number dependent on diameter	$[-]$

Re_L	Reynolds number dependent on length	$[-]$
S	Settling flux	$[\frac{kg}{m^2 s}]$
t	Time	$[s]$
t_p	Pinch off time	$[s]$
Tu_0	Turbulence intensity	$[-]$
u	Velocity	$[\frac{m}{s}]$
U_0	Nozzle exit velocity	$[\frac{m}{s}]$
v	Kinematic viscosity	$[\frac{m^2}{s}]$
V_b	Jet velocity at the bottom of the pool	$[\frac{m}{s}]$
v_e	Erosion velocity	$[\frac{m}{s}]$
V_j	Jet velocity at the waterline	$[\frac{m}{s}]$
V_m	Jet velocity below the waterline	$[\frac{m}{s}]$
V_n	Jet velocity at the nozzle	$[\frac{m}{s}]$
w_s	Settling velocity	$[\frac{m}{s}]$
We	Weber number	$[-]$
x	Horizontal distance from nozzle	$[m]$
y	Vertical distance below the waterline	$[m]$

Contents

1

Intro

The adherence of sand to the side of the hopper can increase the dumping time of a hopper vessel due to the water jet not being as effective as possible because of pools forming on top of the sand banks.

1.1. Problem analysis

Water jetting is often used to loosen or remove sand quite effectively. A lot of research has already been done on using submerged water jets to erode sand. This is why it is also used in different, partially submerged circumstances where sand needs to be removed, like jetting in air or a plunging jet.

During the dumping process of a hopper, the doors will open and a lot of the sand will fall out. Since not the entire bottom of the vessel can be opened there are some inclined walls where sand remains after opening the doors. This sand can be removed by using water jets to loosen it from the inclined wall. Some of the sand sticks to the side and makes a sandbank that can endure a lot of water pressure before it succumbs under the exerted force. Simply increasing the water pressure is not always an option to speed up the removal of these sandbanks. To determine the limiting factor, the erosion effect of the jet on sand should be studied. With the size of the hopper increasing the size of the wall where the sand can adhere to also increases. The sand can accumulate at a further distance from the jet, requiring the length over which the jet exerts pressure to increase as well. Making the efficient removal of clinging sand more relevant with increasing hopper sizes.

Since the information available in the literature is not enough to cover this entire process test will have to be done to gather more data. Applying CFD to this project would have been too complex due to the impact of the jet into the sand after plunging into the water. Which would have a lot of particles in play making CFD quickly too complex to apply. This is why the parameters will be measured using laboratory testing. After determining the effect of these parameters in a scaled laboratory test, the aim is to find a model that can accurately predict the erosion velocity of the sand by the plunging jet.

1.2. Problem statement

Removing the sand stuck to the side of a hopper with a jet is relatively time-consuming. Because the sand offers a lot of resistance against the incoming water jets. This process can be sped up and, if done more effectively, reduce the time required for the dumping process.

1.3. Objective

The objective of this research is to be able to accurately predict the erosion effectiveness of an inclined plunging jet in a hopper were there is a layer of water on top of the sand. This will be done by measuring different parameters from an experimental laboratory set-up. Four different flow configurations that imitate certain aspects present in the vessel are tested.

1.4. Research questions

The goal of this research is to find out how the main parameters of an angled plunging jet develop over its course. This raises the question:

- What are the values of the flow velocity, stagnation pressure, and jet momentum of a plunging jet in a hopper when it reaches the sand depending on the jet configuration?

This question is split in three more concrete questions. These three questions are about the trajectory and upstream conditions of the jet:

- What is the influence of a bend upstream of the nozzle on the flow velocity of the jet after the nozzle?
- How does an inclined flap covering the nozzle influence the flow velocity?
- What happens to the velocity evolution of the jet when it penetrates the waterline?
- What is the influence of a water layer on top of the sand on the jet production?

Four different flow configurations that vary upstream from the nozzle can help to answer these questions.

2

Prototype Jet

Figure 2.1: Sand erosion by jets in the prototype

The current jet system which motivated this research consists of multiple parallel jets, attached to the side of the vessel as visible in Figure 2.1. In this image, it is visible that the jets are turned on jetting water into sand. The jets are situated along the length of the vessel and are positioned somewhat close to each other. The water jets have a wall below them with an incline between 30 to 45 degrees. The nozzle of the jet, which has a diameter of 4 to 6 centimeters, is covered by a lid that is pushed aside by the force of the water expelled from the nozzle. The water at the nozzle exit has a pressure between 4 to 10 bar, which corresponds to a velocity between 30 to 50 meters per second. First, the jet leaves the nozzle, where the geometry of the nozzle influences the jet exit velocity, *a* in Figure 2.2. Then the jet passes a certain distance through the air, *b*, where it entrains air. After traveling through the air it will break up at a certain distance from the nozzle, *c*. After which it will hit the water surface which it has to penetrate, at location *d*. Which will cause bubbles to form, as visible at location *e*. Then the jet will continue its path through the water, *f*, until it makes contact with the sand it has to erode, as shown in the figure at location *g*. The distance it needs to cover in air and water can differ depending on where the sand sticks to the side of the hopper and the amount of water building up on top of the sand. With a total distance of 15 meters, the most likely distance is between three and ten meters with a water height between one and two meters. The erosion speed of the jet depends on the sand and jet parameters at the location where erosion takes place. The water jet parameters at the nozzle are the fluid density, jet pressure, nozzle diameter, and nozzle discharge. Which are parameters that can be determined beforehand. The jet parameter which has to be measured at the sand is the jet velocity. With the pressure the flow velocity can be determined which then can be used to determine the resulting shear stress. The sand parameters that are needed are; the particle size distribution, the density, and the in situ porosity of the bed. Combining these parameters the erosion speed of the jet in this sand can be mathematically determined. The fluid density at the nozzle of the jet is pure water, as the jet covers more distance and entrains more air the average density of the jet drops since the density of the entrained air is much lower than that of the water, reducing the average density. The discharge in the air also increases the total volume due to air entrainment. The velocity profile changes with the distance decreasing from the maximum velocity at the nozzle to the final eroding velocity at the sand. The jet velocity is highest at the center of the jet, where it will stay equal to the nozzle exit velocity for a short period, after which the jet is fully developed and the velocity in the center line will decrease, [Rajaratnam and Albers, 1998].

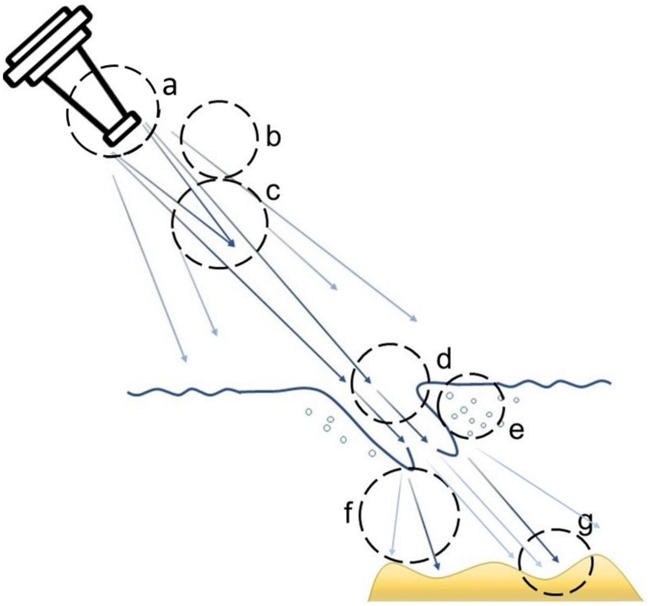

Figure 2.2: Schematic overview of a plunging jet

3

Literature review

A lot of aspects will have an impact on jet development. The jet has multiple different stages it passes through over its trajectory and all of them influence the jet in some way. Knowing the implications of these elements helps to define and set up the experiment. In this chapter, the impact of these factors is discussed.

3.1. Nozzle geometry

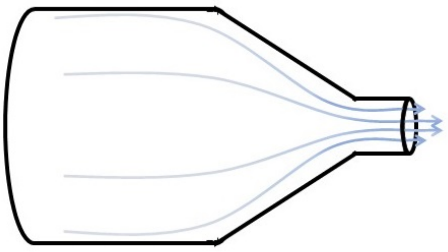

Figure 3.1: Schematic drawing of a fire hose nozzle

The geometry of the nozzle determines the fluid velocity and flow pattern at the exit before the water jet plunges into the air. The nozzle can increase or decrease in diameter near the end which can either increase or decrease the pressure and consequently the velocity. The geometry of the jet can also influence the turbulence of the exiting water and thereby impact the coherence and possible functional jetting distance of the water jet. The jet nozzle from a fire hose, as shown in Figure 3.1, is designed in such a way that due to the contraction of the flow in the nozzle, the pressure increases at the tip and causes the exit velocity of the jet to be larger than if the diameter didn't decrease. The nozzle in the actual hopper looks relatively like that of a fire hose.

A possible influential factor of the nozzle in the hopper is the 90-degree angle in the pipes just before the start of the nozzle. The bend the water has to turn causes the jet to be turbulent before it exits the nozzle. The jet in the hopper also has to push aside a lid that is connected to the top of the nozzle. This lid can also influence the coherence of the jet and the distance it can travel. Since the geometry of the nozzle plays such an important role concerning the parameters of the exiting water jet it should also be taken into account. Changing the geometry of the nozzle will influence the parameters of the jet over its trajectory.

3.2. Air entrainment

The entrainment of air into the water jet can reduce the jet velocity and reduces the coherence of the jet, which will decrease the eventual impact of the jet. The jet in question has a wall right below it which decreases the entrainment from that side compared to the other sides of the jet. The jet might tend to approach the wall due to the Coanda effect, which causes fluid jets to follow adjacent flat surfaces. The jet entrainment at the wall side becomes zero when the jet actually hits the wall and will also reduce the velocity of the jet because of the resulting shear stress of the wall on the water jet. The amount of air entrainment of a plunging liquid jet was visually determined [Roy and Kumar, 2018] and was observed to depend on the jet velocity, nozzle diameter, and jet length. The amount of air entrained into the jet increases its diameter. The local diameter at a certain distance from the nozzle can be determined using Formula 3.1.

$$\frac{D^*}{D_n} = 0.125(WeRe_L)^{\frac{1}{6}} \qquad Re_L = \frac{\rho_w u L}{\mu} \qquad We = \frac{\rho_w u^2 L}{\sigma} \tag{3.1}$$

Where We is the Weber number, Re_L is the Reynolds number dependent on the distance traveled, D^* is the average diameter at distance L, μ is the dynamic viscosity and D_n is the diameter at the nozzle, [van de Sande, 1974]. The equation gives the average diameter of a turbulent jet as a function of Reynolds and Weber. Reynolds and Weber's numbers play a role in the inertial and viscous forces and the surface tension. All of these play important roles in the distance over which the jet stays cohesive.

3.3. Incoming angle

The direction and the pressure of the jet while plunging are influenced by its angle with respect to the horizontal. At shallow angles, the air entrainment is larger than at steep angles due to the contact surface of the jet with the water, with maximum air entrainment occurring at 10 degrees. When the jet comes in under a small angle compared to the waterline, the jet center can be deflected by the water's surface. At incoming angles above 25 degrees with respect to the waterline, the jet remains cohesive enough to penetrate well below the free surface. Whereas water jets with smaller angles have more trouble piercing the waterline and won't penetrate nearly as deep. This was tested using numerical simulation by [Deshpande and Trujillo, 2013]. Where the air volume due to penetration of the waterline by a water jet could be determined up to three centimeters below the waterline. The air entrainment was reduced for an increasing angle. The air entrainment for a plunging jet with an angle of 45 degrees was about 5 times smaller in comparison with jets of 15 degrees or less.

3.4. Distance in air

The distance the jet has to cover should be less than the 'break-up length' of the jet to not lose a significant amount of momentum during the waterline penetration. The break-up length, L_b, is the length at which the water jet splits up from a coherent jet into a shower of small droplets, and thereby loses much of its impact velocity. The break-up length depends on the velocity and the governing process as shown in Figure 3.2. Where the break-up length of a jet is given as a function of the jet velocity. In this figure multiple regions are visible where the break-up length depends on the properties of the jet. The relation for the break up length in the turbulent region is given in Formula 3.2,by [Lubking, 2000].

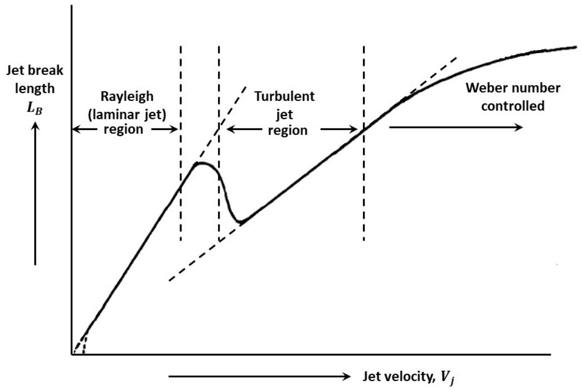

Figure 3.2: Break-up length, [Lubking, 2000]

$$L_b = 320 V_n D_n^{1.5} \tag{3.2}$$

Besides a loss in impact velocity, surpassing the break up length causes more air entrainment into the water. Since the jet reaches the water surface as an lot of individual water particles, all of which will entrain air into the water, so the total air entrainment into the water will be larger than that of a single cohesive jet. This also influences the further velocity development of the jet. The break up happens due to instabilities at the moment of discharge and the effects of air resistance on the water jet. Before the jet reaches its breakup length the jet will have an increasingly sinusoidal movement around the center of the initial jet at the nozzle. When the amplitude of the sinusoidal movement gets too large the jet won't be able to return to the normal and will fall apart. As shown in Figure 3.2 the break up length of the jet increases almost linearly with jet velocity in the turbulent region, [Van de Sande and Smith, 1976]. The actual jet in question has a high enough jet velocity that it is located in the Weber number controlled region instead of the turbulent jet region, which causes the break-up length to become more complex. This means that the break-up length in Formula 3.2 doesn't hold anymore. With high velocity jets the surface tension of the circumference of the jet and the air friction the jet experiences should both be taken into account. As opposed to jets with a lower velocity where these processes aren't as important This makes it difficult to find a simple accurate mathematical expression to define where in the trajectory the jet surpasses the break-up length.

The break-up length used to estimate the coherent travel distance of the jet was defined by [Grant and Middleman, 1966] as *'the length of the fluid jet from the point of exit from the nozzle, to a point at which the disturbances within the fluid jet reach the same radius as the initial nozzle opening'*. Which is shown as the c_L distance in Figure 3.3

$$\frac{C_L}{D_n} = 8.51(We^{0.5})^{0.64} \tag{3.3}$$

The formula for the jet coherence length for turbulent jets is given in equation 3.3. Where it is based on a line through the data of [Grant and Middleman, 1966]. This equation doesn't take the nozzle design into account which was added later by [Morgan and Baines-Jones, 2009] in the way of the nozzle factor N_f resulting in Formula 3.4. The nozzle factor depends on the nozzle material, exit edge sharpness, body shape and entry and exit diameter.

$$\frac{C_L}{D_n} = 8.51(We^{0.5})^{0.64}(N_f) \tag{3.4}$$

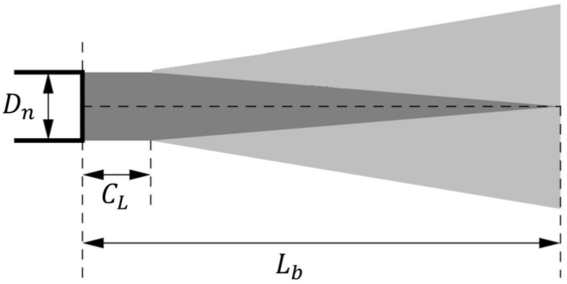

Figure 3.3: Break-up length variables, [Trettel, 2020]

A lot of the previously done research on break-up lengths has been compiled into one paper [Trettel, 2020]. The papers that are mentioned earlier are also part of his review of research into break-up lengths. The break-up length in the paper of B. Trettel is defined as *'the time-averaged distance from the nozzle where the diameter of the jet core reduces to zero'*, as shown in Figure 3.3 by the parameter L_b. The average breakup onset location, L_o, is defined as the time-averaged distance from the nozzle where the decrease of jet center velocity first occurs. In his paper, the results of the earlier research are compared and inconsistencies are highlighted. Noticeably a lot of earlier research doesn't highlight certain influential aspects of the setup that impact the break-up length. The turbulence intensity in most referenced papers is absent. This parameter can have a significant influence on the breakup length of the jet.

Regime name	Appearance
Dripping	Slow formation of droplets at the nozzle outlet
Laminar Rayleigh	Symmetric break up into large droplets
Downstream transition	Varies from Rayleigh-like to abrupt breakup
Turbulent Rayleigh	Similar to laminar Rayleigh but turbulent
Turbulent surface breakup	small surface disturbances causing breakup
Atomization	Larger spray angle than turbulent surface breakup

Table 3.1: Regimes and visual characteristics

Five different break-up regimes to determine the way of the break-up of the jet are specified in the paper. The regimes and their visual appearances are described in Table 3.1. The breakup lengths for four of these regimes are plotted in Figure 3.4 for a nozzle diameter of 6mm. The dripping regime is absent in this figure since that is mostly for air-water systems. The location of the borders between the regimes can be calculated using the Weber number, We_{l0}, [Trettel, 2020]. The formulas for the break-up length inside the regimes are a function of the net turbulence intensity, Tu_0, which is typically between 1 and 10%. It depends on the rate of the turbulence kinetic energy, k_0, over the velocity profile in the x-direction, U_0. This is shown in Formula 3.5.

$$\overline{Tu_0} = \sqrt{\frac{2k_0}{3U_0}} \qquad We_{l0} = \frac{\rho_l \overline{U_0^2} D_n}{\sigma} \tag{3.5}$$

The regime of the actual jet is most likely the atomization regime. This is because of the high Weber number due to the large velocity of the jet in combination with the large Reynolds number. In the atomization regime the diameter of the droplets around the jet core are much smaller than the nozzle outlet diameter. The breakup onset location is small and the breakup length plateaus with increasing jet velocity. The breakup length of this regime is given in Formula 3.6 which followed from a fit over measured data by [Trettel, 2020], where ρ_g is the density of the gas, which in this case is the density of air.

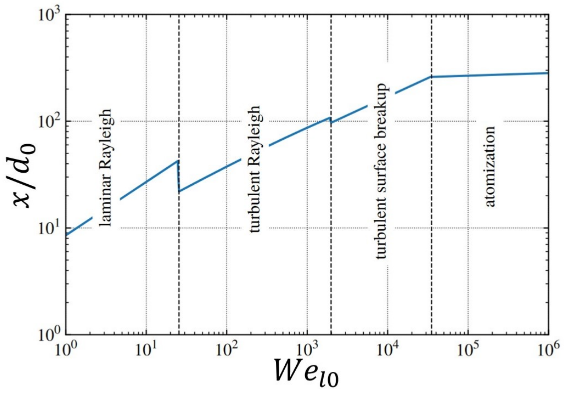

Figure 3.4: Break-up length regimes d_0=6mm, [Trettel, 2020]

$$\frac{x}{D_n} = 5.31\overline{Tu_0}^{-0.568}\frac{\rho_l}{\rho_g} \tag{3.6}$$

The jet is most likely in the turbulent atomization regime, not only due to the speed of the jet but also due to the swirl created due to the bend the jet has to turn before exiting the nozzle. This induces turbulence in the flow. Since the jet will decrease when it reaches turbulence in air it might be beneficial for the jet to be turbulent before exiting the jet nozzle. This seems counter intuitive but the change from laminar to turbulent in air has a significant negative effect on the break up length. When the jet is already turbulent this wont happen making the break up length larger. Which is what happens when the jet is in the atomization regime. The formula for the break up length in the turbulent surface breakup regime is given in Formula 3.7, which B.Trettel based on data of significantly turbulent jets.

$$\frac{x}{D_n} = 3.61\overline{Tu_0}^{-0.275}We_{l0}^{0.334} \tag{3.7}$$

When calculating the We_{l0} the breakup regime can be determined with the corresponding formula for break-up length. As shown in Figure 3.4 the break-up length plateaus at a certain Weber number making a further increase in velocity not correspond with an increase in breakup length.

3.5. Waterline penetration

The velocity at the impact location of the jet, V_j, is given in Formula 3.8, where the formula is determined using projectile motion, [van de Sande, 1974]. With V_n the jet velocity at the nozzle and H_n is the height of the nozzle above the waterline. This formula holds as long as the covered distance of the jet is less than the break up length, otherwise a different formula has to be used which is accompanied by a significant decrease in velocity.

$$V_j = \sqrt{V_n^2 + 2gH_n} \tag{3.8}$$

The incoming angle of the plunging jet compared to the waterline can be calculated using Formula 3.9, an adaptation of a particle motion parabola. Where θ_n and V_n are respectively the angle and velocity at the jet nozzle. The t in this formula is the time passed between exiting the nozzle and hitting the waterline, [van de Sande, 1974].

$$g\theta_j = \frac{\sqrt{V_n^2 sin^2(\theta_n) + 2gH_n}}{V_n cos(\theta_n) t} \tag{3.9}$$

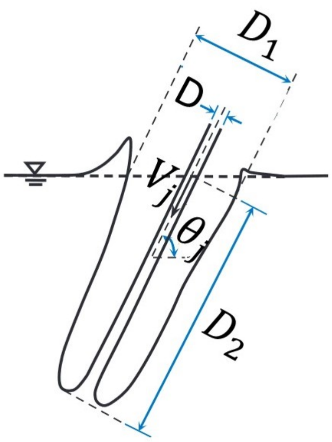

Figure 3.5: Schematic overview of plunging jet with air cavity, [Sun et al., 2020]

At high velocities, the shear of the plunging jet and the surrounding air creates a boundary layer around the jet, which will move with the jet while piercing the waterline, [Biń, 1993]. Making an air film around the jet while it penetrates the waterline is beneficial for velocity preservation. The jet has a constant momentum, which depends on the total mass times the velocity. So when the mass increases the velocity decreases. When air instead of water entrains into the jet the mass increase is smaller, consequently the velocity decrease is lower. Having an air film around the jet while penetrating delays the water entrainment and that way delays the velocity decrease. The entrainment of water into the water jet is much more detrimental to the velocity of the jet than the entrainment of air into the water jet. Having an air film around a jet leads to a slower decrease in velocity at the center line of the jet compared to a jet without an air film. Due to the mass of the entrained substance being lower, the velocity profile has a comparably higher center line velocity and a smaller jet width over which the velocity profile is spread. In a set-up where air was discharged around a submerged water jet, by [Vinke, 2009], the air film around it had a constant center line velocity of up to 36 diameters. This was achieved with a nozzle diameter of 30mm. The air film is present for 24 nozzle diameters compared to 6 nozzle diameters for a jet without an added air film. The length of the air film around the jet in the set-up of Vinke was dependent on the air discharge, water jet velocity, and nozzle diameter. These parameters are not the same or not present, in the case of air discharge, in the actual jet compared to the jet from Vinke. This does show that the air film formed around the jet while plunging is beneficial for increasing the distance over which the jet loses velocity. The very thin air film formed around the jet during waterline penetration prevents contact between the water jet and the surrounding water, as shown in Figure 3.5. If the water in the jet is too turbulent the disturbances at the surface of the water jet penetrates the thin air film and comes into contact with the surrounding water causing the air film to collapse. Using Formula 3.10 the length and width of the sheath around the penetrating jet can be calculated, [Sun et al., 2020].

$$\frac{D_1}{D_j} = 0.13(\frac{tV_j}{D_j})^{0.3}(\frac{t}{t_p})^{0.02}(Fr)^{0.5}(\cos\theta_j)^{-0.003} \qquad \frac{D_2}{D_j} = 1.07(\frac{tV_j}{D_j})^{1.02}(Fr)^{-0.18} \tag{3.10}$$

Where Fr is the Froude number as shown in 3.11, D_1 is the diameter of the air sheath, D_2 is the penetrating depth of the air sheath, D_j is the jet diameter at the waterline and t is the time before the sheath collapses. The time before the sheath collapses is called the pinch of time, t_p, which corresponds to the maximum penetration of the water before the air sheath collapses, [Esmailizadeh and Mesler, 1986]. For a stationary jet with an angle of 45 degrees and a penetrating velocity of $2.5m/s$ the t_p is $54ms$.

$$Fr = \frac{V_n}{\sqrt{gD_n}} \tag{3.11}$$

These variables in combination with the jet diameter allow for the calculation of the size of the air sheath around the jet as a function of D_1, D_2 and D. When the water jet is entirely broken up due to the distance it had to travel to reach the water surface it can be compared to individual water droplets hitting the surface. When a small droplet hits the water surface the surface and penetrates the water line it entrains air into the water, the same as a cohesive water jet would have. The amount of air entrained compared to its size is larger for the droplet than the jet. As apposed to a plunging sheath the air the bubble entrains doesn't increase air entrainment length. Since the water droplet is much smaller and less heavy than the jet the momentum is also much lower, reducing the depth to which the droplet will penetrate. This leads to the assumption that when a water jet has fallen apart in a mist of droplets there is very little momentum left below the surface which in turn will lead to less erosion, [Esmailizadeh and Mesler, 1986].

3.6. Bubble formation

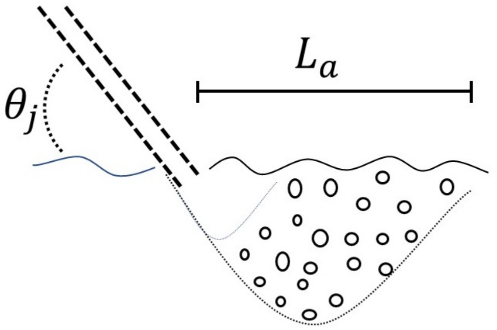

Figure 3.6: Schematic overview of re-circulation zone

Air is entrained into the water due to an air sheath being formed around the jet when the water jet penetrates the waterline. The amount of air entrained increases with the velocity of the plunging jet. When this air sheath collapses a lot of bubbles are formed around the jet. The bubbles are then dragged downwards along the jet due to the velocity of the jet. The downward velocity of the bubbles decreases with the distance covered until the vertical velocity component is zero. After this, the bubbles will slowly start moving to the surface due to their buoyancy. The rising bubbles can still have a forward horizontal velocity. Resulting in the bubbles concentrating in a bowl-like figure opposite the jet, called the re-circulation zone. In Figure 3.6 the re-circulation zone can be seen and a small area where there are no bubbles at the location where the jet hits the water. The re-circulation zone increases with an increase in jet velocity or a decrease in jet angle, as long as the jet is able to pierce the waterline. The theoretical depth of bubble penetration, H_p, is given in Formula 3.12. Where the values of the numbers used in the formula changed depending on the velocity and diameter of the jet at the nozzle. The values for the nozzle which will be applied are given in the formula, which is based on experiments done by [Biń, 1993].

$$H_p = 2.4V_n^{0.66}D_n^{0.66} \tag{3.12}$$

Applying this formula to the values provided in Chapter 2 the resulting depth to which the bubbles will penetrate is between $2.7m$ and $4.9m$. Both depths are large enough that the bubbles should easily reach the bottom. The formula used here is for vertical plunging jets instead of inclined plunging jets, but due to the depth reached being more than twice the depth present it is still very likely that bubbles will still be able to reach the sand at the bottom. If the bubbles were to reach the bottom of the pool they will influence the jet density at that location. Since the velocity depends on the density and the pressure more air decreases the density and reduces the flow velocity. Even though the bubbles should reach a large enough depth, they still might not reach the bottom. After the jet hits the bottom it will move to the left and right, creating the flow velocity which will carry off the sand particles. The bubbles might not be able to pierce this layer of moving water at the bottom and might immediately be carried away by the flow. If that is the case they won't influence the density at the location of the erosion.

According to [Smit, 2007] the aeration length, L_a, is determined by the water discharge at the nozzle, Q_w. The aeration length is the horizontal distance the bubbles will reach from the point where the jet hits the water, see Figure 3.6. When the water is very shallow the aeration length is larger than in very deep water where the bubbles won't reach the bottom.

$$L_a = 0.5Q_w^{0.5} \tag{3.13}$$

The influence of the bubbles on the development of the jet velocity after the waterline penetration might curve the jet slightly upwards. Since the jet in question is very turbulent there are a lot of bubbles due to the waterline penetration, [Roy and Kumar, 2018]. The bubbles entrained by the jet while in the air break up the jet when submerged. Decreasing the penetration depth of the jet itself. With a lot of bubbles, the jet lands on a cushion of rising air bubbles. Which will significantly decrease the penetration depth of the jet.

3.7. Water salinity

Whether salt or fresh water is used for the jetting has indirect consequences on certain previously mentioned parameters. Such as the difference between bubble coagulation. The small bubbles in freshwater can combine and form larger bubbles whereas small bubbles in salt water won't fuse and will stay small individual bubbles. Because of this, there is more spread in bubble size in fresh water, with an average of $3mm$. And a smaller spread in salt water with an average of no more than $0.5mm$. The bubbles in freshwater are larger and have more buoyancy than bubbles in salt water. Because of this bubbles in freshwater have less underwater residency time compared to salt water and might reach lesser depths than bubbles in salt water. This will influence the density of the jet at a depth where in freshwater the bubbles have already ascended and in salt water, they are still present. This makes it difficult to accurately represent saltwater bubble conditions in freshwater. To be able to represent this the used jet should have a diameter less than $0.5mm$ with a jet velocity low enough to stay in the 'chain regime', where the bubbles ascend in a chain-like configuration. The exact borders of this regime are hard to define since there are large transitions and it is not always easy to distinguish them. If the jet velocity increases further the size of the bubbles between fresh and saltwater will differ, [Lubking, 2000]. This is outside of the regime where the tests will be done, so there will be a difference between testing in fresh or salt water. The surface tension between salt and fresh water is also different. The surface tension of fresh water is $0.073mN/m$ and the surface tension of salt water is $0.076mN/m$, indicating that the velocity loss due to salinity is likely to be negligible. The water jetted in practice will be seawater, not fresh or salt water. Seawater also differs slightly in the mentioned aspects from salt water. Where air entrainment in seawater is even less than that in salt water. Since it not only depends on density, viscosity, surface tension, and salinity, but also on other physical, chemical, and biological properties, these differences are again negligible, [Chanson et al., 2006].

3.8. Underwater distance

The height of the water level above the sand determines the distance the jet still has to cover after penetrating the waterline. The velocity of the jet after piercing the water surface can be calculated by using Formula 3.14 with V_m the speed below the waterline and x the distance below the surface. When plotting Formula 3.14 it shows that the jet loses most of its energy in the first half a meter after the air film, this is likely due to momentum conservation. Where the increase in mass due to water entrainment causes the center line velocity of the jet to decrease. Since the density of water is much higher than the density of air the velocity lost due to entrainment at the edges of the jet is much larger when the jet hits the water. The formula mentioned here is for a straight plunging jet and is independent of potential influence of bubbles, [Lewis et al., 1999].

$$V_m = 3.3 * V_j(\frac{D_j}{y})^{1.1} \tag{3.14}$$

When taking into account the incline and the potential curving of the jet after penetrating the waterline due to the bubbles working as a cushion on the jet the velocity decrease of the jet might be even larger. The smaller vertical component due to the incline under which the jet hits the waterline reduces the vertical velocity, as well as the increased surfaces through which the jet has to penetrate and the bubbles acting like a cushion on which the jet lands. This would decrease the vertical velocity of the penetrating jet even further.

$$\frac{u_{s,0}}{u_0} = 6.2\frac{D_n}{s} \tag{3.15}$$

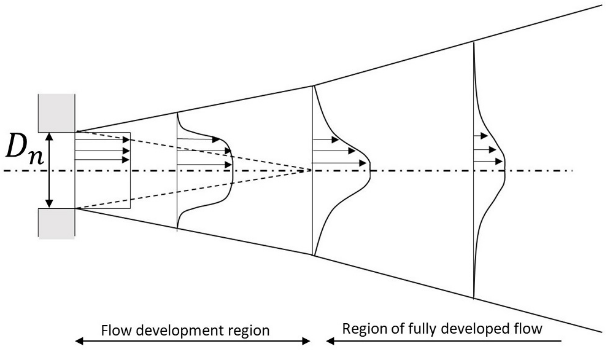

Figure 3.7: Flow field in a free circular jet, [Nobel, 2013]

A submerged jet, as opposed to a plunging jet, would immediately have contact with stagnant water and wouldn't have an air cavity around it. The velocity of a submerged jet is given by Formula 3.15.

This equation is only valid for $s > 6.2D_n$. Where $u_{s,0}$ is the velocity at distance s, u_0 is the exit velocity and D_n is the nozzle diameter. The large velocity difference between the jet exiting the nozzle and the surrounding water would cause a shear zone to immediately develop. The increase in mass moved will decrease the velocity according to constant momentum. The center line velocity stays the same until the flow is fully developed, as visible in Figure 3.7. The development region is the first part of the jet where there is still a core in the center of the jet with a velocity equal to the nozzle exit velocity, after the flow is fully developed and the flow field keeps increasing in size with velocities below the exit velocity. Where the velocity of the jet in air was determined using the projectile motion, the velocity of the jet in water was determined with momentum conservation. Another main difference between a submerged jet and an plunging jet being the initial air entrainment as an air sheath and after that the air sheath collapsing into a cloud of bubbles and the entrained air bubbles acting like a cushion, [Nobel, 2013].

3.9. Pick-up flux

From the multiple different pickup functions only the high-velocity pickup functions are focused on here. These are the revised [van Rijn et al., 2019] dimensionless pickup rate, the [Winterwerp et al., 1992] pick-up rate and the [Cheng et al., 2020] pick-up rate, these are shown in Formula 3.17 respectively. These were selected out of all the available pick-up functions since these were determined to be in the same regime as the production of the experimental jet since they were high-velocity pick-up functions. According to [Heijmeijer et al., 2022] the van Rijn and Winterwerp pick-up functions underestimate the actual erosion, as visible in Figure 3.8.

The erosion can be expressed as $kg/\frac{m^2}{s}$ or the erosion can be determined in m/s by using the formulas in Formula 3.16.

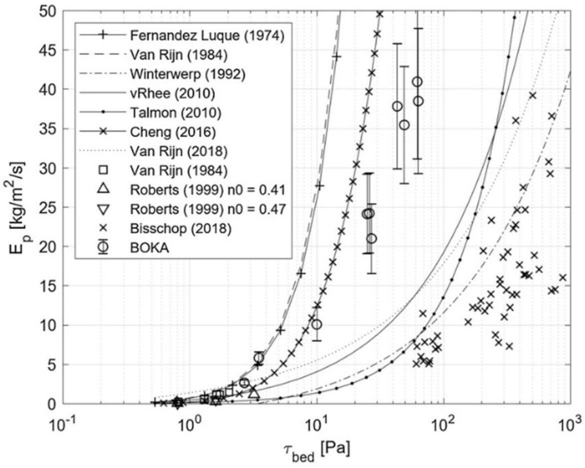

Figure 3.8: Comparison of the different pickup functions, [Heijmeijer et al., 2022]

$$v_e = \frac{E - S}{\rho_s(1 - n_0 - C_{nb})} \qquad E = \phi_p \rho_s \sqrt{g\Delta D} \tag{3.16}$$

Here E is the erosion, S is the settling flux, n_0 is the in situ porosity of the bed and c_{nb} is the near bed volumetric concentration, which is taken as zero. Using the known starting diameter of the jet, the time duration, and the erosion velocity the maximum diameter can be calculated. This can in turn be used to determine the diameter of the theoretical hole formed in the sand. The volume of this theoretical hole gives the total production of the jet.

The pick-up functions are given in Formula 3.17, where θ is the shields parameter, θ_{cr} is the critical shields parameter, [Brownlie, 1981], D_* is a dimensionless particle parameter and F_* is the densiometric Froude number.

$$\phi_p = 0.00033 D_*^{0,3} \frac{1}{\theta} (\frac{\theta - \theta_{cr}}{\theta_{cr}})^{1.5} \qquad \phi_p = 0.012 D_*^{0.3} (\theta^{0.5} - 1.3) \qquad \phi_p = 0.0001 D_*^{2.5} (F_* exp(-\frac{40}{F_*})) \tag{3.17}$$

The equations needed for Formula 3.17 are given in Formual 3.18

$$\theta_{cr} = 0.22 R_p^{0.6} + 0.06 \exp(-17.77 R_p^{-0.6}) \qquad \theta = \frac{\tau}{g(\rho_s - \rho_w) D} \qquad D_* = \sqrt[3]{\frac{\Delta g}{v^2}} D \qquad F_* = \frac{u}{\sqrt{\Delta f D_{50}}} \tag{3.18}$$

Where R_p is the particle Reynolds number,Δ is the specific density and τ is the shear stress, as shown in Formula 3.19

$$R_p = \frac{D\sqrt{\Delta g D}}{v} \qquad \Delta = \frac{\rho_s - \rho_w}{\rho_w} \qquad \tau = \frac{f}{8}\rho_m u^2 \tag{3.19}$$

Where D is the particle diameter, g is the gravitational acceleration and v is the kinematic viscosity of water. Where f is the friction factor derived from the Moody chart using the Reynolds number and the relative pipe roughness, which is taken as five times the D_{50}.

3.10. Sand erosion

All of the elements discussed previously will influence the flow velocity and pressure of the jet when it eventually reaches the submerged sand. Where the determined parameters can be related to the erosion speed of the jet. This is possible without actually having to jet in sand.

The erosion speed of the sand depends on properties of the sand itself and properties of the water jet coming into contact with the sand. The permeability of the sand, k, depends on the particle size distribution, D_{15}, the porosity, n_0, and on the kinematic viscosity, v, of the fluid as shown in Formula 3.20 by [den Adel, 1987]. The permeability is influenced by the D_{15} of the sands particle size distribution. The D_{15} the size for which 15 percent of the sand particles have a smaller diameter than the given value.

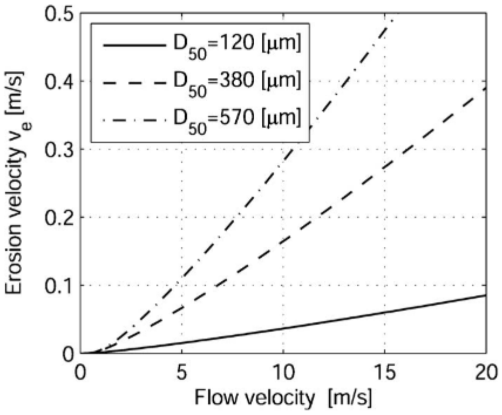

Figure 3.9: Erosion velocity as a function of the flow velocity, [Van Rhee, 2010]

$$k = \frac{g}{16v} D_{15}^2 \frac{n_0^3}{(1-n_0)^2} \tag{3.20}$$

If the stagnation pressure of the jet is measured it can be related to the flow velocity using Formula 3.21. This value, in combination with the median particle size of the sand, D_{50}, can be used to determine the erosion velocity using Figure 3.9 from [Van Rhee, 2010]. To determine the flow velocity from the stagnation pressure the density is needed. The friction factor, f, is used to be able to determine the shear stress. The friction factor depends on the Reynolds number and relative roughness and can be determined by using a Moody diagram.

$$u = \sqrt{\frac{2p}{\rho_w}} \qquad \tau_b = \frac{f}{8}u^2 \rho_w \tag{3.21}$$

Since the incoming jet is a turbulent plunging jet that entrains air while penetrating the waterline the density is a combination of the density of water and air, depending on the ratio between air and water. If the location of the sand is deeper than the penetration depth of the bubbles the density can be considered constant and equal to the water density. As shown in section 3.6 the depth of plunging bubbles is given using Formula 3.12 and can be applied to the actual to find the penetration depth of the bubbles. Applying this formula it follows that air bubbles can reach the depth where the erosion takes place. The density at the erosion location might still be pure water if the bubbles aren't able to penetrate the water flow of the jet coming off the bottom and flowing to the sides.

3.11. Erosion according to Vlasblom

Another way erosion is often determined is by using the Vlasblom formula for the production of a jet, as shown in Formula 3.22.

$$M_s = \alpha I = \alpha \rho_w Q_j u_0 = \alpha \rho_w Q_j \sqrt{\frac{2p_j}{\rho_w p_j}} \tag{3.22}$$

Where M_s is the mass flux of the eroded sand, α is a dimensionless empirical parameter which according to Vlasblom is $0.1 s/m$ [Vlasblom, 2003] for average sand, as is the sand assumed for the sand in the experiment. The I is the jet momentum, which consists of; Q_j, the jet discharge, p_j, the jet pressure, and ρ_w, the water density. The formula from Vlasblom depends on a constant times the momentum. Jetting formulas often assume that the momentum is conserved. Meaning that when the area over which the jet propagates increases its velocity decreases and vice versa. Since the momentum is conserved the value for the mass flux does not change at different distances from the jet nozzle. This results in a constant value for the mass flux over the entire distance. Giving a value for the erosion according to Vlasblom which is the same over the entire trajectory of the jet. This value can be assumed as the maximum erosion achievable by the jet.

3.12. Supercritical flow

The erosion process of the sand bank would be less complicated if there was no water puddle on top of it. Creating supercritical flow could be a possibility to jet away the water after which the jet is directly jetting in the sand, as opposed to plunging as shown in Figure 2.2. Due to this, there is only air entrainment and no water entrainment with constant momentum which means that the center line velocity decreases less rapidly. Removing this water might lead to a higher erosion velocity when the jet hits the sand. If a hydraulic jump were to take place the water would reflect off the bottom and drain the water over the sandbank as shown in Figure 3.10. The flow speed at the bottom can be calculated when the initial diameter and velocity of the jet and the distance x are known. Where x is the distance underwater from the waterline where the jet is moving straight, without curving.

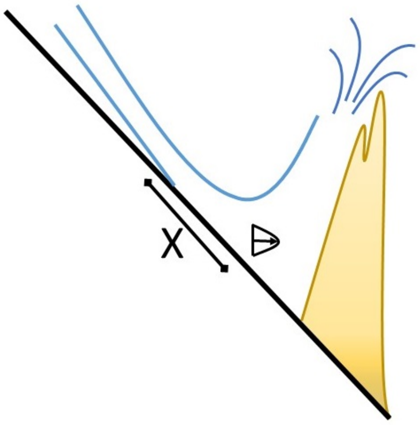

Figure 3.10: Schematic flow rate of supercritical flow

$$V_b = 3.5 \sqrt{\frac{D_n}{2y}} V_j \tag{3.23}$$

Using Formula 3.23 the velocity of the jet at the bottom of the pool, V_b, can be calculated, [Brandt et al., 2016]. The supercritical flow forming here might create a hydraulic jump, where the water surface rises abruptly when a high-velocity jet enters a low-velocity or stagnant pool.

For a situation where the proposed hydraulic jump happens in a pool with walls on either side the formula is given in 3.24, [Bhagat et al., 2020]. Which is based on the continuity of momentum at the jump, the balance between the loss of momentum of the incoming jet and the thrust of the water at the jump. Due to the conservation of momentum, the high-velocity incoming jet increases the velocity of the still pool and increases the speed enough to make it more water than went in jump out. That way reducing the depth of the pool.

$$\rho_w u^2 h - \rho U^2 H = \frac{1}{2}\rho g(H^2 - h^2) \tag{3.24}$$

Where h is the height of the film at radius r, U is the velocity at the nozzle and u is the velocity at the bottom. Being able to apply this formula requires knowledge of the flow field on either side of the location where the jet hits the water and the height of the jump over the wall has to be determined experimentally as well. This means that these values have to be measured in situ before this formula can be applied.

3.13. Scaling

If the tests were to be done full scale the measured values could directly be related to the processes happening in the prototype. This would make the results easily relatable to the actual scenario but doing the tests at this scale would cost too much time and money, hence a scaled-down version will be used. Scaling is done using scaling factors, which is the ratio between the value of the prototype and the model, as shown in Formula 3.25.

$$n_x = \frac{n_s}{n_a} \tag{3.25}$$

Where n_x is the factor with which a dimension is scaled, n_s is this dimension in the set-up, and n_a is this dimension in the actual scenario.

3.13.1. Scaling water

Scaling experiments in which water plays a prominent role can be done in multiple ways. Scaled laboratory studies are often subject to dimensionless scaling factors; free surface flows are often scaled with the Froude number, surface tension-dominated experiments are often scaled with the Weber number, and flow velocity-dependent experiments are scaled with the Reynolds number, [Chanson et al., 2006]. These three dimensionless scaling factors are shown in Formula 3.26. The actual jet has a very large Reynolds number, meaning that it is deep in the turbulent flow region. At such a large value the jet is very turbulent and some variation in the Reynolds number doesn't impact the characteristics of the flow noticeably. That is why scaling with Reynolds won't be dominant in this experiment, so the experiment will be scaled with either Froude or Weber.

$$Fr = \frac{V_n}{\sqrt{gD_n}} \qquad We = \frac{\rho_m V_n^2 D_n}{\sigma} \qquad Re = \frac{\rho_m V_n D_n}{\mu} \tag{3.26}$$

The Froude number is a dimensionless number which relates the ratio of flow inertia to the gravity or is used to change the length scaling. As shown in formula 3.26 the Froude number is a relation of speed over length. Froude is often used for high turbulent phenomena where friction effects are negligible. The Weber number is a dimensionless number, shown in formula 3.26, which relates the inertia to the surface tension. Weber is often applied when surface tension, σ, or air entrainment are determining factors.

$$Fr : n_u = \sqrt{n_L} \qquad We : n_u = \frac{1}{\sqrt{n_L}} \tag{3.27}$$

In 3.27 the scaling factor for velocity, n_u, as a function of the scaling factor for the length, n_L, according to Froude and Weber are shown. Since $n_g = 1$ and $n_{Fr} = 1$ the resulting ratio is given in Formula 3.27 for Froude and Weber. For scaling down the experiment according to Froude the velocity has to be divided by $\sqrt{n_L}$ and for Weber divided $\frac{1}{\sqrt{n_L}}$.

$$p = \frac{1}{2}\rho u^2 \tag{3.28}$$

When choosing a scaling factor for the length this not only influences the velocity scaling but the scaling of the pressure as well, since this is dependent on the velocity. In formula 3.28 the formula for the pressure is given. Assuming $n_\rho = 1$ gives n_p as shown in formula 3.29 for Froude and Weber.

$$Fr : n_p = n_u^2 = n_L \qquad We : n_p = n_u^2 = \frac{1}{n_L} \tag{3.29}$$

The same issue arises with the scaling of the pressure as with the velocity where the dimensionless scaling number scale in opposite direction of each other. Having to divide by the length scales given in formula 3.29 results in the scaling factors shown in Table 3.2.

	Froude	Weber
Length $[m]$	n_L	n_L
Pressure $[bar]$	n_L	$\frac{1}{n_L}$
Velocity $[m/s]$	$\sqrt{n_L}$	$\frac{1}{\sqrt{n_L}}$

Table 3.2: Scaling of Froude and Weber side by side

It is unclear which of the two dimensionless scaling factors, Froude and Weber, is more important for the scaling of this experiment. The assumed significant impact of the Weber number is for the part of the jet in air. And the Froude number is governing for the jet after the waterline penetration. The location where the jet pierces the waterline is likely influenced by both numbers.

Some scaled options with the corresponding pressures, lengths and velocities are shown in Table 3.3. Scaling with Froude results in increasingly high pressures for scaled down tests. This in combination with the results below water being more of interests for the subject of this report makes the scaling factor used in this set-up the Froude number.

	Actual	Froude		Weber	
Scale	1:1	1:2	1:5	1:2	1:5
Length [m]	8	4	1,6	4	1,6
Pressure [bar]	4 - 8	2 - 4	0,8 - 1,6	8 - 16	20 - 40
Velocity [m/s]	27 - 40	19,7 - 28	12,5 - 17,7	39,5 - 55,9	62,5 - 88,3

Table 3.3: Scaled parameters for Fr en We

The length will be scaled down by half as will the pressure, which corresponds to scaling according to Froude. This is partially because scaling according to both is impossible and scaling according to Weber has the pressure of the jet increase to pressures that are difficult to attain in the laboratory setting.

3.13.2. Scaling sand

If sand was to be incorporated in the experiment it would also need to adhere to these scaling rules. The sand particle diameter can, in theory, be adjusted by using larger or smaller diameter sand particles. The sand in the actual scenario is very fine sand but could be replaced by other sand to adhere to the scaling rules. When sand with a smaller or larger diameter were used the material would behave differently since the particle size influences the erosion process. Besides a difference in consolidation and porosity of the material of the larger or smaller particles, the erosion process of either size doesn't scale well as can be derived from Formula 3.19 and 3.16.

Scaling of erosion velocity is also an important parameter. Where the erosion velocity, v_e depends on the pick-up flux, E, the settling flux, S, the density of the grains, ρ_s, the porosity of the settled original bed, n_0 and the near-bed concentration, c_b. As shown in Formula 3.16. Using the definition of the settling flux and the definition of the erosion velocity and substituting these in Formula 3.16 using the van Rijn pickup function gives Formula 3.30.

$$v_e = \frac{1}{\rho_s(1-n_0-c_b)}(\phi_p\sqrt{g\Delta D} - c_b w_s) \tag{3.30}$$

The formulas for erosion velocity were discussed more in-depth in Chapter 3.9. Where it can be noted that the erosion velocity depends on velocity through the shear stress, as shown in Formula 3.18. The scaling from the erosion Formula 3.30 is given in Formula 3.31,

$$n_{ve} = \frac{\sqrt{n_L}}{(1-n_n-n_{cb})} n_L^{0.3} \frac{1}{n_\theta} (\frac{n_\theta - n_{\theta cr}}{n_{\theta cr}})^{1.5} \tag{3.31}$$

Where the pick up flux of van Rijn from Formula 3.17 is used. Assuming the same sand characteristics in the model and in the prototype gives that n_ρ = n_n = n_{cb} = 1

To determine the resulting scaling factor from Formula 3.31 the scaling for the Shields and critical Shields parameter are needed, these are given in Formula 3.32.

$$n_{\theta cr} = (n_{Rp}^{0.5})0.6 + exp((n_{Rp}^{(0.5)}){-0.6}) = n_{Rp}^{0.3} + exp(n_{Rp}^{-0.3}) \qquad n_\theta = \frac{n_v^2}{n_L} = 1 \tag{3.32}$$

The scaling factor of the particle Reynolds number needed to determine the critical Shields parameter is given in Formula 3.33.

$$n_{Rp} = \frac{n_L^{1.5}}{n_u} = n_L^{0.5} \qquad n_{\theta cr} = n_L^{(0.5)^{0.6}} + exp(n_L^{(0.5)^{(-0.6)}}) = n_L^{0.3} + exp(n_L^{-0.3}) \tag{3.33}$$

Adding all these scaling Formulas in the erosion scaling formula results in the scaling factor given in Formula 3.34.

$$n_{ve} = \frac{\sqrt{n_L}}{(1-n_n)} n_L^{0.3} \frac{1}{n_\theta} (\frac{n_\theta - n_{\theta cr}}{n_{\theta cr}})^{1.5} = n_L^{0.8} \tag{3.34}$$

For the total production the erosion velocity, v_e, has to be multiplied with the surface which is eroded, A, where n_A is equal to n_L^2, which is shown in Formula 3.35

$$n_P = n_{ve} n_A = n_L^{0.8} n_L^2 = n_L^{2.8} \tag{3.35}$$

The resulting scaling factor for the erosion velocity gives $n_L^{2.8}$ instead of the desired scaling factor of $\sqrt{n_L}$. This means that the erosion of the model does not accurately represent the erosion of the prototype, but overestimates the actual erosion.

3.13.3. Scaling Vlasblom's erosion rate formula

As shown in Formula 3.36 the erosion according to Vlasblom depends on density, jet pressure, surface area, and velocity.

$$M_s = \alpha \rho_w (A V_n) \sqrt{\frac{2 p_j}{\rho_w}} \tag{3.36}$$

The result when scaling this formula according to Froude is given in Formula 3.37.

$$n_{M_s} = (n_A n_V) \sqrt{\frac{n_{p_j}}{n_\rho}} \qquad n_{M_s} = (n_L^2 \sqrt{n_L}) \sqrt{\frac{n_L}{1}} = n_L^3 \tag{3.37}$$

The scaling according to sand size and Vlasblom differ and as such the scaling of the production is not accurate when scaled back up to full size.

3.14. Literature evaluation

A lot of literature found and referenced in this report has the jet coming in at a vertical drop, which influences the characteristics of the jet and the plunging. For example the bubble formation is different, as is the speed of the jet at the waterline and the formula for velocity development of the jet after hitting the waterline is different as well. The velocity of the proposed jet is also much higher than those in most of the found literature. Whereas most studies used velocities between 4 to 10 m/s with an outlier at 90 to 150 m/s the velocity of the eventual jet will be between 30 to 50 m/s. Causing the jets to differ in either Reynolds, Froude or Weber. This makes it difficult to relate the found values to the dimensions and variables of the actual experiment. Trying to apply the found formulas to this jet might present a model which doesn't match with reality.

To know the flow velocity, shear stress and erosion velocity in the hopper, the stagnation pressure needs to be determined. To find the optimal parameters for quick erosion the stagnation pressure should be measured with varying parameters at the nozzle, from which the ideal jet settings can be found. The distance covered in water and air can be changed for different jet set-ups. The coherence of the jet over its trajectory is not clear. It seems that it is a very important factor for momentum conservation but is difficult to determine before hand. So in all the potential set-ups the break up length should also be determined. The momentum and velocity losses in air depend a lot on the distance the jet has to travel and seem mostly impacted by the traveling length being larger than the break-up length. The losses of the jet don't really seem to occur due to the penetration of the waterline but due to the water entrainment which happens afterwards. The waterline penetration can be optimized by having a large air sheath during penetration and that way delay the water entrainment into the jet.

4

Experimental set-up

Before the actual set-up was designed some small tests were done to get a feeling for the influential factors. These small scale tests are described in Appendix A.

Two different types of tests were done, one to determine the velocity at the location of interest, using four different pipe configurations before nozzle, see Figure 4.4, and one to determine the production of the jet, with one configuration before the nozzle. Where for the velocity test the jet was pointed at the frame where the pressure and density were measured. And for the sand test instead of the frame a large container filled with sand was used.

4.1. Overview experimental set-up

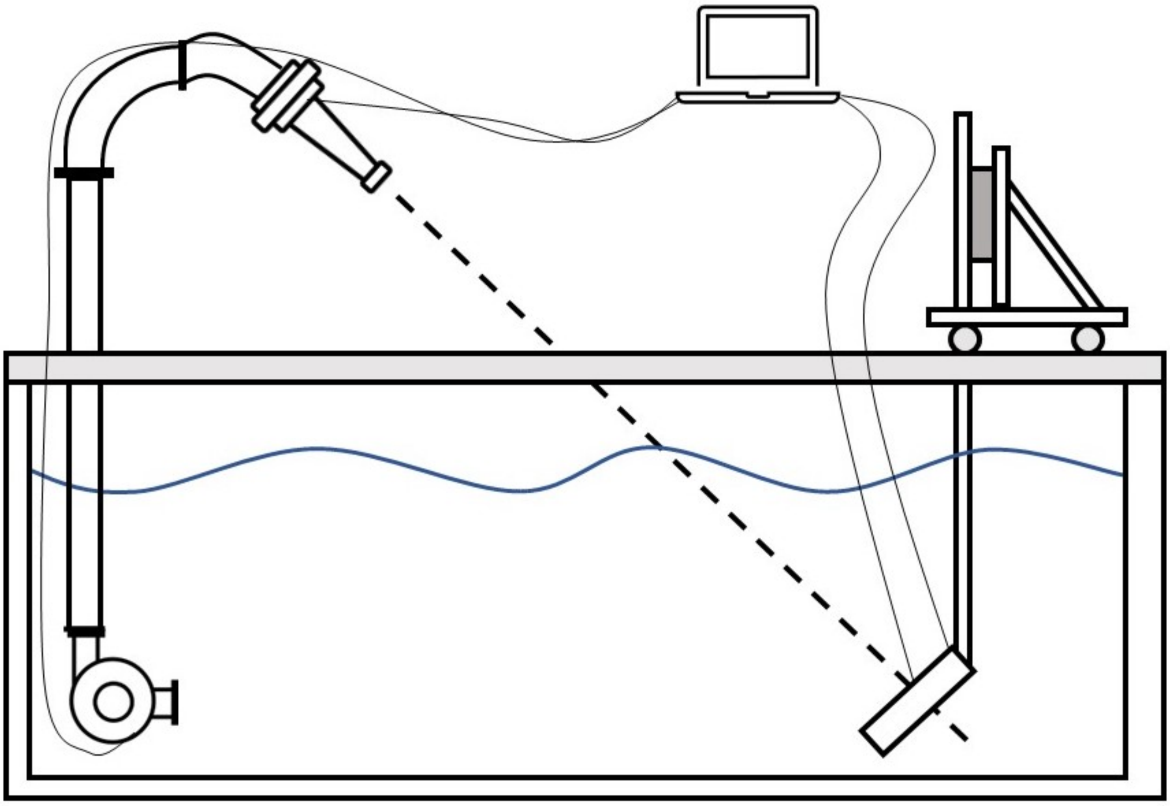

Figure 4.1: Schematic overview of the entire set-up

Figure 4.2: Middle bend configuration in the laboratory

The test were done at the Boskalis laboratory with the associated pump. The water tank has a perspex window on the side of the tank to view below the water line. The pump can reach a pressure of 3.7 bar for 953 rpm. Where the lines of the pump pipeline curve intersect at 3.5, 2.9, 2.3 en 1.35 bar. These correspond to 4, 6, 8 en 10 cm jet nozzles. The size of the tank also allows for significant set-ups where the movement of the measuring devices is possible by hand. The pump gave a volumetric flow rate of 41,4 cubic meters per hour, which resulted in a jet pressure of 3,6 bar at the nozzle. This equals an exit velocity of 26,8 meters per second.

Figure 4.1 gives a schematic impression of what the configuration looked like. The segment from the top of the pump to the jet nozzle was changed depending on which of the four pipe configurations was tested, the rest of the composition stayed roughly the same. The pump inlet was close to the bottom of the pool, as was the pump, with the heart of the pump being around 80 cm above the bottom of the pool, resulting in a minimum water height. The water was transported from the pump vertically to configuration that led towards the nozzle. The two wires from the pump and the nozzle to the laptop transmitted the volumetric flow rate of the pump and the pressure at the nozzle respectively. The measuring frame was attached to a different frame that was attached to a movable cart, that way the measuring frame could be placed in the center of the jet exiting the nozzle. The jet was pointed to the center of the measurement frame where measuring devices were located to determine the density and the pressure. The two wires from the measuring frame conveyed these measured values to the laptop. The water level could be changed by adding or removing water from the tank.

Figure 4.2 shows the actual jetting part of the experiment in the lab. The measurements of which are more accurately specified in Chapter 4.3. This set-up could be changed to test different possible scenarios.

Using actual sand in the experiment to determine the erosion speed of the jet makes the entire set-up messier and too time-consuming to do enough iterations of it. Some tests with sand were done to determine the production of the jet set-up, but only from one pipe configuration since setting up, and executing the experiments with sand was very time-consuming. These tests were done at the end of the testing period and are not entirely accurate when scaling back up to the actual jet size, due to the sand particle size not being scaled according to Froude as discussed in Chapter 3.13.

4.2. Nozzle dimensions

A picture of the nozzle is shown side by side with a schematic overview of the nozzle in Figure 4.3

The nozzle starts at a diameter of $80mm$ and tapers to an inner diameter of 25mm over a total distance of $90mm$ as is clear from Table 4.1.

By using the measured and the theoretical volumetric flow rate the nozzle discharge coefficient, C_D can be calculated, where C_D is equal to 0.78.

Part	Length [mm]	Inner diameter [mm]
1	10	80
2	70	80 - 25
3	10	25

Table 4.1: Length and diameter of parts nozzle

The nozzle was consistent for nearly all the test. Only the flap test used a different nozzle with a flap attached to the nozzle as shown in Figure 4.5.

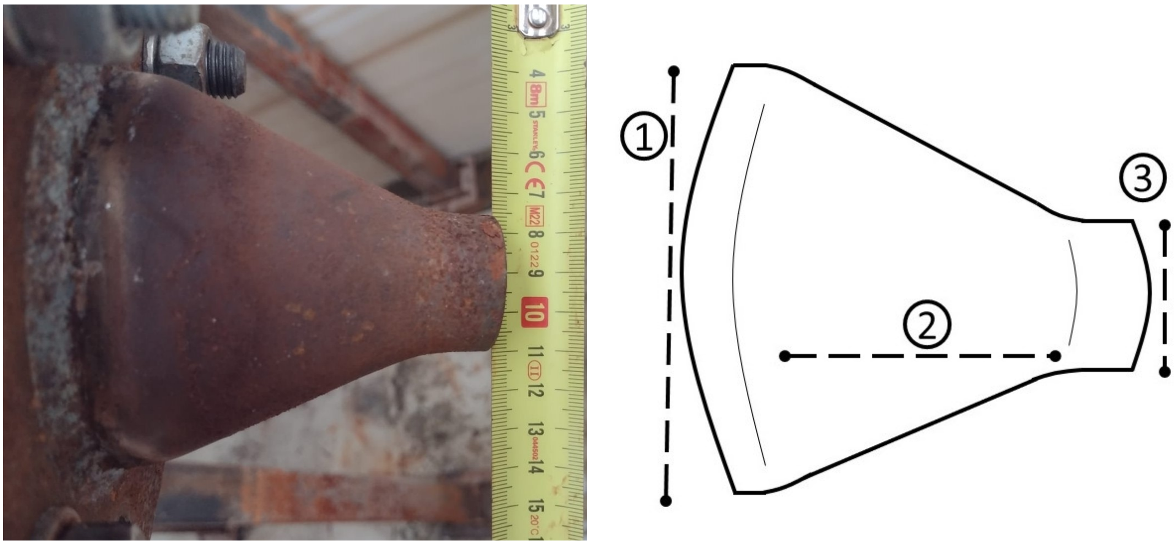

(a) Nozzle (b) Nozzle schematic

Figure 4.3: The nozzle next to a schematic drawing

4.3. Four pipe configurations

The experiment consists of the parts shown in appendix B and the parts shown in Figure 4.2. These were constructed at the Boskalis wharf at Capelle aan de IJssel. After construction, these parts were moved to the lab in Papendrecht where the actual experiments would take place. These parts consisted of a frame for the measuring devices, a foundation for the jet nozzle, and a base to which the measurement frame could be attached and used to move the frame into the right location. By changing the order of the multiple pipes the flow of the water could be influenced to change the inflow of the water into the nozzle. These pipe segments are shown schematically in Figure 4.4, their lengths or heart to heart distances are given in Table 4.2. Where the r/D from the two S-bends and segment *b* are 2.5.

Here *a* is a 3-meter-long hose that connects the pump to the nozzle part of the pipe configuration. The length of heart-to-heart distance and the inner diameter of all the pipes are given in Table 4.2. Where part *b* is a bend to make the connection of the hose more manageable over the inclined table to which the pipes are fastened and part *d* is two bends attached in an S-shape, an S-bend, to add a spiral flow to the water.

Part	Length or hth [m]	Inner diameter [mm]
a	3	100
b	0.35	80
c	0.54	80
d	0.2	80
e	1	70

Table 4.2: Length and diameter of pipe segments

Using these different segments four different pipe configurations were created to simulate different parts of the water trajectory in the vessel.

4.3.1. Straight jet pipe configuration

Most tests were done with a straight jet configuration, as shown in Figure 4.4a. This consisted of the hose from the pump to the first bend and from there on only straight pieces of pipe. This set-up consisted of the pieces *a,b,c* and *e* when consulting Figure 4.4. This pipe configuration would most likely be the best of the considered configurations since the flow experienced no negative influences when compared with the other three pipe configurations.

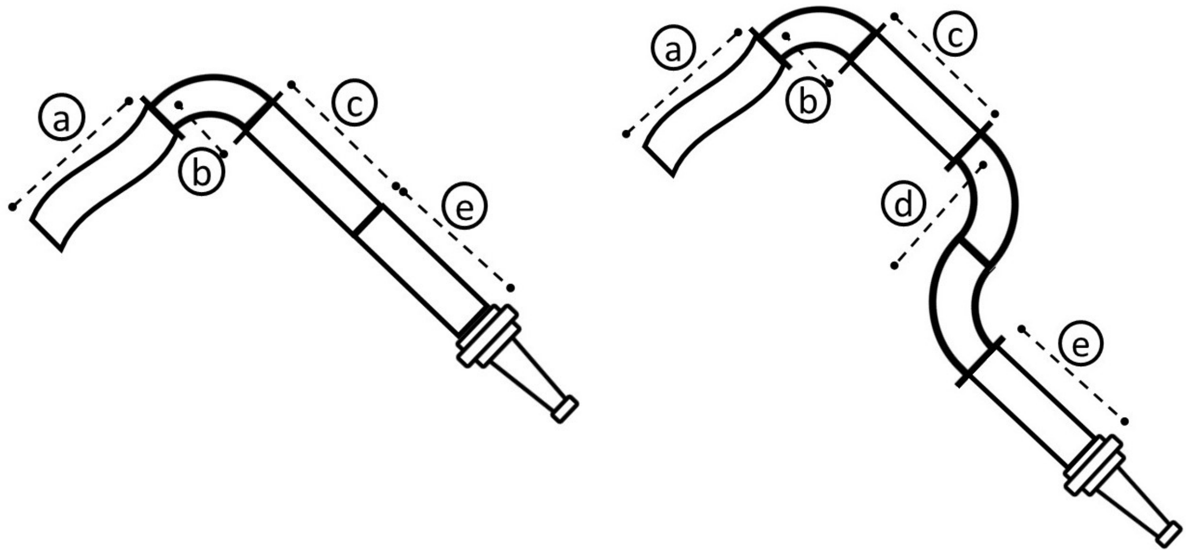

(a) Straight (b) Middle bend

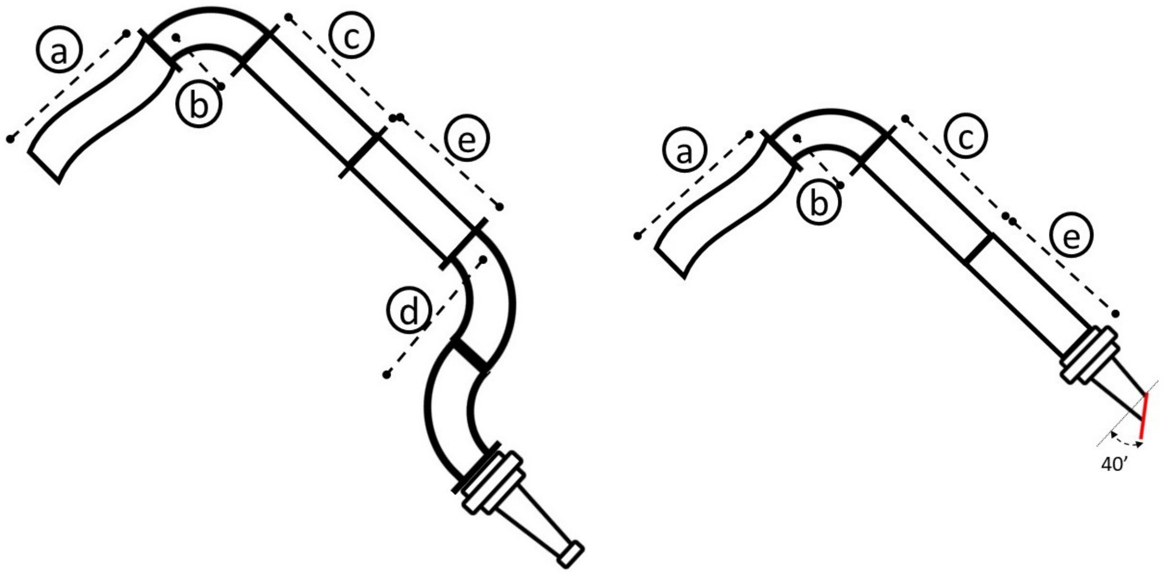

(c) End bend (d) Flap

Figure 4.4: The four different pipe configurations used for the experiments

4.3.2. End-bend pipe configuration

Since the jet has to turn a bend in the actual hull of the vessel its influence needed to be studied. This is why part *d* from Figure 4.4 was placed before the nozzle, as shown in Figure 4.4c. Mimicking the bend in the pipe layout of the vessel had a significant influence on the cohesion of the jet at the nozzle exit.

4.3.3. Middle-bend pipe configuration

To somewhat reduce this influence the bend was moved somewhat backward between parts *c* and *e*, as is the set-up in Figure 4.4b. This is slightly more accurate to the actual situation in the vessel and showed how a possible reduction in secondary rotating flow would influence the water jet. This is also the pipe configuration visible in Figure 4.2.

4.3.4. Flap pipe configuration

Since the nozzle in the vessel is closed off with a rubber flap to prevent sand from entering pipes this was mimicked as well, as shown in Figure 4.4d. This was done by cutting off the tip from the nozzle under a 40-degree angle and attaching a rubber flap of roughly the same material over this angled nozzle, as shown schematically in Figure 4.5. The water inflow of this pipe configuration was the straight inflow the same as in the straight pipe configuration, Chapter 4.3.1. Adding a bend into this pipe configuration would have brought different variables whose effects would be hard to distinguish from each other.

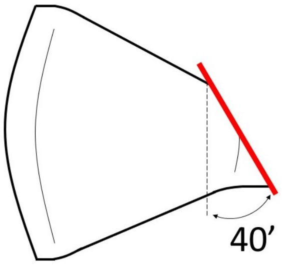

Figure 4.5: Schematic flap nozzle

4.4. Description of the used measuring devices

The entire experimental composition consists of multiple parts coming together to be able to measure the desired values. The devices used in combination with the before mentioned pipes will be discussed more in detail in this segment.

4.4.1. Pitot tube

To produce the velocity of the jet over its trajectory the velocity of the jet has to be determined at multiple different locations. The velocity of the jet will be determined using a pitot tube and Formula 4.1. Which is a rewritten version of Formula 3.21. This pitot tube is connected to a differential pressure sensor using an impulse tube. Multiple pressure sensors are connected to the pitot tube, a relative pressure sensor with a range from 0 to 5 bar and an absolute pressure sensor, also with a range between 0 to 5 bar. These pressure sensors are used to determine the pressure at the location of interest where the water jet connects with these measuring devices. The pitot tube at the impact location of the jet measures the total pressure at location 1 in Figure 4.6 and the static pressure at location 2. The total pressure is the sum of the static and dynamic pressure. Meaning that the dynamic pressure can be determined by subtracting the static pressure from the total pressure. Which in turn can be used to calculate the velocity as shown in formula 4.1.

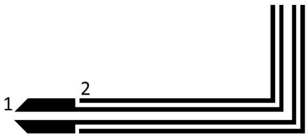

Figure 4.6: Schematic drawing of a pitot tube

$$u = \sqrt{\frac{2(p_1 - p_2)}{\rho}} \tag{4.1}$$

Where u is the velocity, $dp = (p_1 - p_2)$ is the pressure difference and ρ is the density of the air-water mixture.

The pressure sensors were connected to the pitot tube as shown in Figure 4.7. Where the stagnation pressure is measured by the absolute and the relative pressure sensor. The relative pressure sensor also measures the static pressure to determine the dynamic pressure.

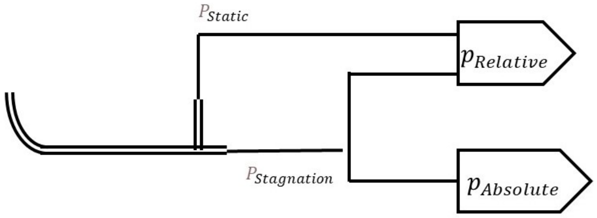

Figure 4.7: Schematic drawing of the connection of the pressure sensors to the pitot tube

At the nozzle a pressure sensor was also connected. This was to determine the pressure at the nozzle, there was a impulse tube connecting this nozzle directly to the pressure sensor. Since the density in the nozzle can be assumed to be only water the velocity here can be calculated by using the pressure from this pressure sensor without having to measure the density.

The electrical pressure transducer turns the measured pressure in a signal between 4 to 20 mA. Which by way of the converter is turned into a digital signal. This digital signal is logged by Dredge Datalogger, a Boskalis-made program. The value this logger puts out is interpreted as the pressure measured by the pitot tube.

4.4.2. Rods with conductivity sensors

The density is determined by connecting two rods with conductivity sensors in an X-shape close to the pitot tube, as shown in Figure 4.9. The conductivity concentration measurements are used in this scenario to measure the density of the air-water mixture in which they are submerged. These two rods have closely placed electrodes through which a current can run. The material in between these points influences the amount of current running from one side to the other. Whereas air is not a great conductive material, water is a very conductive material. Using an amplifier and a NI-DAQ (National Instruments -Data acquisition) these rods are connected to the PC, as shown in Figure 4.8. Where using a simple LabView set-up the conductivity between the points is given, as shown in Appendix C.

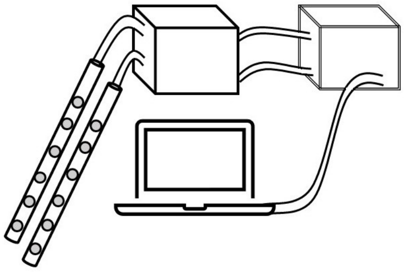

Figure 4.8: Rods with conductivity sensors to amplifier to NiDaq to PC

The rods with conductivity sensors give a maximum range between roughly -3 and 10 volts. The -3 measurement corresponds to pure air and the 10 Volt measurement corresponds to pure water. The maximum measurement of these conductivity sensors was around $10,7$ volt, which is why the range was chosen as large as possible without having the sensors clipping at this largest value. If the sensors were to clip at this largest value it would render the data unusable. An example from a test which was used to verify the largest and smallest voltage value from that day is given in Appendix D. Most measurement profiles in air corresponded with a line around the -3 value with peaks shooting upwards in the direction of the 10 Volts, but rarely reaching it. The reverse was the case for measurements for the measurement profile in the water, where there were spikes downward from the 10 volt line in the direction of -3 volt. The conductivity sensors measured the voltage value with a sample rate of 50Hz. This resulted in a large batch of data which corresponds to a water and air percentage, part of the raw data is shown in Appendix E. The interpretation of the rods with conductivity sensors is expanded upon in Chapter 6.

4.4.3. Measurement frame

The rods with conductivity sensors were connected to the frame in the shape of a cross, as shown in Figure 4.9. In this image, the measurement numbers of all the conductivity points are shown. These correspond to the output number in the NiDaq. Most often the measurements of points 1,9 and 10 were used. Since these were closest to the pitot tube. Point 2 is also very close to the pitot tube entrance but is somewhat sheltered by the pitot tube and the other conductivity rod, giving values that were often considered inaccurate. The average values of 1,9 and 10 were used to determine the water percentage at the pitot tube.

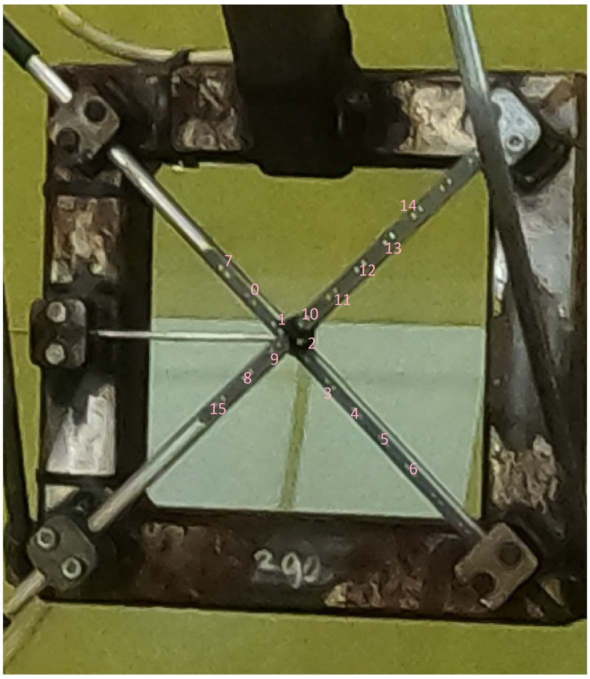

Figure 4.9: Conductivity points numbered in the frame

4.4.4. Volumetric flow rate meter

Besides the pressure sensors, the volumetric flow rate in the pipes was also measured by an Electro Magnetic Flow meter (EMF). Situated at the dredge pump, to measure the discharge. These measurements were given together with the nozzle pressure, the exact time, the relative pressure, and the absolute pressure, giving the same time values for all these measurements. The data points were logged with a sample rate of 1 Hz by the EMF.

4.4.5. Loadcell

For a test with sand the weight of the container when filled with sand needed to be determined. This was done by hanging a load cell between the container and the crane which was used to lift said container. This load cell had a limit of 1000 kilograms, when filled to the brim the container weighed around 700 kilograms.

5

Description of the experiments

Using the set-up as described in Chapter 4 different tests were done to acquire the data needed to conclude the jet trajectory. The stagnation pressure of the jet will be measured using a pitot tube, to determine the velocity corresponding to this stagnation pressure the density is also needed, as can be determined from Formula 3.28. The density is determined using conductivity sensors. The pitot tube and the rods with conductivity sensors will be attached to the measurement frame to make them easy move and be able to place them in the center of the jet. It should be verified that the rods with conductivity sensors are interpreted correctly, this will be discussed more in-depth in Chapter 6.

5.1. Velocity tests

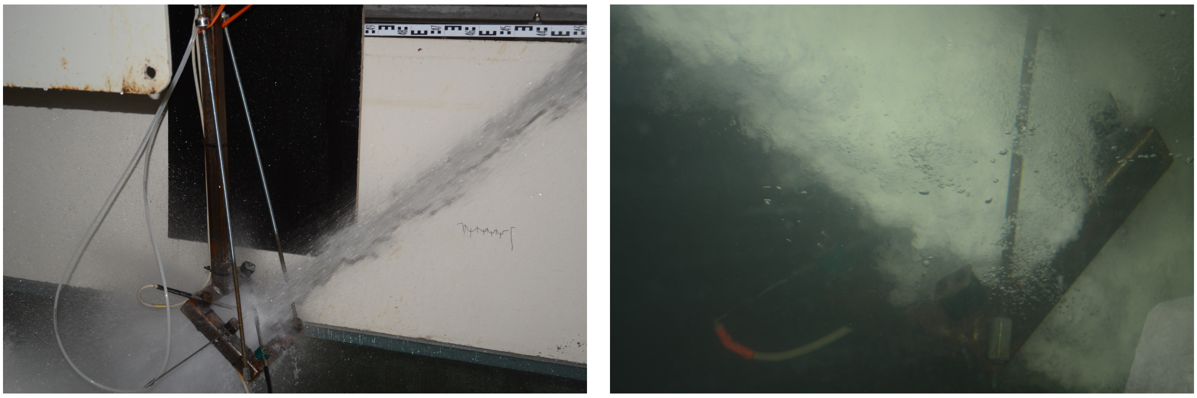

(a) Measurement frame in the air

(b) Measurement frame below water

(c) Measurement at water the line

Figure 5.1: Measurement frame at three different locations

The first test were done with with the four set-ups as described in Chapter 4.3. The measurement frame would be located somewhere in the trajectory of the jet, either above or below water. This test was repeated multiple times using different water height and different distances from the tip of the nozzle to the measuring device. That way a distance profile could be constructed of the velocity of the jet versus the distance above and below water.

Besides the stagnation pressure and density at the centre of the jet multiple velocity profiles were constructed at varying distances. This was done by moving the measuring devices straight through the jet in vertical direction after the center of the jet was found. With this measurement the vertical width of the jet could be determined and the pressure through the jet over its distance. For later tests a peristaltic hose pump was used as well to help and verify the water percentage in the jet measured by the rods with conductivity sensors. This data was not used in the eventual data analysis in this report, this is expanded upon in Appendix F.

Profiles were made of the four different set-ups as mentioned earlier. The most profiles were made of the straight upstream pipe set-up, less profiles were made of the other three set-ups.

5.2. Erosion test

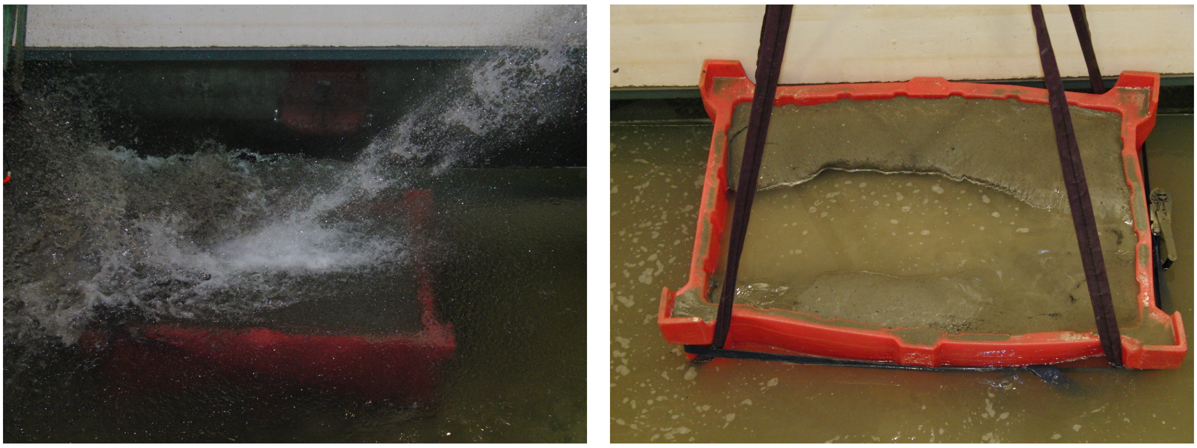

(a) Sand container during jetting

(b) Sand container after jetting

Figure 5.2: Pictures of the sand test

After the tests described above some tests were done including sand, to determine the sand production by the water jet, the sand properties are expanded upon in Appendix G. All these tests were done with the straight upstream pipe set-up. A container filled with sand was jetted upon for 30 seconds at multiple different water heights to determine the influence of the water height on the production of the jet. For this test, the red container, which can be seen in Figure 5.2, was filled with sand. The container has a volume of 107 by 68 by 44 cm. The sand was packed as densely as possible by using a vibrating rod. When it was filled to the maximum the container was lifted using the crane and topped off with water, this was to make sure that the container was always entirely full. Using a load cell between the container and the crane allowed for determining the weight of the sand, water, and container. Then the container was placed at the location of jet impact, where it was jetted on for 30 seconds. After that, it was removed from the flume and again weighed while the container was topped off with water. The difference in weight between the measurement before and after was used to determine the amount of sand removed from the container. Since the container was topped up with water after the experiment the removed weight was sand only, using the difference between the density of water and sand the actual sand production of the jet could be determined.

After the sand was eroded by the jet the frame with the pitot tube was placed at the same location to measure the water density and stagnation pressure at that point. This related the measured production to the stagnation pressure and density corresponding to this location.

5.3. Measurement procedure

All the tests were done in roughly the same way with a consistent order of operations. At the start of each testing day a measurement was done of the rods with conductivity sensors hanging still entirely in the air and then entirely in water, this was done to have a reference measurement for the rods with conductivity sensors for the tests done on that day. The air and water values could change somewhat depending on water temperature or air humidity. Second, the air was vented out of the polyethylene tubing connecting the pitot tube to the Rosemounts, to make sure there were no air bubbles that could distort the pressure measurements. Then all the devices were turned on; the NIDAQ, the transducer, the amplifier, and the volumetric flow rate meter, in some cases Go Pro cameras were turned on as well. After making sure all the programs were running and would save the data correctly the dredge pump was switched on. The cart off of which the measuring frame was hanging was moved into the center of the jet as accurately as possible, a picture of which is shown in Figure 5.3. By moving the cart while reading the live pressure measurements the center could be roughly approached, after which the cart was secured in place. Then the x-y-table on the cart was used to even more accurately approach the center of the jet with the pitot tube by moving the frame in small increments in horizontal and vertical directions. When the center was approached as close as possible the measuring device was secured in place using a tension strap. While all of the devices were running for a few minutes some pictures or videos were shot of the experiment, after which the dredge pump and all of the measuring devices were turned off. The collected data was saved on the laptop with a file with some remarks about the experiment if needed. After the water had settled a laser distance meter was used to determine the distance from the jet nozzle to the pitot tube. In between some tests, some rather big changes had to be made to the setup to be able to measure different settings. Such as changing the height of the attachment of the measuring device on the x-y-table to reach different distances, increasing the water height in the flume to reach different water depths, or changing the set-up from the pump to the jet nozzle by including an S-bend, adding length or using a different nozzle.

The second test, where the sand was eroded from a large container by the jet, had some extra steps. The container was first filled with as much sand as possible, by using a vibrating rod to make the sand as dense as possible. After which the container was lifted by a crane equipped with a load cell to determine the weight of the container and sand. While hanging in the load cell the container was topped up with water to fill the entire volume of the container. When the weight was known it was placed at the location of impact of the jet where it was jetted upon for 30 seconds. Then it was removed from the flume and again hung in the load cell and topped up with water to determine the amount of sand removed by the water jet. After the removal of the container, the frame with the pitot tube was placed at the location where the sand was jetted away earlier to relate the production determined with the weight difference of the container to the stagnation pressure and density measured by the frame at the same location. This was done multiple times with the container and frame placed at the same location but with an increasing water height. This allowed for finding a correlation between the water depth of the sand and the production, both a calculated production and a real production determined with the sand.

5.4. Visually determined jet diameter

To determine the water percentage of the jet at locations close to the nozzle where the frame could not reach high shutter speed images where taken. As shown in Figure 5.4 pictures were taken with a ruler situated below the jet to be able to determine its diameter. Since the volumetric flow rate at the exit of the nozzle is known and the diameter at the distance from the nozzle is known the air percentage at the location where the picture is taken can be determined. The air percentage found this way is the air percentage over the entire width of the jet. It is difficult to accurately determine the width of the jet when

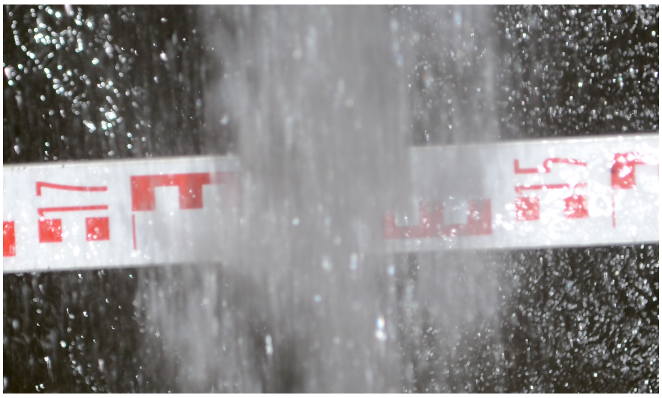

Figure 5.4: Close up picture of the diameter of jet

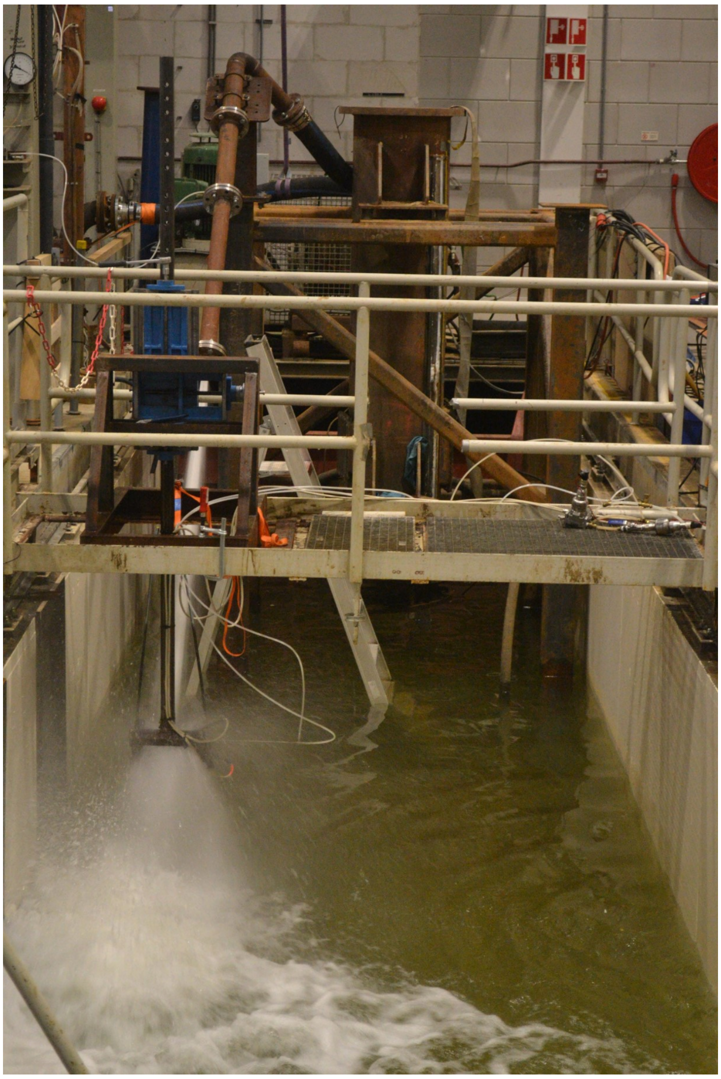

Figure 5.3: The set-up during a test

measuring it against a ruler since it is possible to partially look through the jet and the jet boundaries are not clearly defined, as visible in Figure 5.4. These measurements are used in the graphs where the water percentage is plotted against the distance from the nozzle. Pictures of the diameter of the jet at 0.5, 1, and 1.5 were done for all set-ups, to determine the water percentage for the jets at locations close to the jet where the frame sometimes could not reach. Appendix H shows the determined distances with the corresponding diameters used in the data.

6

Calibration of the conductivity sensors

6.1. Conductivity sensor calibration tests

The assumption made beforehand to interpret the rods with conductivity sensors linearly proved to be false. To find a different way to interpret this data three tests were done where the water and air percentages were known. When measuring with the conductivity sensors during these experiments the data could be related to known water percentages resulting in a new interpretation of the data. The water percentage during these tests was also verified with a peristaltic pump, but due to uncertainty about the accuracy of this pump, they were not used, as is expanded upon in Appendix F.

6.1.1. High water percentage calibration test

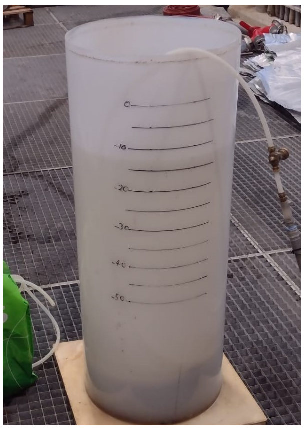

Figure 6.1: The cylinder used for the test

This test, at the high end of the water percentage scale, consists of a large cylinder with a diameter of 40 cm and a height of 1,3 meters partly filled with water, as shown in Figure 6.1. Some more detail about this cylinder is shown in Appendix I. A rolled-up segment of impulse tube with different exits for air was placed on the bottom of this cylinder. On top of the water, a ring was floating with a measurement point attached to it, to determine the increase in volume due to the added air. When the air valve was opened air bubbles entered the water in the cylinder, the increased volume could be determined by eye, by looking at the increased height of the measurement point attached to the ring. Using the difference in volume before and after the air valve was opened the air percentage in the cylinder could be determined. Doing this for different air percentages resulted in the voltage percentage with a known air percentage for water percentages between 80 to 100%. Test with less than 80% water did not work since the limit of air from the air valve was reached and the water started bubbling too much to accurately read the volume indicator.

6.1.2. Medium water percentage calibration test

Another test was done to be able to determine the water percentage corresponding to the measured voltage, by creating a packed bed of gravel in a bucket and then filling that up with water to a predetermined volume and placing the conductivity rod in the bucket, as shown in Figure 6.1.2. This way the amount of grit to water is known beforehand. The grit in this test was dried for 24 hours at 100 degrees Celsius to make sure that there was no water left and that the grit volume was entirely grit. Using the fact that grit and air both do not conduct a current it can be assumed to be comparable. The test was done with three different grit sizes, 20 mm, 10 mm and 5 mm diameters. This gave three different points of water-to-air ratios which can be used to find the water percentage corresponding to a certain voltage. The three tests with different gravel sizes were repeated to find multiple values for the water percentage as a function of the voltage percentage. Images of the three different gravel sizes used in this experiment are given in Appendix J. The fact that the 'air bubbles' or grit don't move over the conductivity rod, in contrast to actual air bubbles, is somewhat negated

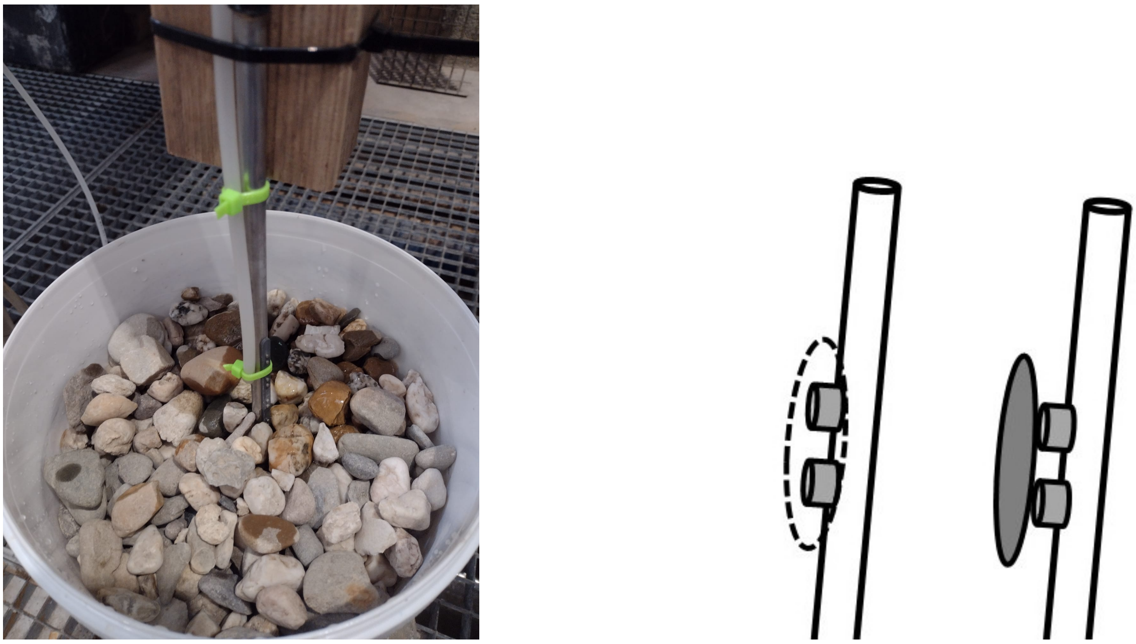

(a) The bucket filled with gravel (b) Gravel and air blocking the conductivity sensor

Figure 6.2: Images of the gravel tests

by moving the conductivity rod up and down. This roughly simulates the bubbles passing along the conductivity rod. The important difference between the two remains that the air bubbles can cover the conductivity sensors and that way break the conductive bridge between the points, whereas the gravel can not 'fold' themselves over the conductivity sensors. They can increase the bridge distance, but are not able to disconnect the conductivity from one point to the other entirely. As shown in Figure 6.2b, where the left segment of this image shows an air bubble covering around two points and the right part shows a rock resting against the conductivity points. Gravel was used instead of sand to more accurately approach the size of the air bubbles as shown in Appendix K. Knowing the air-to-water percentage in combination with the voltage from the conductivity rod allows for more interpretation of the voltages. The air-to-water ratio of this experiment was between 35% to 45% water, putting it roughly in the middle of the graph.

6.1.3. Low water percentage calibration test

Figure 6.3: A frame from the high speed image test

The velocity of the water jet above water was visually determined by frame-by-frame analysis from a high-speed video, a frame of which is shown in Figure 6.3. The distance over the frames can be recalculated into the distance over time which gives the velocity of the jet at the chosen location, as is shown in Appendix L. From this frame-by-frame analysis the velocity of the entire jet, center, and edges, was determined to all be close to the exit velocity of 26,8 m/s. This was done for air measurements at a distance of 2.3 and 1.9 meters from the nozzle. The velocity, in combination with the measured stagnation pressure, can be used to calculate the density. The velocity as a function of pressure and density as given in Formula 3.28, can be rewritten into a formula for the density as a function of velocity and pressure, this results in Formula 6.1.

$$\rho = \frac{2p}{v^2} \tag{6.1}$$

The density can in turn be split into water and air percentages. Using the water percentages calculated this way they can be plotted against the average voltages measured by the rods with conductivity sensors, resulting in a graph for the voltage corresponding to water percentages of less than 20 percent.

These three mentioned test; the cylinder test, the gravel test and the high speed imaging resulted in three sets of data which can be used to verify the interpretation of the rods with conductivity sensors, as will be explained in more detail in Chapter 6.

The values from the conductivity sensors have to be compared to the air percentage to be able to make use of the measured voltages. The interpretation of this data was tried in multiple different ways.

6.2. Verified water percentages

In Chapter 5 the cylinder test, the gravel test, and the high-speed imaging were described. These three tests yielded three sets of known air percentages at three different locations in the jet's trajectory, the lower percentage of 0% to 30%. the middle segment from 35% to 45% and the upper segment from 80% to 100%. These three data sets were used to find a formula that matches the measured data with the measured voltages.

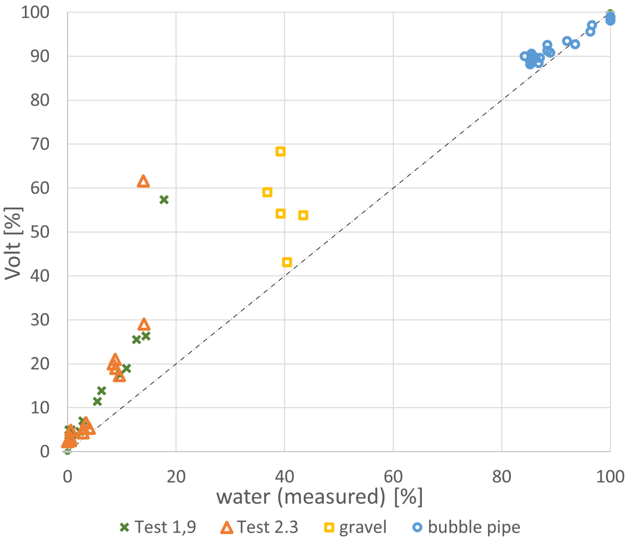

Figure 6.4: All measured water percentages

6.3. Linear interpretation

In Figure 6.4 the points of these tests are shown. Here the water percentage is shown on the x-axis and the voltage percentage on the y-axis. If the correlation were linear all points would fall on the diagonal dotted line. First, a linear relationship between the voltage and the water percentage was assumed. Where 1% of voltage range corresponded to 1% of water at that location. The voltages measured where limited between -3 volt, which corresponds to air, and 10 volts, which corresponds to water. When this was used to interpret the data the values from this were rather unexpected and illogical. This is why the tests from Chapter 5 were done. As visible in Figure 6.4 this resulted in four sets of data that needed to approach the diagonal dotted line. As visible in Figure 6.4 the linear relation seems to hold for water percentages up to 30%, after which the linear relation starts to overestimate the water percentage.

6.4. Threshold method

Another way to look at the data is to count the number of measurements above a certain threshold. Where the measurements crossing the threshold are considered air and the rest is considered water. Since the measurement profile was a consistent base value of water, 10 volts, with spikes reaching towards the air value, -3 volts, but not quite reaching it. The 10 and -3 volts corresponded to the largest range for the conductivity sensors as expanded upon in Appendix D. The value of this threshold was determined by stating that air and water together should be 100 percent since these are the only two elements in the solution. When calculating the air percentage with the height increase of the water column the corresponding percentage of water is also known. When using the volt measurements of the conductivity sensors to calculate the water percentage and adding this to the air percentage the resulting sum should be one. Trying this with multiple different values for the threshold can be used to roughly approach the desired value for the threshold under these conditions. Where for the conditions of this test the addition of the percentages measured and calculated was between 95 and 105 percent for a threshold of 5,69 volts. Where the ideal sum would be 100 percent, but due to inaccuracies in volume measurements by eye a fault margin of 5% is acceptable. One of the conductivity probes gave a permanently higher value than the others. When applying the threshold method to these measurements the percentages were off by 10% compared to the 5% disparity for all other probes. Whether this is due to faulty measurements or a larger range of measurements is unclear. This threshold is only applicable to these conditions with these specific maximum and minimum voltages. But it should be applied in such a way that it is also applicable to the other measurements where the maximum and minimum values of the voltage differ from the ones of this test. Calculating the percentage above and below the threshold might be used to find the thresholds which can be applied to the other measurement, which in this case resulted in the lower 82,5% being water and the upper 17,5% being air. Plotting the resulting density from the determined percentage of air and water for multiple different nodes against the density when determined using the height increase of the water column should in ideal conditions result in a diagonal graph through zero with a slope of one. After doing this for multiple measurements from the last performed tests the points seem to approximate this hypothesis. And the points are crowded around the imaginary diagonal through zero. The points measured during these tests are all in the high water percentages. With water concentrations between 80 to 100 percent. Due to the nature of the set up a further increase in air concentration made the container overflow and made the device used for reading the height increase heave even more, making it less accurate. To make sure the trend line estimated at the top of the graph holds for the entire spectrum the bottom part should be verified as well.

The reverse from the threshold section from below water could be true above water. Where there is a threshold for which the part above it should be considered water and the part below the threshold should be considered water. The NiDaq measurements in the above water case had air as a baseline, -3 volt, with spikes towards the water, 10 volt, which is the reverse of the below water case. The threshold of the submerged measurements where verified with the conductivity measurements in the cylinder as described in section 6.1.1. There was no such water percentage verification with water suspended in the air. The velocity above water was determined to be close to the exit velocity by frame-by-frame analysis from high-speed imaging. Finding the percentage of the threshold by using the stagnation pressure and the known velocity resulted in considerable threshold fluctuations for a different location in distance from the nozzle and center. Which made this method unreliable when determining the water percentage while in the air

6.5. Vinke interpretation

The rods with conductivity sensors were also used by [Vinke, 2009] in his experiments. Here the rods were used at a different range, from -5 to 3 volts instead of the -3 to 10 volts used in this report. The water percentage plotted against the voltage is roughly linear, with a single bend in the middle. Recalculating the voltage measured between -3 to 10 as a corresponding value between -5 and 3 gives a corresponding water percentage according to Vinke's interpretation. The resulting water percentages seemed to match for high water percentages but were not as accurate for the other water percentages.

Applying the formulas found by Vinke to the water percentage in the air gives too high velocities of the jet above water. The resulting velocities above water are higher than the exit velocity of the jet, which of course is not possible. From this, it can be deduced that the equation from Vinke doesn't hold at low water percentages.

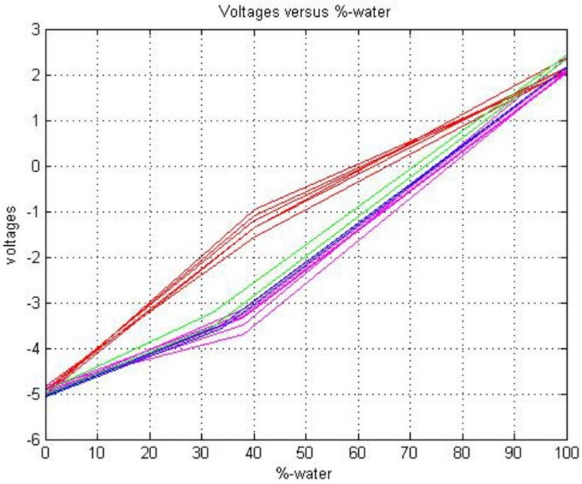

Figure 6.5: Conductivity sensor interpretation[Vinke, 2009]

6.6. Maxwell equation

An equation about the sand percentage deducted from the conducting fluid from the mixture is given by [Talmon, 2011]. Based on earlier research by [Maxwell, 1881]. The Maxwell equation determines the sand percentage as a function of change in the conductivity of the fluid due to mixing in of a non-conductive substance into the conductive fluid. This results in Formula 6.2.

$$c_{sand} = \frac{2 - 2\frac{\sigma_m}{\sigma_{carrier}}}{2 + \frac{\sigma_m}{\sigma_{carrier}}} \tag{6.2}$$

Where c_{sand} is the volumetric concentration of sand, σ_m is the conductivity of the mixture and $\sigma_{carrier}$ is the conductivity of the carrier fluid. The situation researched in this report is comparable to the formula of Maxwell since the sand particles and air are both non-conductive. In Figure 6.6 the water percentage according to the Maxwell equation is plotted against the water percentage determined from the tests done. In the lower quadrant, the water percentage is determined from the high-speed images. In the middle part the water percentage where the gravel was mixed in the water and the high percentage in the cylinder with air. As is visible here the Maxwell equation overestimates the water percentage in the middle of the range but is more accurate near the 0 and 100 percentages.

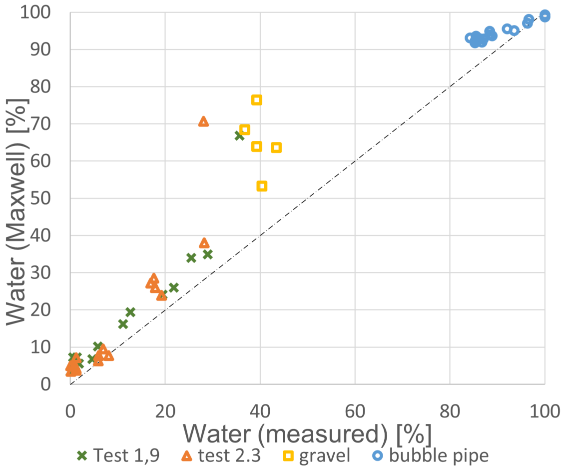

Figure 6.6: Interpretation according to Maxwell

Since the Maxwell equation is based on the conductivity of the mixture compared to the conductivity of the carrier fluid, applying its reverse on water parts in the air quickly falls apart. Since then the mixture contains small water bubbles and the carrier fluid is air, which has no conductivity. This causes the $\sigma_{carrier}$ in Formula 6.2 to be equal to zero and so have to divide by zero and is thus not applicable above water. When looking at this scenario as a water mixture with a lot of non-conductive material mixed in it appears to be too much non-conductive material which in turn does not allow the water to form a complete conductive bridge.

6.7. Bruggeman equation

The Bruggeman equation, as shown in Formula 6.3 was applied to the measured voltages as well. The Bruggeman equation depends on the increased distance needed to create a conducting bridge between points when a non-conductive material is mixed into a conductive material. [Tjaden et al., 2016] expanded on Maxwell's equation for particles of differing sizes. Where different particle sizes are seen as different solutions in the mixture and summed to create a solution with particles of different sizes. Bruggemans model is more catered towards systems with a range of particle sizes. For air bubbles in water the range of differing bubbles is relatively small, when visually determining the size of bubbles during the cylinder test the bubbles were very uniform in size. The Bruggeman model gives slightly lower values than the Maxwell equation.

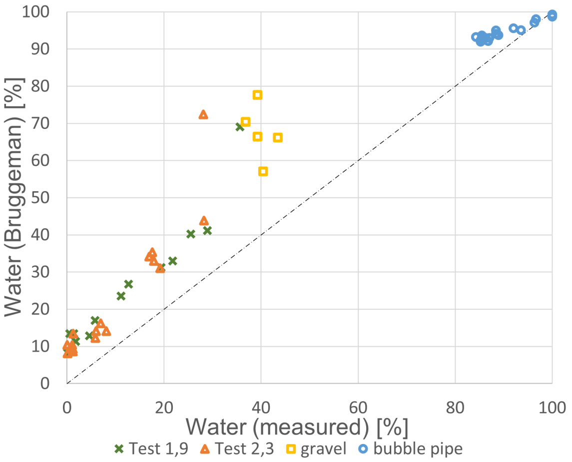

Figure 6.7: Bruggeman interpretation

$$\frac{\sigma_{eff}}{\sigma_{liquid}} = \epsilon^{\frac{(1+n)}{n}} \tag{6.3}$$

Where σ_{eff} is the conductivity of the mixture and σ_{liquid} is the conductivity of the liquid where the less conductive material is mixed in. The n is 2 because the non conducting material is assumed to be circle. The ϵ is the percentage of the conducting liquid. As shown in Figure 6.7 the equation overestimates the water percentage in the lower and middle segment of the graph.

The Bruggeman equation was applied over the entire range of the jet. At high and low water percentages it overestimated the amount of water. This could be due to only the mixture conducting electricity and the mixed in material, air, not conducting at all. Where the formula takes the conductivity of the mixed in material as a part of the function which in this case is taken as zero.

6.8. Archie's law

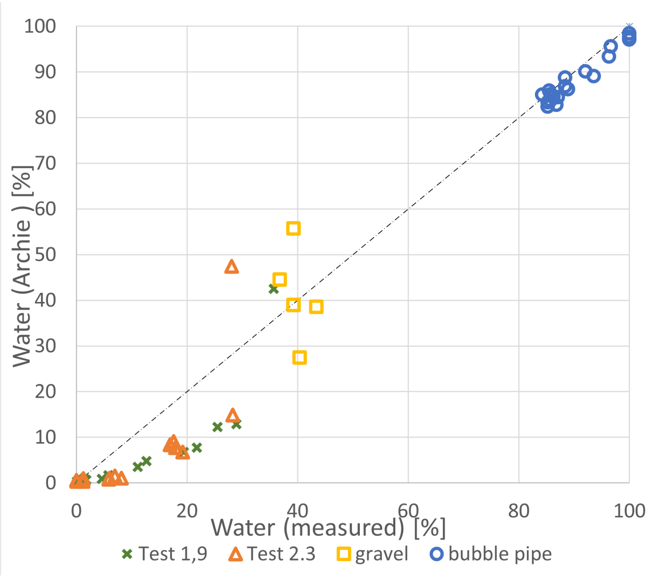

Figure 6.8: Archie's law interpretation

Archie's law, [Archie, 1942] gives the in situ electrical conductivity, C_t of a porous rock as a function of its porosity, n_0, and its fluid saturation, C_w, as shown in formula 6.4. Where the porosity is to the power of the conductivity exponent of the rock, m, and n is the saturation exponent. Archie's law gives the electrical conductivity as a function of the water saturation of the mixture whose conductivity needs to be determined.

$$C_t = \frac{1}{a} C_w n_0^m S_w^n \tag{6.4}$$

In the case of water jetting there are no rocks present so the rock conductivity exponent is set equal to zero, which leaves the fluid saturation. This can be assumed to be the amount of air left in the rock which is taken as the amount of air left in the water. These assumptions reduce the formula to a constant times the fluid saturation to the power of the saturation exponent. This results in a formula which relates the water percentage to the voltage as a function of the voltage to the power of 1 over a constant, as shown in Formula 6.5.

$$W_p = (\frac{V_{avg} - V_{min}}{V_{range}})^{1/c} \tag{6.5}$$

Here W_p is the percentage of water, V_{avg} is the average voltage during the measurement, V_{min} is the minimal voltage, V_{range} is the range of voltages and c is a constant that was determined by fitting the formula different times over the known values. This resulted in a value of 0.65 for the constant c.

As visible in Figure 6.8 Archie's law approximates the diagonal line well for the high water percentages but underestimates it for low water percentages. This might be due to the low water percentage measurements coming from measurements in air where the conductivity sensors are generally less reliable, which is expanded upon in the discussion, Chapter 9. These points are also determined in a different way from the other two data sets as discussed in Chapter 4.3.

6.9. Measurement interpretations overview

Below the waterline, where the amount of water is much larger than that of air, most of the above mentioned formulas resulted in roughly the same values for air to water percentages. Where Archie's Law and the Maxwell Equation seemed to match the best with the found values between 80 to 100 percent of water, when compared to the values found using the cylinder test. For the low air percentages, 0 to 30 percent, the formulas all fell short and were unable to be corroborated using the data found from the cylinder test. This resulted in reasoning backwards from the velocity to the water percentages by using the high speed imaging. This gave a relation between the water percentage and the voltages of the conductivity sensors for low water percentages. This left a large gap in the middle of the graph between water percentages of 30 to 80 percent. Using just these two data sets a clear model describing the range from 0% to 100% was not found. Instead of using two models which would intersect each other around the 45% mark a third test, the gravel test, was done to bridge the gap between 30% and 80%. Archie seemed to match the three data sets more accurately than the other explored options. The constant in the power of Archie's law allowed for tuning of the formula to relate to the data points as close as possible.

For a value of 1 for the power in Archie's law the velocities of the jet are around the $26m/s$ mark. To confirm the accuracy of this approach the water percentages at different distances from the center were determined, by using the other measurement points as visible in Figure 4.9. By determining the water percentages at different distances from the center the total volumetric flow rate could be determined. This was done by determining the water percentage at each measurement point and then weighing them according to the percentage of the total surface this theoretical ring occupies. Since the surface over which the measurement water percentage is applied increases with increasing radius faraway points weigh heavier than percentages closer to the jet center. The calculated water percentage was compared to the theoretical water percentage and the percentage determined from the images of the jet diameter, Figure 5.4.

For a value of 1 in the power of Archie's law the calculated volumetric flow rate was twice as high as the volumetric flow rate at the exit of the nozzle. When the same was calculated for a power of 0.65 the calculated volumetric flow rate matched to theoretical volumetric flow rate. But when calculating the velocity of the jet the velocities were twice as high as the velocity which followed from the high speed imaging. For the data to result in velocities that matched the theory and high speed imaging the calculated velocities had to be divided by 2. Which is why a factor was added.

6.10. Applied factor to interpretation method

The model most approaching these three measurement points was Archie's law. Changing the power in Archie's law allowed the model to either approach the measurement points near the 100% correctly or the points near the 0% correctly, depending on the value chosen in the power of the formula. When adding the points determined around the 40% mark the model approaching the 100% proved more accurate. This left the points near the 0% mark out of line. These points were determined by visually determining the velocity using high-speed imagining and using the pressure at this location to reason back to the air and water percentages. If there is an inaccuracy in these measurements it is most likely at the low water percentage. When multiplying the low water percentage points by a factor of 2 the points more closely approach the proposed line. This result can be reached by either multiplying the water percentage by two or adjusting the pressure or density that was used to determine the water percentage through high-speed imaging, which is the more likely solution. The reasoning behind this is discussed more in-depth in Chapter 9 and Appendix M.

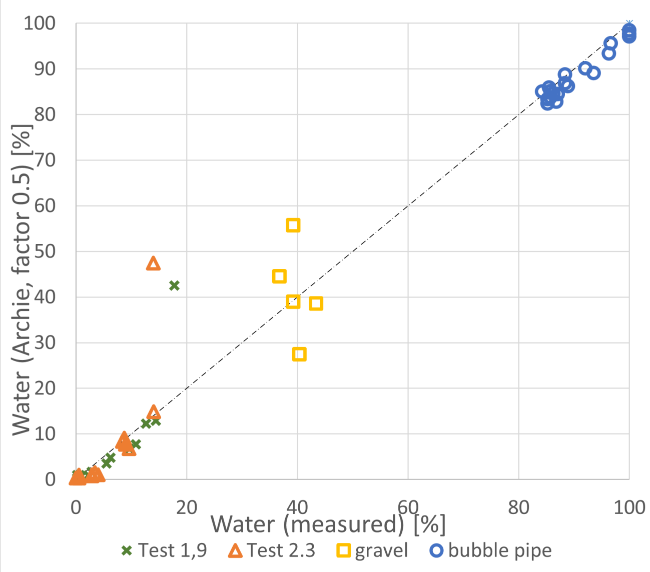

Figure 6.9: Archie's law with factor 0.5 interpretation

When applying a factor over the pressure of the measurements the mathematically determined water percentages are closer to the experimentally determined water percentages at the low water percentage. Since the gravel and cylinder test did not use pressure to calculate the water percentage those points remain the same.

7

Results of individual configurations

For all the jet configurations the same graphs were plotted using the data acquired during testing and given in Appendix E. Some measured points were left out in this chapter due to unreliability these are shown in Appendix N and O. The profiles are given with the center of the jet occurring at the largest stagnation pressure. The center of the jet in the water percentage jet is next to the peak of the profile. This happened in almost all measurements. To correct this the water percentage graphs are moved so that the peak also corresponds to the largest water percentage, this was 10 mm, this was equal to the distance between two measurement locations. This was most clear by the percentage profile above water, where the other water percentage profiles have been moved by the same distance. The resultant velocity profiles are calculated using these slightly moved graphs. The resultant profiles for if the percentage graphs were not moved are given in Appendix P.

First, the profiles of the measured stagnation pressure and water percentage are given. Using these values the resultant velocity profile can be plotted. The last graph is the measured density and calculated velocity of the center of the jet at certain distances in the jet traveling direction from the nozzle. Where the jet traveling direction is taken as the line continuing straight from the nozzle under the same incline of 40 degrees.

7.1. Velocity profile for straight configuration in air

The water percentage over the distance is decreasing rather fast, as visible in Figure 7.1d. Indicating the amount of air quickly entrained into the jet over its trajectory. Showing that even at short distances air is quickly entrained into the jet. Graphs 7.1a and 7.1b show the small center of the jet where there is still a lot of water. The water percentage and its pressure quickly reduce when moving away from the center of the jet.

As visible in Graph 7.1c the jet velocity crosses the 26,8 meters per second line, which is the exit and maximum velocity possible of this jet. This is likely due to the very low water percentages, as shown in the water percentage graph, for which the pressure is compensated. This results in a very high total pressure, in turn resulting in too high water velocities. These velocities in reality are lower, as determined by high-speed imaging.

7.2. Velocity profile for straight configuration below water

The measurements under water are a continuation of the measurements above water mentioned in Chapter 7.1. These show the velocity and water percentage after the jet has pierced the waterline. For the measurements done below water, there were multiple different measurement depths and water heights used. The measured percentages and velocities are shown in Figure 7.2. Where the pressure profile and water percentage profile are shown in Figures 7.2a and 7.2b respectively. Combining these two graphs results in the third profile of the velocity over the distance from the jet center. Noticeable is the velocity profile of the jet at a water depth of 0.29 m, which results in the largest velocity. When looking back at the pressure and water percentage profiles the water percentage is very low above the water jet, this might be due to the entrained air leaving the jet at the upper side of the jet. This low water

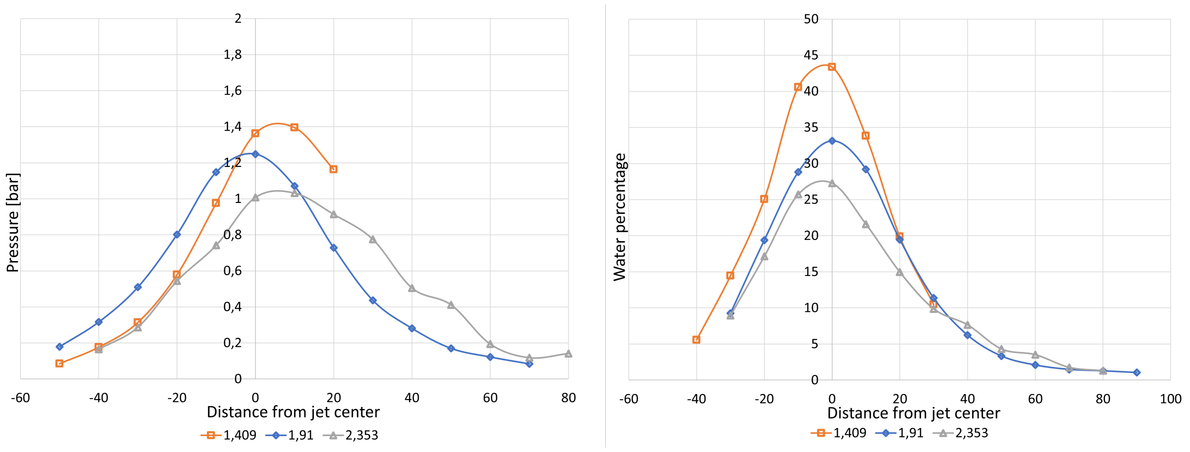

(a) Pressure profile

(b) Water percentage profile

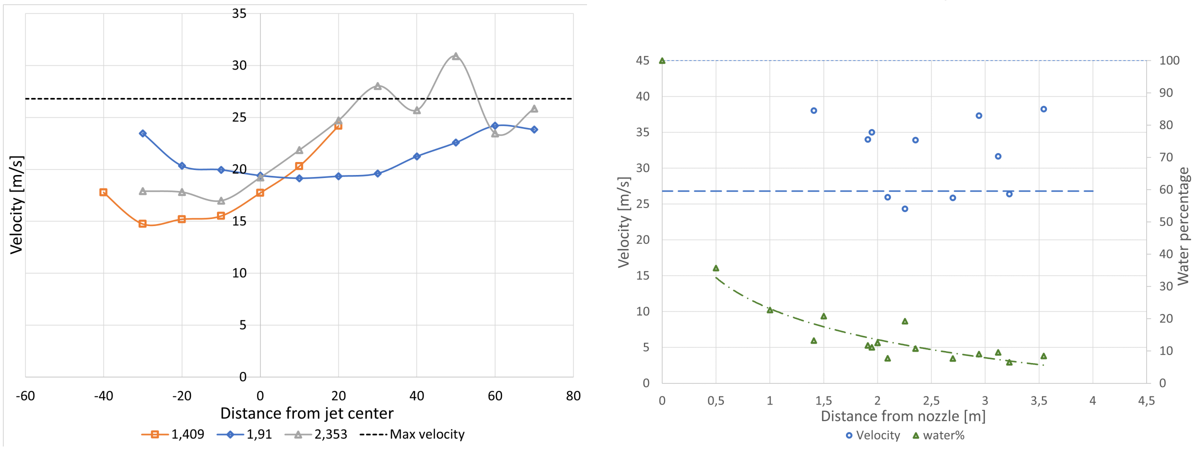

(c) Velocity profile

(d) Velocity and water percentage at distance

Figure 7.1: Graphs for the straight configuration above water at three distances from the jet nozzle in the jets trajectory ($D_n = 2.5cm, p = 3.6bar$)

percentage resulted in large velocities during the data analysis. Besides the low water percentage, the jet pressure is seen to be much larger than that of the next-located jet. This could be due to the jet center better approaching the pitot tube when compared to the slightly less deep jet measurement. The high pressure can be explained due to the jet practically functioning as an above-water jet since the water depth is so small. Since the velocity and pressure approach that of a jet in the air. When the water depth above the pitot tube was shallow enough the pitot tube was visible from the shore and seemed to not be submerged at all, as shown in Figure 5.1c.

In Figure 7.2d a profile is shown with a small part above water and then the evolution of the jet after penetrating the waterline. Where the water percentage matches with the one above water from Figure 7.1d, but with a sudden increase as soon as the jet hits the water. And the velocity decreases as soon as the jet hits the water.

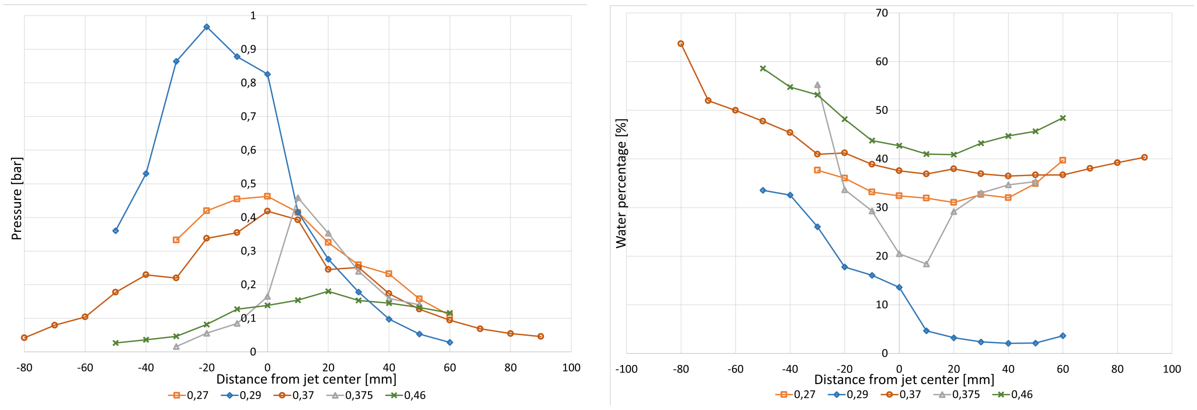

(a) Pressure profile

(b) Water percentage profile

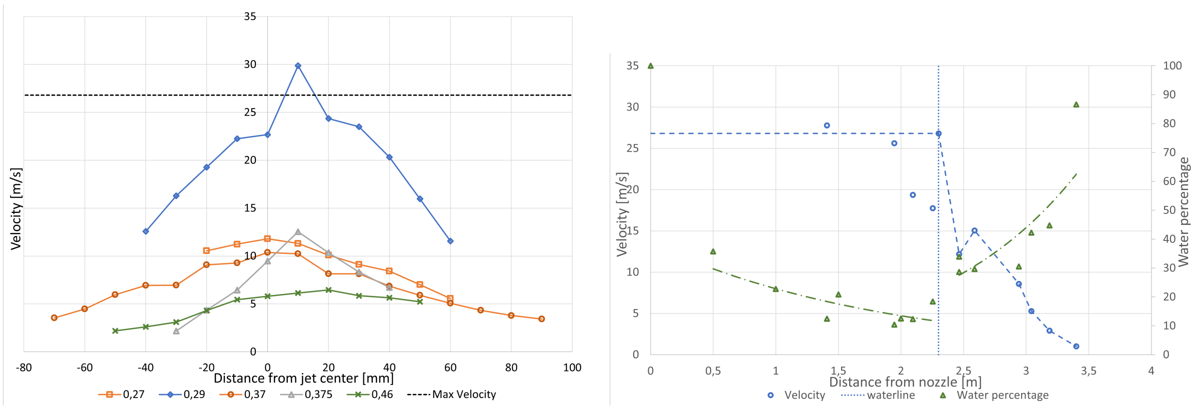

(c) Velocity profile

(d) Velocity and water percentage at distance

Figure 7.2: Graphs for the straight configuration below water at five water depths ($D_n = 2.5cm$, $p = 3.6bar$)

7.3. Velocity evolution for middle bend configuration

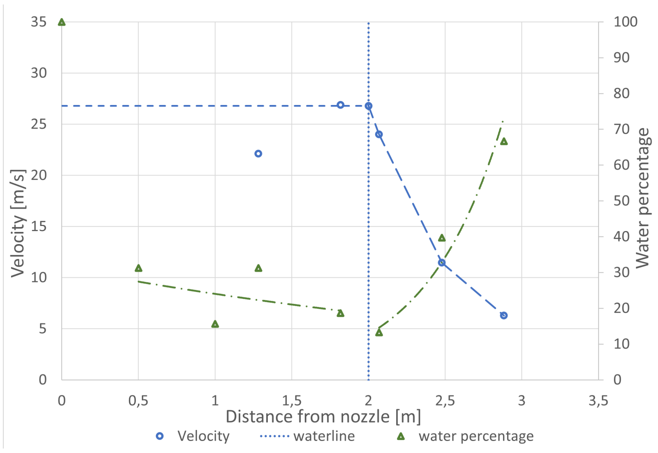

Figure 7.3: Velocity and water percentage evolution of the middle bend configuration ($D_n = 2.5cm$, $p = 3.6bar$)

In this middle bend configuration there is a straight piece of pipe after the S-bend before the water reaches the nozzle, as shown in figure 4.2 and Figure 4.4. This part helps to reduce the secondary flow induced by the bend before the jet exits the nozzle. As shown in Figure 7.3, the velocity of the jet decreases roughly the first meter after hitting the water line, while the water percentage increases when the air entrained by the jet, while above water, floats towards the water surface. When comparing this jet with the straight inflow jet the water percentage seems to increase more quickly. The profile graphs of both bend configurations, with and without the pipe after the bend, are shown side by side in Figure 7.4 where they are compared more to determine the influence of the secondary flow.

7.4. Velocity profile for both bend configurations

In Figure 7.4 the graphs from both S-bend configurations are shown side by side. From this, the reduction in secondary flow due to the straight piece of pipe can be seen. Where from Figure 7.4a the difference in pressure between the two configurations is clear, where the middle bend configuration has a clear pressure peak and the end bend configuration does not. Combining this graph with the water percentage graph from Figure 7.4b results in a graph that shows the two velocities side by side in Figure 7.4c. The water percentage graph has more water below than above the center of the jet, as is expected due to the buoyancy of the entrained air bubbles. The difference between the two water percentages is also likely due to the end bend configuration entraining more air while above water, as visible in the jet images shown in Appendix Q. The resulting velocity of the end bend configuration crosses the profile of the middle bend setup. This is likely due to the low water percentage measured at this location. Some points are left out of this graph since the large velocity at a large distance from the jet center seemed unlikely, this data is shown in Appendix R.

From Figure 7.4d the low water percentages before the jet hits the water is visible. The water percentage measured by the middle bend configuration, shown in Figure 7.3, is much larger. which corresponds to the visually determined air percentage being much larger in the end bend configuration than the middle bend configuration, which also follows from Figure 7.4b. The velocity of the jet seems to decrease slightly quicker for the end bend configuration as well.

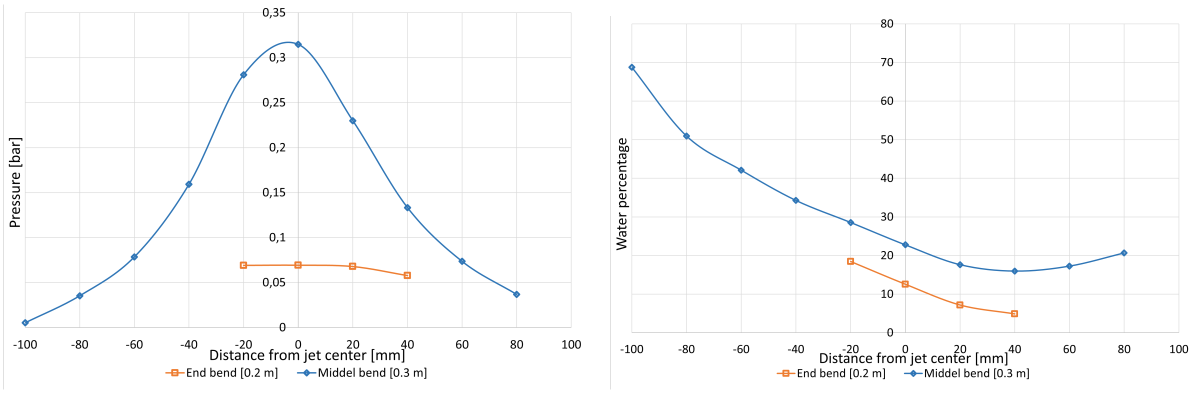

(a) Pressure profile

(b) Water percentage profile

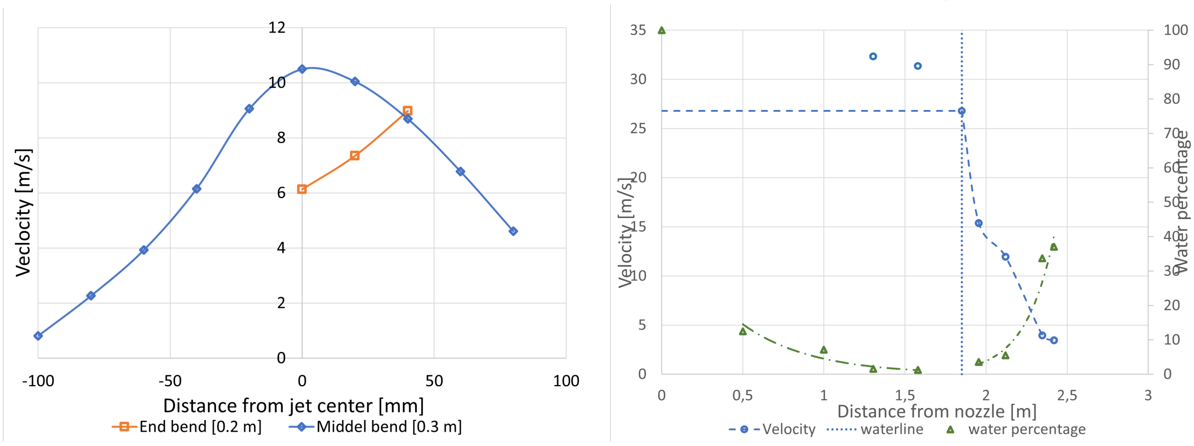

(c) Velocity profile

(d) Velocity and water evolution of the end bend configuration

Figure 7.4: Graphs for both the bend configurations at two distances below water ($D_n = 2.5cm$, $p = 3.6bar$, $H_n = 1.8m$)

7.5. Velocity profile for flap configuration

Figure 7.5a shows the pressure profiles of three distances from the flap configuration. These are all relatively close together. Figure 7.5b shows the water percentage of this flap which is very low for the two closes measurements. And relatively large for the furthest measurement. The low water percentage for the closes two is likely due to the large amount of air entertainment for this jet. As shown in Appendix Q the jet is very wide and has a lot of air in it which it entrains into the water. Likely a lot of air is entrained of a short amount of depth after which the stagnant water increases the percentage. Figure 7.5d shows a quick water percentage increase after the waterline is penetrated. There are few

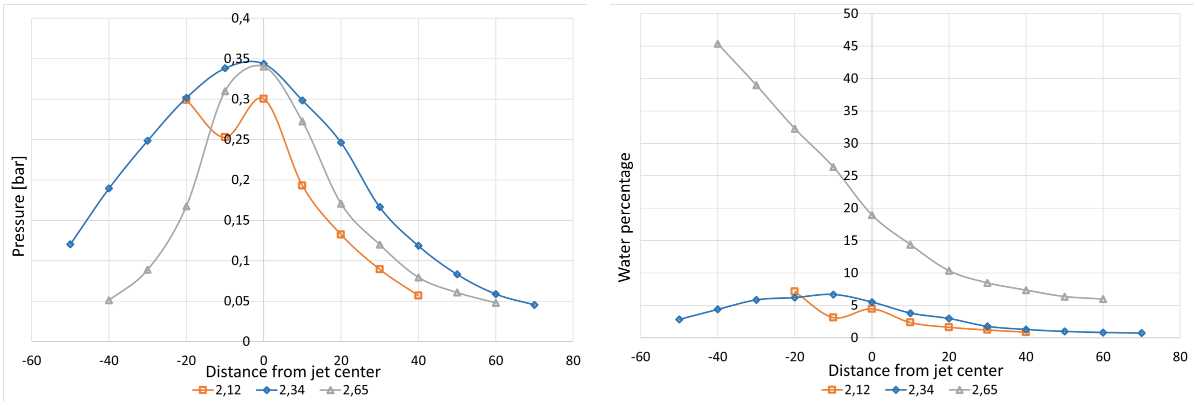

(a) Pressure profile (b) Water percentage profile

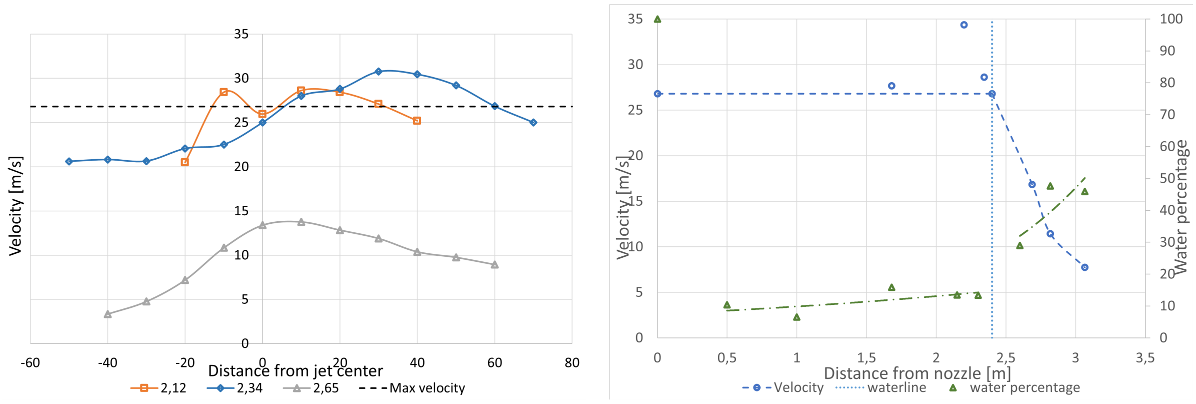

(c) Velocity profile (d) Velocity and water percentage at distance

Figure 7.5: Graphs for the flap configuration above water for the upper two and $0.1m$ below water for the jet at $2.65m$ distance ($D_n = 2.5cm$, $p = 3.6bar$)

data points below the waterline but the water percentage seems to quickly increase. This would explain the high water percentage form the furthest measurement point from Figure 7.5b

As visible in graph 7.5d the jet velocity after hitting the water line drops quickly. Where in the first half a meter it reduces from 26,8 to 5 meters per second, with the density increasing rapidly over the same distance.

When looking at the velocity and density profile, shown in Figure 7.5c and Figure 7.5a respectively, the velocity in the centre of the jet seems to decrease quickly over distance, especially after penetrating the waterline. Where the water percentage is also seen as very low above water at the first two distances from the nozzle and the high at the furthest measurement from the nozzle. Where the air bubbles are seen to rise towards the water surface as evident by the large density discrepancy above and below the jet centre in the density profile graph.

7.6. Remarks velocity profiles for all configurations

The velocity profiles sometimes cross the 26,8 m/s boundary which should not be possible. When this happens the water percentage profile shows low water percentages. This seems to imply that at very low percentages the interpretation of the conductivity rod data, in combination with the stagnation pressure, is still somewhat insecure. Though this seems to be mostly the case at very low water percentages.

The profiles also show a water percentage difference between the upper and lower part of the profile. This is due to the entrained air bubbles rising to the water's surface. Which reduces the water percentage above the jet center. This somewhat influences the pressure profile, as can be seen in Figure 7.1a, where the pressure seems to reduce quicker above the jet than below it.

In Appendix S pictures are shown of the jet when exiting the nozzle. These pictures show the the distance over which the diameter stays equal for the different configurations. Noticeably the width of the jet is roughly constant for the straight and the middle bend configuration. The end bend configuration increases in size very quickly, due to the rotating motion of the jet when exiting the jet nozzle. The width of the flap configuration increases immediately after exiting the nozzle due to the flap preventing any of the water to move upwards and flattening the water jet. To have the same volumetric flow rate while the height at the exit gets reduced makes it so that the width increases.

Appendix Q shows a picture of the jet from the nozzle to the water surface. From these images the increase in diameter from the different configurations is visible. Where the end bend configuration is the widest jet as corresponds with the low water percentages above the water line as determined in Chapter 7. Followed by the flap setup, then the middle bend setup, with the straight configuration being the most coherent. This matches the water percentages above water discussed in Chapter 7. Below water, this trend continues as shown in Figure 8.2b. Where the end bend configuration has the lowest water percentage and thus the most air entrainment.

7.7. Erosion evolution for the straight configuration

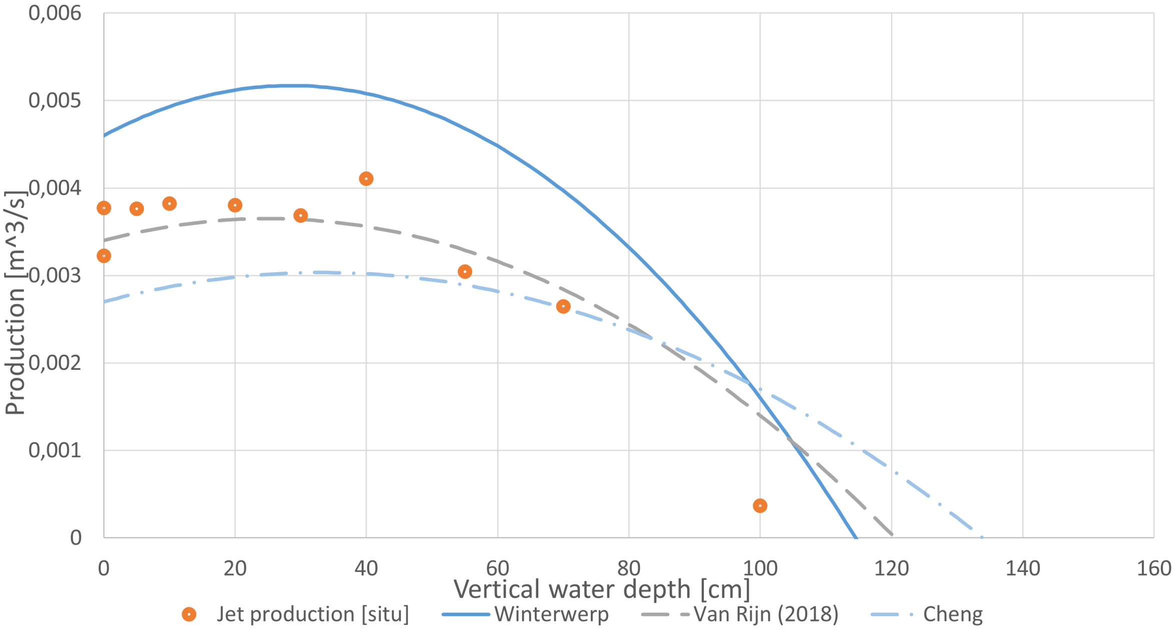

Figure 7.6: Jet production evolution at increasing water depths

The erosion of the jet with the entirely straight configuration was plotted against the vertical distance below the water line to determine the erosion of the jet at different water depths. This gives the observed erosion velocity and the calculated erosion velocity using the water percentage and stagnation pressure that were measured at the same location where the sand was eroded using the measurement frame. The calculated production was determined using the pick-up functions of Winterwerp, van Rijn (2018) and Cheng, as mentioned in Chapter 3.9. These formulas were used since these pick-up functions are in the same order of magnitude as the measured production. These two pick-up functions usually underestimate the erosion according to [Heijmeijer et al., 2022]. The jet in this report is much less ideal than the straight, fully submerged jets on which these functions are based, which is why it makes sense that these functions are in the same order of magnitude. The results are shown in Figure 7.6, with the water depth on the x-axis and the erosion velocity on the y-axis. Where the sand or measurement frame was always at the same height and the water level was the only variable. Plotted here is the erosion as determined by the sand container test with beside it the production as according to van Rijn (2018), Winterwerp and Cheng. From the graph it follows that the influence of the first halve a meter of water above the sand has very little influence on the production of the jet. This might be due to the entrained air forming a sheath around the jet at the start so the stagnant water does not decrease the velocity as much.

8

Analysis of configurations side by side

8.1. Analysis for all configurations side by side

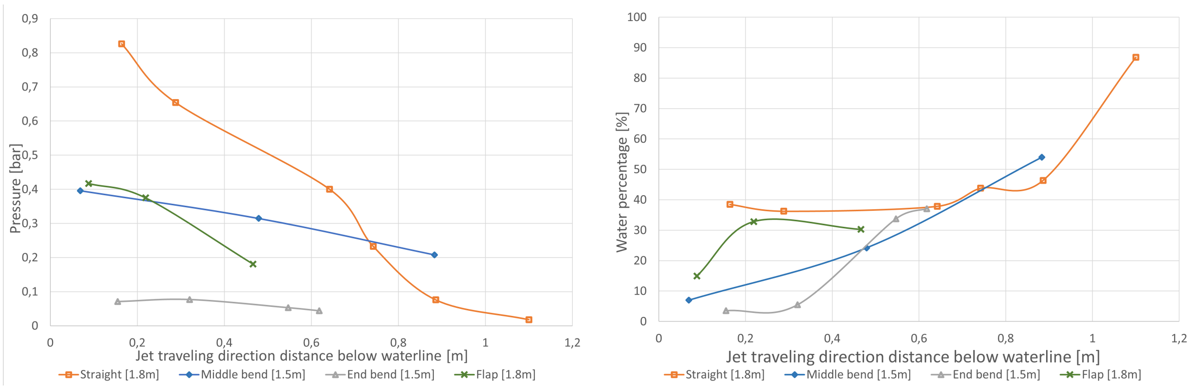

(a) Pressure evolution

(b) Percentage evolution

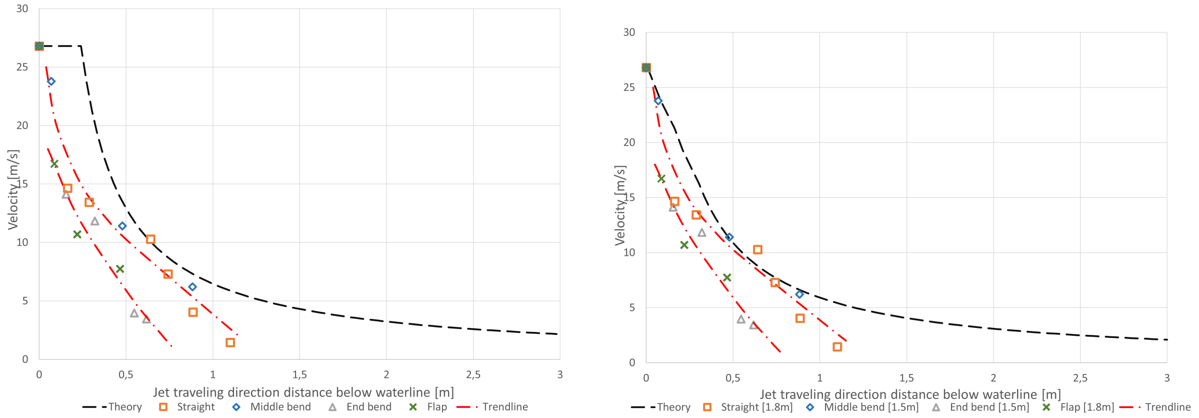

(c) Velocity evolution with a development zone

(d) Velocity evolution without a development zone

Figure 8.1: Jet properties evolution in the traveling direction of the jet at vertical water distances ($D_n = 2.5cm$, $p = 3.6bar$)

Figure 8.1a shows the stagnation pressures of the different configurations at different water depths where the water depth is expressed as the distance below water in line between the nozzle and the frame, so with a diagonal under a 40-degree angle. Here a clear difference between the four configurations is shown just like the pressure over distance as given in Figure 8.2a. Where the pressure of the straight setup is the largest, with the middle bend and the flap being comparable and the end bend configuration exerting the lowest pressure.

Next to this, the water percentages at the same locations are shown in Figure 8.1b. The order from largest to smallest water percentage follows that of the pressure from straight to flap and middle bend to end bend. All increase in water percentage until all the air bubbles have floated upwards and there is little velocity left in the water.

Combining the pressure and water percentages gives the velocity as shown in Figure 8.1c where the four configurations are shown in the same graph. Here the velocity is plotted against the jet traveling direction that the jet has traveled below the water line, in the continuation of the jet at a 40-degree angle. The black dotted line is the theoretical velocity according to Formula 3.15. Figure 8.1d shows the same graph but for the jet without a development zone, where the jet velocity according to the theory approaches the higher of the two trend lines. All four different configurations are very close to each other, but there still seem to be two different groups of velocity evolution. This is shown by the two red trend lines through the dots. Where the upper trend line follows between the straight and middle bend data, and the lower trend line follows between the end bend configuration and flap data.

The velocity of the flap and the end bend configuration decrease in velocity the quickest, with the flap being slightly quicker in reducing its velocity. The straight setup and the middle bend configuration seem pretty close to each other as well. These two appear to be the better options. The end bend configuration looks to perform the worst in pressure and water percentage when looking at Figure 8.1 and Figure 8.2. The flap configuration seems relatively close to the middle bend set up, but has a smaller peak in the pressure graph as shown in Figure 8.2a, and its water percentage seems to reduce slightly quicker than that of the middle bend as shown in Figure 8.2b. The straight set up has the largest pressure and water percentage at the jet center. Both of these are lower for the middle bend configuration but their velocities are still very close together.

The difference between these two groups might be larger than described here since the low performing jet have low water percentages. As mentioned in this report low water percentages are likely to overestimate the velocity, which is why the gap between the two groups might be larger than shown here.

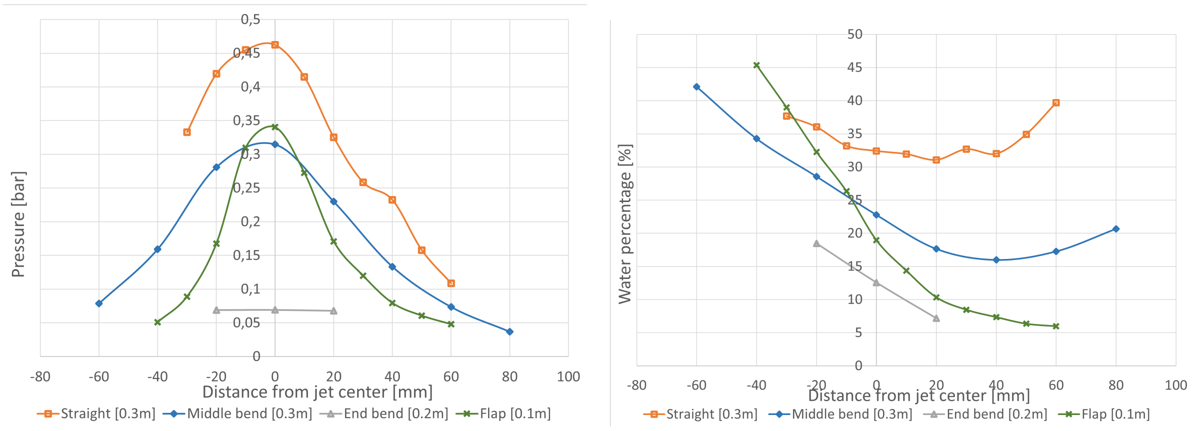

(a) Pressure (b) Water percentage

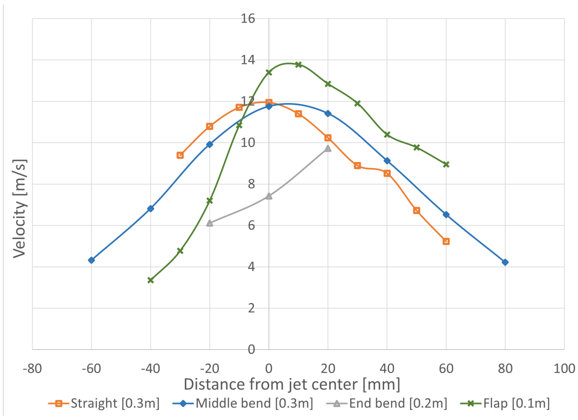

(c) Velocity

Figure 8.2: Jet profiles for all set ups at vertical distances below the waterline ($D_n = 2.5cm$, $p = 3.6bar$, $H_n 1.8m$)

In Figure 8.2a the jets are all roughly at a distance of 2.4 meters from the nozzle and around a depth of 30cm. From here it shows that the pressure of the straight jet is roughly 30% higher than the jet with the middle bend and flap, which are close to each other, but with different jet diameters. With at the very bottom of the graph the end bend configuration, just like in Figure 8.1a. The water percentage order from the profiles in Figure 8.2b matches with Figure 8.1b as well. The velocities are close to each other as well, as shown in Figure 8.2c. Some points were removed from these figures since they were deemed inaccurate due to very low water percentages resulting in very high velocities. The full graphs are given in Appendix N and O.

8.2. Straight upstream configuration analysis

The jet with the straight inflow towards the jet is the jet with the highest pressure, largest water percentage and jet with the smallest width. In the graphs shown in Chapter 7 the underwater velocity of the jet is also shown. As visible in Appendix S the water jet for the straight configuration is the most coherent while above water. The air measured under water is most likely entrained in the jet while in air. where the large contact surface between the jet and the air makes entrainment easy. This air shows up again underwater where it leaves the jet while floating towards the water surface due to its buoyancy. The straight jet entrained less air than the other configurations as can be determined from Figure 8.2b which shows the water percentages of the jets side by side.

8.3. Middle bend configuration analysis

The middle bend configuration is slightly less coherent than the straight water jet set up as visible in Appendix S. Figure 8.2b shows that this jet has the second highest water percentage in the jet center right after the straight configuration. This configuration also about the second largest pressure, together with the flap set up and is the second widest jet after the straight configuration, as can be seen in Figure 8.2a. This is likely due to how similar the middle bend jet configuration is to the straight configuration. The straight piece of pipe after the S-bend removes a lot of the secondary flow induced by the S-bend present in the configuration.

8.4. End bend configuration analysis

The end bend configuration is the least coherent jet, as shown in Appendix S. Due to the water being swirled around in the bend and after that immediately exiting through the nozzle the rotational motion of the water is still present in the jet. This causes the jet to swirl in the air. As visible in Figure 8.2b and 8.2a this set up has the lowest pressure and water percentage of the tested configurations. Looking at the pressure decrease over water depth in Figure 8.1a shows that the pressure of the jet was never very high to begin with. This was also the jet with the most inaccurate measurements due to very low water percentages recorded by the rods with conductivity sensors.

8.5. Flap configuration analysis

This configuration has roughly the same water percentage and pressure at the jet center as the middle bend configuration, as shown in Figure 8.2a. The profile of this configuration is much smaller than the middle bend configuration, as can be seen in Appendix S. The flap flattens the jet the moment it leaves the nozzle resulting in the small jet center visible in Figure 8.2a. In Figure 8.2b it shows that the flap configuration has a high water percentage below the jet center and a low water percentage right above it. Due to the jet center being very small and having more air bubbles above the jet center than below it.

8.6. Comparing the four configurations

The production of a jet depends heavily on velocity, as visible in Figure 8.1c the velocity of the different jets can be split in two groups of comparable velocity. The velocity being comparable can be due to the entrainment of air around the plunging parts of the broken up jet. These entrained air films have a much lower density than the water of the jet and barely reduces its velocity, keeping the velocity constant. When these small jet parts come in contact with water the large density of the water that needs to be entrained by the jet quickly slows the jet down. Making the speed reduction fastest for the jets with the least width. Which agrees with the order of the jets in Figure 8.1c.

The difference in water percentage of the jet, as shown in Figure 8.2b might influence the production of the jet. The water percentage is a part of the erosion velocity formula, as shown in Formula 3.18 where the ρ_m is the density of the mixture of air and water and not purely the density of water. When pure air shears over a sand bed there likely will not be any erosion of sand. If the same velocity over the sand bed would be sheared by pure water instead of air the erosion velocity of the sand bed will likely be much higher. A larger ρ at the same flow velocity will result in a larger bed shear stress. As visible in Figure 8.2b the water percentage of the straight jet is higher than that of other jets and over a larger width than the other jets. The first assumption was that the erosion happening would be better because of the higher water percentage and the larger width of the jet center.

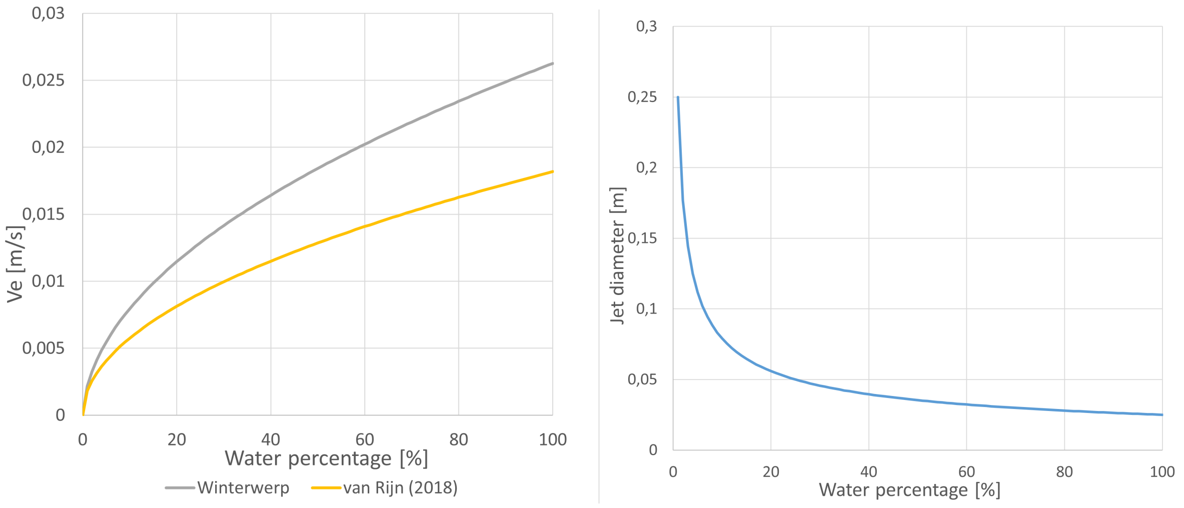

(a) Erosion velocity at $26,8m/s$

(b) Water percentage of a jet with an original diameter of $2,5cm$

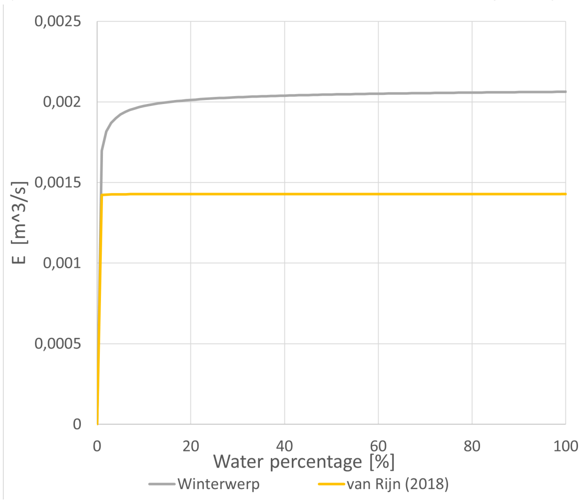

(c) Erosion as a function of the water percentage

Figure 8.3: Erosion of a jet with increasing diameter and reducing water percentage

In Figure 8.3a the erosion velocity is plotted against the water percentage according to Winterwerp and van Rijn (2018) for a jet with a velocity of $26,8m/s$. From this graph, it is clear that a larger water percentage corresponds with a larger erosion velocity.

In Figure 8.3b the jet diameter is given as a function of the water percentage for a jet with a nozzle diameter of $2,5cm$. Where a larger water percentage corresponds with a smaller jet diameter.

Combining these two graphs results in the erosion of the jet as a function of its water percentage, which is shown in Figure 8.3c. This figure shows that from a water percentage of 20% onward the erosion is practically constant. This would mean that the coherence or water percentage of the jet does not influence its erosion.

8.7. Erosion analysis

Chapter 3.11 mentioned the erosion according to Vlasblom with the corresponding formula, given in Formula 3.22. Since all these numbers are known the production according to Vlasblom can be calculated. Theoretical the production of this jet according to Vlasblom is $0.0157m^3/s$. Making it nearly four times as large as the largest measured production according to Figure 7.6. The main difference is that Vlasblom assumed a straight submerged jet, as opposed to a plunging, inclined jet. And the production according to this formula does not decrease over the distance since impulse conservation is assumed. This gives the assumption that the erosion of this jet can theoretically be four times higher than it shows in this configuration.

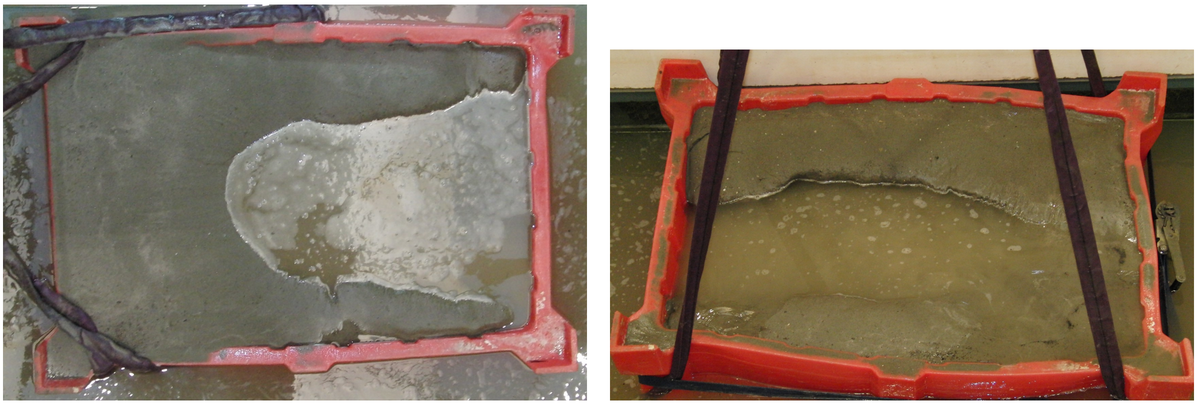

(a) Sand at the water surface

(b) Sand at 0.3 m water depth

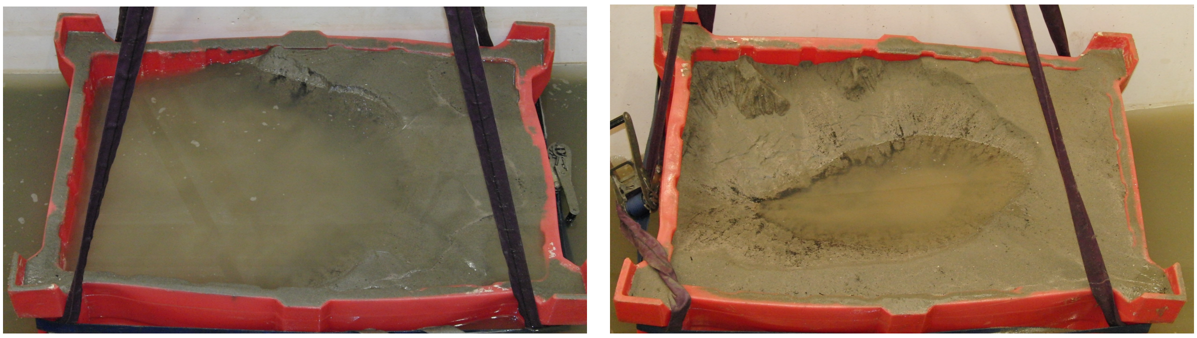

(c) Sand at 0.55 m water depth

(d) Sand at 1 m water depth

Figure 8.4: container after erosion for different water depths, with jet approaching from the left

Noticeably the initial erosion velocity for the formulas increases before it decreases. Appendix N shows the measurement points from which these graphs are plotted. The initial increase might be due to the measurements at the water surface being less accurate due to the low water percentages at this location. Another possible explanation is that the jet is curved slightly upwards after penetrating the waterline. This results in the jet not jetting straight into the sand bed but shearing over the sand bed, as can be seen in Figure 8.4. Here the container is shown after the jetting of the erosion and the resulting sand bed is visible. Figure 8.4a shows the sand when the container was at the water's surface. From this, it seemed that the jet was jetting straight into the sand and created a hole in the length of its trajectory. This would result in a less than optimal production. In Figure 8.4b it looks as if the jet was curved and sheared over the packed sand bed and deposited the sheared sand outside of the container. Image 8.4c seems to show a more sheared hole as well. Image 8.4d seems to have the least production. The sand seems to be sheared away from the container, but the large water depth made the velocity above the bed less than for Figure 8.4b and 8.4c, resulting in less production.

The erosion scales with $n_L^{2.8}$ or n_L^3, as demonstrated in Chapter 3.13. Where n_L was chosen as 0.5. As mentioned in that same chapter the scaling of the production is subject to inaccuracies when compared to the test if it were done at full scale, this is discussed more in depth in Chapter 9.

9
Discussion

Some of the sections of this report allow for speculation about whether the data is entirely trustworthy or if there was possibly an error in data collection or processing.

9.1. Expectations

At the start of this research, the expectation was to find the sections of the set-ups that influenced the velocity at the erosion location the most. During testing, before the data was analyzed, the straight jet set-up seemed to be the most coherent jet and was therefore expected to perform the best. The end bend set-up and flap set-up seemed to entrain a lot of air above the waterline and were expected to have very low erosion velocity under the water. From the conclusions drawn in this report, it seems that the erosion velocity difference between the set-ups is very small, which was not expected during testing. From the data, it follows that the velocity of the jet is roughly the same at water depths with small differences between set-ups. This is likely due to the air entrainment of the jets creating an air layer between the water jet and the stagnant water which has the jet entrain air while below water which does very little to slow down the jet. The difference between the set-ups in measured pressure and water percentage seem to roughly cancel each other when these are used to calculate the velocity, on which the erosion functions are based.

At the start it was also expected that even a small layer of water would have significant consequences for the production of the jet when it reached the sand bed. This was also not entirely true, as shown in Figure 7.6. Where the first halve a meter of water depth barely influenced the production of the jet. This might be due to the air entrained into the water shielding the water from the influence of the stagnant water.

9.2. Accuracy of jet centrum determination

The experiments were all done by placing the measurement devices in the jet center by hand, where the possibility of human error is rather large. The chance of the pitot tube being not in the jet but next to it during at least one of the tests is pretty significant. When the jet at the measurement location was very wide, or the pressure was very low it was difficult to accurately find the jet center. Some mistakes might be made in this aspect.

9.3. Scaling issues

The scaling was done according to Froude since the water segment below the water was regarded as the more important segment, where Froude is the more important factor. Scaling according to Froude was also more approachable than scaling according to Weber. If these tests were scaled according to Weber the results might differ. To know this the tests should be repeated with different scaling or at full scale.

The scaling was done according to Froude, but assuming it was done according to Weber would result in the prototype size being equal, but the pressure assumed for the prototype would be $3.6/2$ bar, which equals 1.8 bar. This corresponds to a velocity of $19m/s$. This is not close to the actual scenario and underestimates the pressure and velocity significantly. Meaning the results presented in this report would not accurately portray the prototype. To verify whether the correct scaling factor was applied here the test should be repeated with scaling according to Weber.

As mention in Chapter 3.13 the scaling of the experiment to the prototype was subject to different scaling factors, resulting in scaling issues between the two. The scaling of erosion was also mentioned in Chapter 3.13 and did not correspond to the desired scaling of the erosion.

9.4. Conductivity senors unreliability

For applying the values measured by the rods with conductivity sensors in the air multiple different formulas were considered, as mentioned in Chapter 6. An acceptable formula was found, but the measurements in the air might not be that reliable. This is likely due to air giving a ’zero’ measurement when it blocks out two measurement points, as shown in Figure 6.2b. This is regardless of the size of the air bubble but happens when the two points can not form a conductive bridge, due to even a small air film. This problem happens in the air but is not present when these rods with conductivity sensors are used in sand, where they are more often used. Since there they can still create a conducting bridge. This means that the water percentage might not always be accurately measured, especially at low water percentages where a lot of air is present.

Most inaccuracies of the water percentage interpretation of the conductivity sensors happened at low water percentages. Making the data with low water percentages the most likely to be incorrect. The method of interpretation of the rods with conductivity sensors can still be improved upon, especially at low water percentages. Since in this report, the most important segments were with larger water percentages the interpretation by way of Archie’s law with a factor was sufficient. For follow-up research, the interpretation of the conductivity sensors can be expanded upon.

9.5. Pitot tube inaccuracies

Since the stagnation pressure measurements at this location were done by a pitot tube in the air with very little water there is room for error at this segment of the set-up. The small amount of water in air measurements was confirmed both by the conductivity sensors and visually. The velocity is determined from the stagnation pressure and the calculated density by using Formula 9.1, which is a rewritten version of Formula 6.1 and Formula 3.28. The transition from air to water is also an imprecise part of the jet trajectory, as mentioned in Appendix N. Where the pitot tube might still entrain air into the tube due to not actually being submerged due to the air sheath around the pitot tube.

$$v = \sqrt{\frac{2p}{\rho}} \tag{9.1}$$

The pitot tube in air has also air coming into the pitot tube and not just water. The air might enter the impulse tube and act like a kind of cushion between the water and pressure sensor. This could dampen the signal and reduce the measured pressure peaks.

The pitot tube measured the stagnation pressure with a sample rate of 1 Hz, this might have influenced the measurement. Since it is not clear whether the pitot tube takes the largest pressure value during this second or averages the pressure out or gives the pressure from a specific moment.

When the pitot tube measured the jet while underwater, it was visible that the jet was jetting in pulses. The jet did not have a constant pressure specifically at larger distances. This might have influenced the pressure measurements of the pitot tube underwater, also due to the low measurement frequency of the pitot tube. In the same way, fluctuating pressure influenced the pressure measurements of the pitot tube in the air as discussed above.

9.6. Water temperature influences

The temperature in the laboratory can have influenced the results of the test. When water temperature increases with 1 degree Celsius the conductivity increases with 2%. This means that the conductivity sensors might have given larger conductivity values on days where it was warmer in the lab. In the experimental set-up the water volume used was rather large and all test were executed during the winter, likely the temperature fluctuations of this body of water were very small.

To offset the temperature fluctuation every testing day the maximum and minimum value of the conductivity sensors were set by measuring in air and water to have the range of the sensors for each testing day. This reduces the influence of the temperature on the measurements but still has some influence on the final data.

For the tests with small water amounts, like the cylinder and gravel test the temperature might have been more influential. For these tests the range of the conductivity sensors was also determined. All cylinder test were conducted on the same day, as were the gravel test. Having very little temperature fluctuation within the test themselves.

10

Conclusions and recommendations

10.1. Conclusion

From the acquired data it became clear that the bend in the set-up negatively influenced the coherence of the jet and added a secondary rotational flow in the exiting jet. Though this negative influence was significantly less when a straight segment was added after the bend before the nozzle.

The flap reduced the coherence and velocity at increasing water depths of the jet. To possibly increase performance in the prototype the flaps should be removed to make the jet more coherent and have a larger velocity than it would have at the same water depths with a flap. This would however create other possible issues regarding the silting of the pipes.

From the graphs in Chapter 7 for all set-ups the velocity decreased significantly after penetrating the waterline, whereas there was little to no velocity decrease before the waterline penetration.

From Figure 8.1c, which shows the velocity of the four configurations below water, it follows that there was some difference between the jets, where the end bend and the flap performed the worst. Whereas the straight jet up performed the best, closely followed by the middle bend set-up. The velocity difference between the two sets might be larger than determined here since low water percentages seem to overestimate the velocity and the two worst-performing jets had very low water percentages. The water percentage followed the same order as the velocity profiles, which means that the air entrainment is much larger at the worst performing jets and were visibly less coherent than the straight pipe lay-out. To more accurately verify the claims made in this report will require more research in the interpretation of the fluid density through the conductivity sensors and the actual erosion of the different set-ups.

When approaching the erosion with water percentage as governing factor by using the pick-up functions of Winterwerp and van Rijn (2018), the data was nearly constant over the entire range of water percentages, meaning that the resultant erosion of all the set-ups is comparable. This might be different for different jet set-ups and would require more research.

The production as determined by the erosion test is barely influenced by the first half a meter of water, this is most likely due to air entrainment by the jet forming a sheath around the water jet which prevents the stagnant water from slowing down the jet velocity.

10.2. Recommendations

According to the fluid flow measurements presented here, the set-up of the jet has minimal influence on the actual erosion happening, though this could be verified by repeating the tests done with the sand container using the different jet set-ups, to make sure this theory holds in practice. Since the current research might not be all-inclusive, more data and research would be needed to verify this claim.

The angle of the jet was hypothesized to influence the entrainment during water penetration in Chapter 3.3. Due to time constraints, the angle of the jet was never changed and was 40 degrees for all the tests. This might be of influence on the jet still and should be tested using the same or a similar setup. That way the data of these tests can be compared to each other to determine the influence of the incoming angle.

To compare the erosion of the different jet configurations more accurately the erosion test should be done for all four configurations. To verify if the erosion is actually constant for all the set-ups as claimed. Comparing the erosion from the tests with sand can give a more accurate comparison than comparing the velocity of the jets at increasing water depths.

The interpretation of the water percentage through the rods with conductivity sensors also remains uncertain. Further research in this area is needed. Archie's law with the factor used in this report is acceptable for larger water percentages but falls short at low water percentages. Since the conductivity sensors are more often used in sand where the conductivity is influenced differently than in air, this is due to the sand still leaving some room for the water and the air that can disrupt the measurement with thin layers of air covering the electrodes.

A

Small scale tests

(a) Inclined sand set-up (b) Jetting in water (c) Water tank used

(d) Break up length of a jet

Figure A.1: Pictures of the small scale tests

Some small-scale tests were done to become familiar with the subject matter before the set-up was designed.

A.1. Inclined sand erosion

The first quick set-up consisted of a tub filled with water with a wooden board in it, which has a 90-degree angle, as shown in Figure A.1a. The sand was loaded onto this board after which it was jetted away with a fire hose at a constant distance. This was done multiple times with different submerged levels of fine sand resulting in slightly different set-ups. This set-up was done to get acquainted with the physical aspects of the subject.

A.2. Water depth penetration of the jet

The second test consisted of a perspex box filled with water with sand at the bottom, as shown in Figure A.1c and Figure A.1b. This was done to check the penetration depth of the jet with different heights, angles, and different levels of turbulence. By changing the height, angle, and nozzle the turbulence and travel distance could be influenced. What was noticeable was the depth of influence of the jet matched the visual depth of the bubbles. When the bubbles didn't reach the bottom of the water tank the sand wouldn't erode. The angle caused the jet to penetrate to lesser depths, but since the tank was very small the influence of the wall made conclusions difficult. Making the jet turbulent resulted in a lesser penetration depth than very coherent jets. Salt was added to this tank halfway through the test with no visually noticeable influence on the penetration depth of the bubbles or the bubbles themselves. Since the visual measurements are limited in accuracy this might not be the actual case.

A.3. Pitot tube testing

A third test was done to check the measuring capabilities of a pitot tube in a turbulent jet in air. Expectations of air bubbles entering the pitot tube and influencing the measured pressure turned out to be false. The pitot tube gave a decent pressure reading as long as the pitot tube was positioned directly into the jet. When it was under a slight angle compared to the center of the jet the measurements quickly became unreliable. Measuring the pressure at multiple distances gave a very rough graph of the pressure decay over distance. Using a video camera the accompanying break-up length could visually be determined.

A.4. Break up length tests

A couple of tests were done concerning the breakup length. For this, the water was jetted horizontally and with a camera, the visual break-up length was determined. For a jet with 5 bar and a nozzle diameter of 30 mm, the visual break-up length occurred around 2 meters from the nozzle. For a fire hose with a pressure of 1,47 bar and a nozzle diameter of 6mm, the break-up seemed to occur at 0.9m from the nozzle.

Specifying the exact location of the break-up length is difficult due to the mist of water surrounding the center line of the jet. The visually determined break-up lengths did not seem to match the break-up lengths from the literature. Leading to the assumption that the break-up length is better determined visually than mathematically. Most likely due to the break-up length depending on a lot of factors that aren't part of the formulas. Such as the nozzle roughness and geometry and the inflow of water into the nozzle.

A.5. Key takeaways

From these small tests, some noticeable things happened which will require more in-depth research or should be taken into account during the actual final set-up. The jet was creating a burrow at the location of impact and subsequently filling that indentation with water. Which is to be expected when looking at the actual scenario from which this was derived. What was interesting was that it seemed like the jet was breaking up before it hit the break-up length found in the literature. After measuring beside a ruler it looked like the distance before the break length was reached was very short in comparison with what was expected. Though this should be re-evaluated with more accurate cameras. If the water jet didn't travel the entire distance through the air but covered the last part of the distance sliding over the diagonal wall seemed to have a relatively strong impact on the submerged sand. A jet sliding along the wall has very little aeration while covering the distance but is subject to the shear stress the wall exerts on the water. Besides this, the jet no longer has a break-up length since it isn't traveling through the air. When the water jet clings to the side the thickness of the jet is less than it can be in the air. This speeds up the process of velocity reduction in the center of the jet. The air cavity due to plunging is also likely to be less when the jet sticks to the wall since the air can only enter from one side. This is likely to reduce the number of bubbles created during the water line penetration.

B

Drawings of set-up components

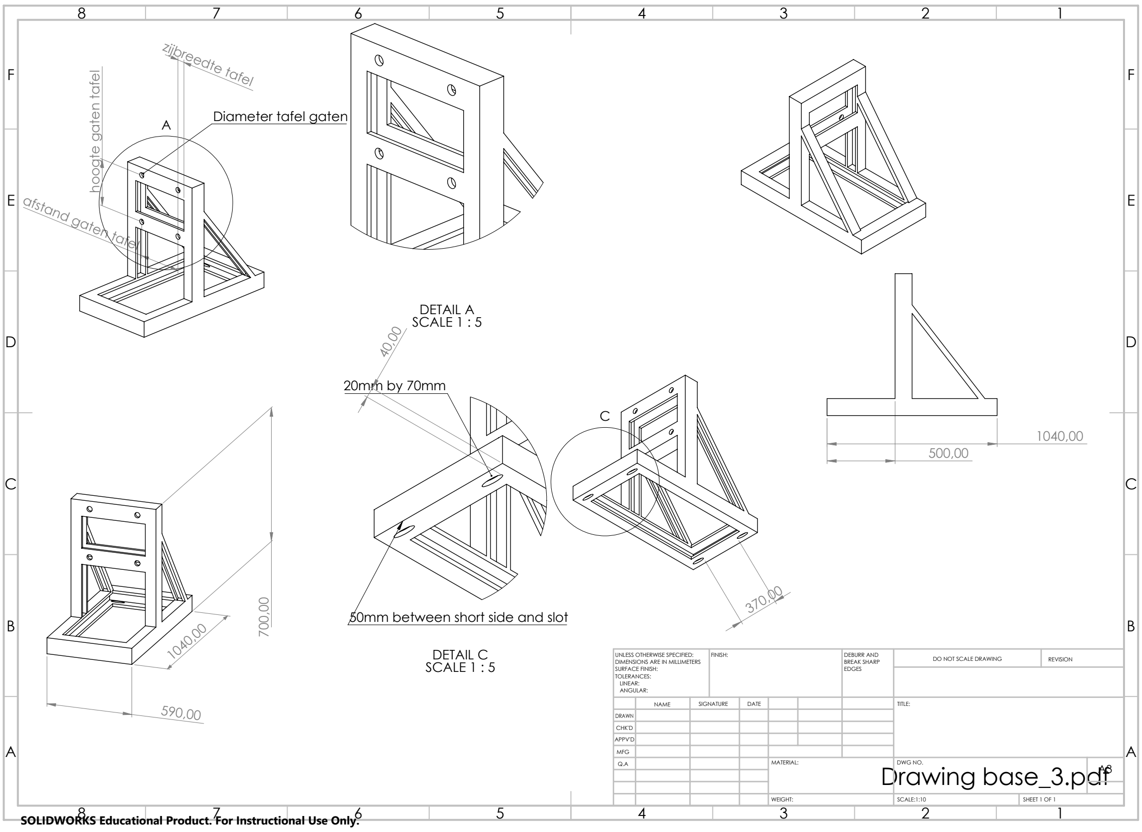

Figure B.1: Drawing of the base for the cross slide worktable

There is an x-y-table connected to the base shown in Figure B.1 to this x-y-table the frame was connected. The table made the horizontal and vertical movement of the frame fairly easy.

Using the plate from Figure B.2 the pipes leading to the nozzle could be set under a 40-degree angle, which was the angle of interest. The pipes were connected using nuts and bolts through the holes in the attachment.

The frame, as shown in Figure B.3, was used to connect the pitot tube and rods with conductivity sensors. The rods and pitot tube were set under a matching 40-degree angle with the nozzle forming an X in the middle of the square.

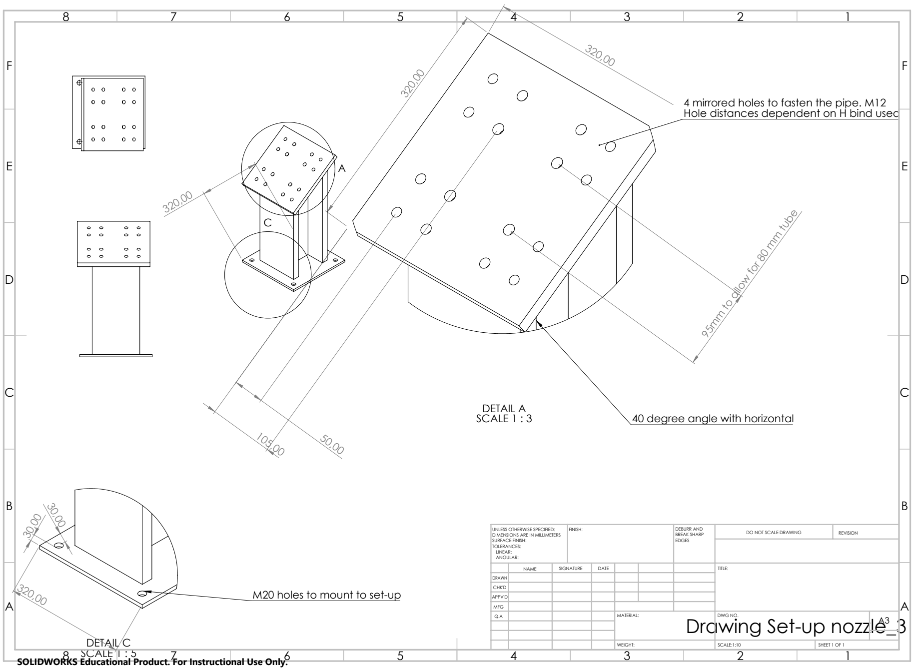

Figure B.2: Drawing of the attachment location for the jet

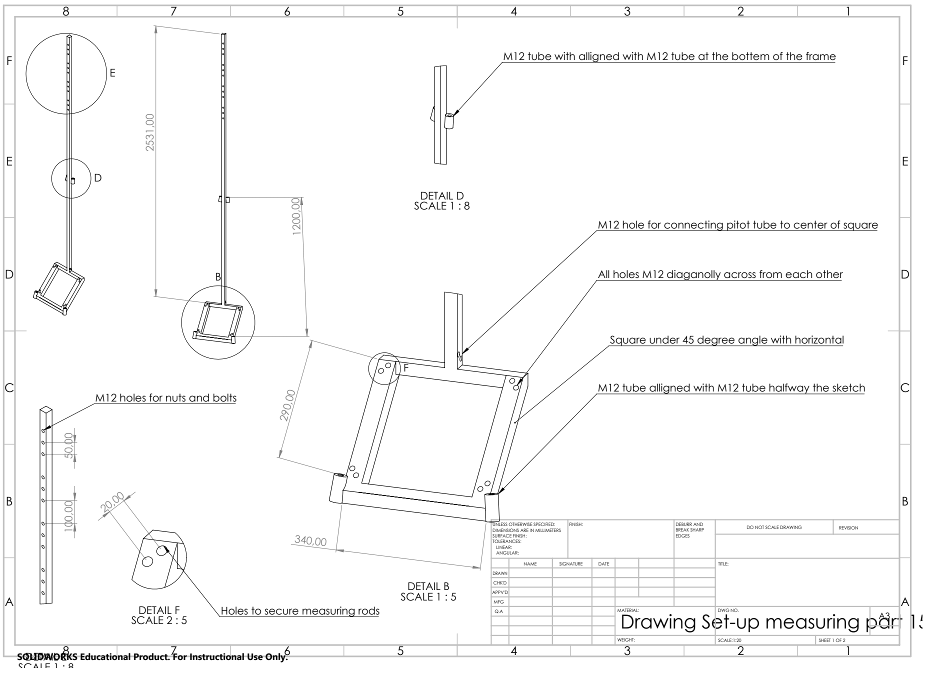

Figure B.3: Drawing of the measuring part of the set-up

C

Labview script

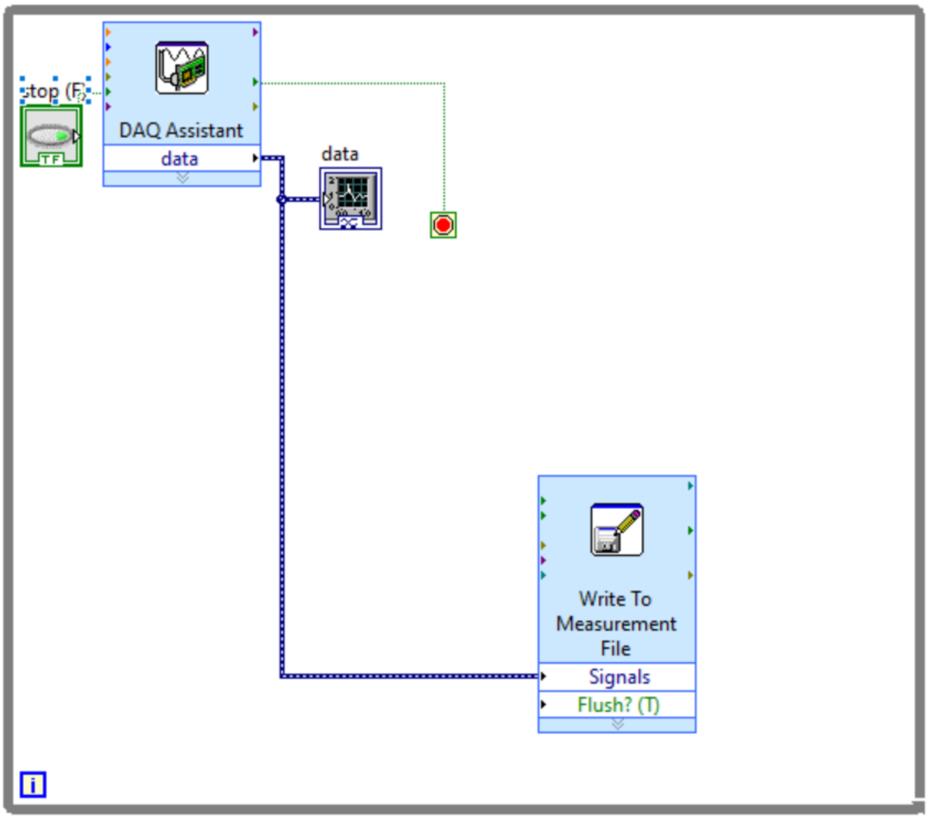

Figure C.1: Lab view script used

Shown in Figure C.1 is the script used to read the rods with conductivity sensors. the DAQ assistant collects data which the data shows on the screen when running. Using the Write To Measurement File the measurements are saved as an Excel file with all of the inputs side by side and the exact time of the measurement on the left. The data was measured with a sampling rate of 50 Hz.

D

Conductivity sensor boundary values

This appendix gives the raw data of the conductivity sensors. This data is represented in the graph in Figure D.1 showing the largest and smallest value of the conductivity sensors when slowly lifted out of the water. The measured voltage is given on the y-axis and the number of the measurement on the x-axis. Where the conductivity sensor measured with a sample rate of 50 measurements per second. This graph is only for point $Voltage\_9$, the other conductivity sensors gave similar graphs but with slightly different upper and lower values. This is why voltage percentages are used in the calculations instead of the absolute voltage values. Where the lowest value is taken as 0% and the largest value as 100%, which in this case corresponds to 8.6V and -3.43V

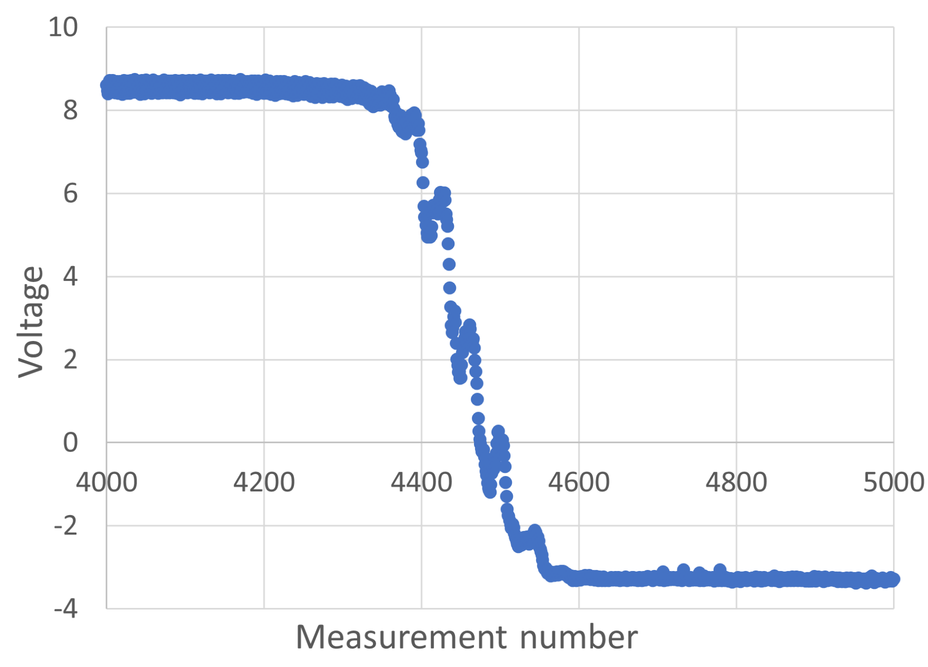

Figure D.1: Voltage_9 measurement points at transition from water to air

Figure D.2 shows the numbers which are used to create the graph in this appendix. These are some of the given voltage values at the during the test from water to air for measurement points from $Voltage\_1$ to $Voltage\_9$. The graph for the transitory segment from $Voltage\_9$ is given in the above Figure D.1.

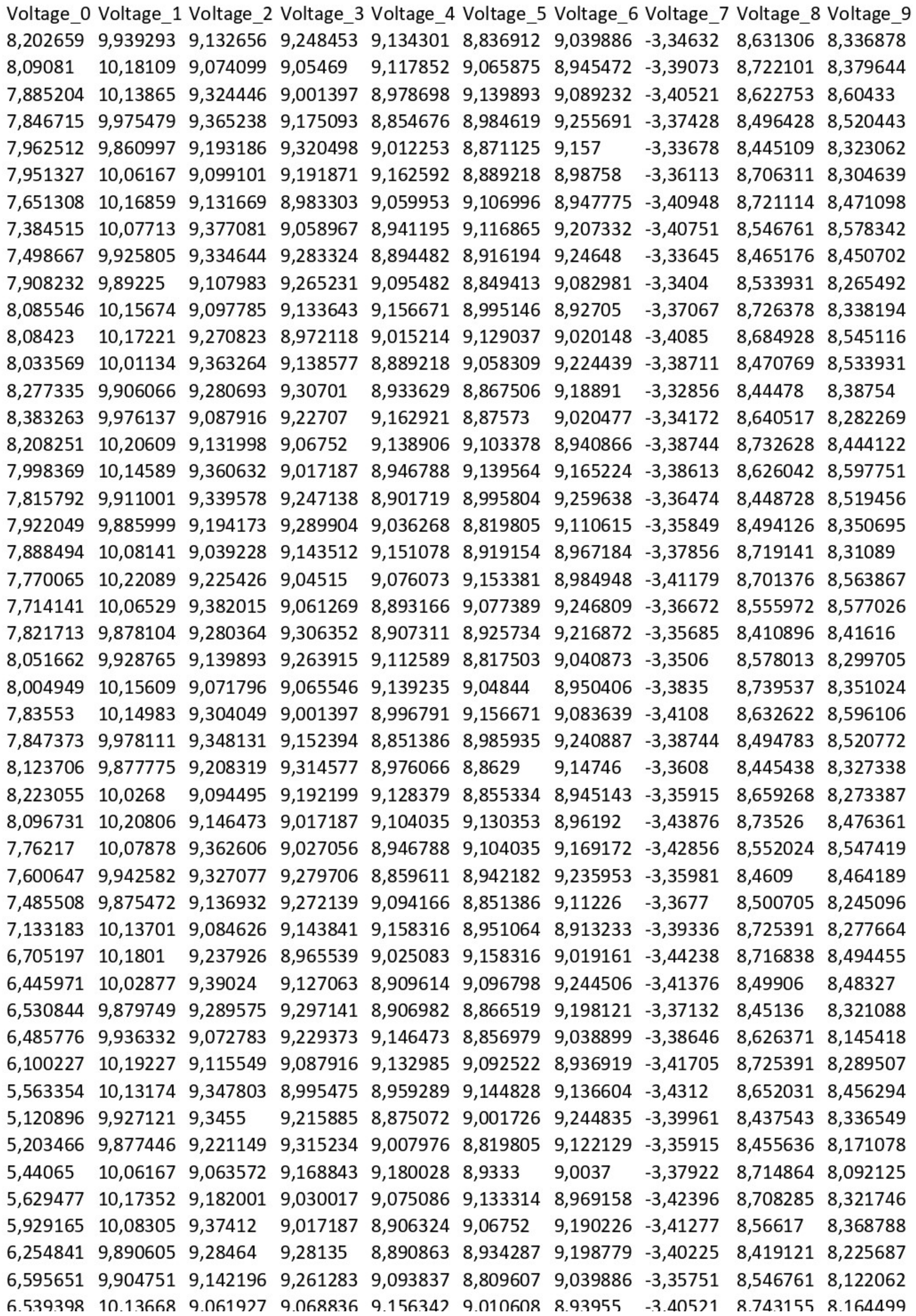

Voltage_0	Voltage_1	Voltage_2	Voltage_3	Voltage_4	Voltage_5	Voltage_6	Voltage_7	Voltage_8	Voltage_9
8,202659	9,939293	9,132656	9,248453	9,134301	8,836912	9,039886	-3,34632	8,631306	8,336878
8,09081	10,18109	9,074099	9,05469	9,117852	9,065875	8,945472	-3,39073	8,722101	8,379644
7,885204	10,13865	9,324446	9,001397	8,978698	9,139893	9,089232	-3,40521	8,622753	8,60433
7,846715	9,975479	9,365238	9,175093	8,854676	8,984619	9,255691	-3,37428	8,496428	8,520443
7,962512	9,860997	9,193186	9,320498	9,012253	8,871125	9,157	-3,33678	8,445109	8,323062
7,951327	10,06167	9,099101	9,191871	9,162592	8,889218	8,98758	-3,36113	8,706311	8,304639
7,651308	10,16859	9,131669	8,983303	9,059953	9,106996	8,947775	-3,40948	8,721114	8,471098
7,384515	10,07713	9,377081	9,058967	8,941195	9,116865	9,207332	-3,40751	8,546761	8,578342
7,498667	9,925805	9,334644	9,283324	8,894482	8,916194	9,24648	-3,33645	8,465176	8,450702
7,908232	9,89225	9,107983	9,265231	9,095482	8,849413	9,082981	-3,3404	8,533931	8,265492
8,085546	10,15674	9,097785	9,133643	9,156671	8,995146	8,92705	-3,37067	8,726378	8,338194
8,08423	10,17221	9,270823	8,972118	9,015214	9,129037	9,020148	-3,4085	8,684928	8,545116
8,033569	10,01134	9,363264	9,138577	8,889218	9,058309	9,224439	-3,38711	8,470769	8,533931
8,277335	9,906066	9,280693	9,30701	8,933629	8,867506	9,18891	-3,32856	8,44478	8,38754
8,383263	9,976137	9,087916	9,22707	9,162921	8,87573	9,020477	-3,34172	8,640517	8,282269
8,208251	10,20609	9,131998	9,06752	9,138906	9,103378	8,940866	-3,38744	8,732628	8,444122
7,998369	10,14589	9,360632	9,017187	8,946788	9,139564	9,165224	-3,38613	8,626042	8,597751
7,815792	9,911001	9,339578	9,247138	8,901719	8,995804	9,259638	-3,36474	8,448728	8,519456
7,922049	9,885999	9,194173	9,289904	9,036268	8,819805	9,110615	-3,35849	8,494126	8,350695
7,888494	10,08141	9,039228	9,143512	9,151078	8,919154	8,967184	-3,37856	8,719141	8,31089
7,770065	10,22089	9,225426	9,04515	9,076073	9,153381	8,984948	-3,41179	8,701376	8,563867
7,714141	10,06529	9,382015	9,061269	8,893166	9,077389	9,246809	-3,36672	8,555972	8,577026
7,821713	9,878104	9,280364	9,306352	8,907311	8,925734	9,216872	-3,35685	8,410896	8,41616
8,051662	9,928765	9,139893	9,263915	9,112589	8,817503	9,040873	-3,3506	8,578013	8,299705
8,004949	10,15609	9,071796	9,065546	9,139235	9,04844	8,950406	-3,3835	8,739537	8,351024
7,83553	10,14983	9,304049	9,001397	8,996791	9,156671	9,083639	-3,4108	8,632622	8,596106
7,847373	9,978111	9,348131	9,152394	8,851386	8,985935	9,240887	-3,38744	8,494783	8,520772
8,123706	9,877775	9,208319	9,314577	8,976066	8,8629	9,14746	-3,3608	8,445438	8,327338
8,223055	10,0268	9,094495	9,192199	9,128379	8,855334	8,945143	-3,35915	8,659268	8,273387
8,096731	10,20806	9,146473	9,017187	9,104035	9,130353	8,96192	-3,43876	8,73526	8,476361
7,76217	10,07878	9,362606	9,027056	8,946788	9,104035	9,169172	-3,42856	8,552024	8,547419
7,600647	9,942582	9,327077	9,279706	8,859611	8,942182	9,235953	-3,35981	8,4609	8,464189
7,485508	9,875472	9,136932	9,272139	9,094166	8,851386	9,11226	-3,3677	8,500705	8,245096
7,133183	10,13701	9,084626	9,143841	9,158316	8,951064	8,913233	-3,39336	8,725391	8,277664
6,705197	10,1801	9,237926	8,965539	9,025083	9,158316	9,019161	-3,44238	8,716838	8,494455
6,445971	10,02877	9,39024	9,127063	8,909614	9,096798	9,244506	-3,41376	8,49906	8,48327
6,530844	9,879749	9,289575	9,297141	8,906982	8,866519	9,198121	-3,37132	8,45136	8,321088
6,485776	9,936332	9,072783	9,229373	9,146473	8,856979	9,038899	-3,38646	8,626371	8,145418
6,100227	10,19227	9,115549	9,087916	9,132985	9,092522	8,936919	-3,41705	8,725391	8,289507
5,563354	10,13174	9,347803	8,995475	8,959289	9,144828	9,136604	-3,4312	8,652031	8,456294
5,120896	9,927121	9,3455	9,215885	8,875072	9,001726	9,244835	-3,39961	8,437543	8,336549
5,203466	9,877446	9,221149	9,315234	9,007976	8,819805	9,122129	-3,35915	8,455636	8,171078
5,44065	10,06167	9,063572	9,168843	9,180028	8,9333	9,0037	-3,37922	8,714864	8,092125
5,629477	10,17352	9,182001	9,030017	9,075086	9,133314	8,969158	-3,42396	8,708285	8,321746
5,929165	10,08305	9,37412	9,017187	8,906324	9,06752	9,190226	-3,41277	8,56617	8,368788
6,254841	9,890605	9,28464	9,28135	8,890863	8,934287	9,198779	-3,40225	8,419121	8,225687
6,595651	9,904751	9,142196	9,261283	9,093837	8,809607	9,039886	-3,35751	8,546761	8,122062
6,539398	10,13668	9,061927	9,068836	9,156342	9,010608	8,93955	-3,40521	8,743155	8,164499

Figure D.2: Raw data from conductivity sensors from water to air

E

Raw data

E.1. Regular tests

This section shows the data used to construct the density and water percentage over distance above and below water. The first column, 1 shows the date on which the experiments took place, the second column, 2 shows the test that day. Then it gives whether it was above or below water, 3. Then it gives the vertical distance below the water and then the distance in the jet traveling direction from the nozzle to the frame, 4 and 5. Then it says what set-up was used in this test, 6. The following numbers are the maximum and minimum values of that measurement point that day, 6 an 7 for V9 and 10 and 11 for V10. The subsequent number is the average voltage during the measurement, 9 for V9 and 12 for V10. The final two columns. 13 and 14 are the absolute and relative pressure of that measurement.

1	2	3	4	5	6	7	8	9	10	11	12	13	14
Date	Test	Above or below	Vertical water depth [m]	Distance nozzle-frame [m]	Set-up	v9 Vref water [v]	Vref air [v]	Vavg measure [v]	v10 Vref water [v]	Vref air [v]	Vavg measure [v]	Average pressure absolute [bar]	Average pressure relative [bar]
221116													
	test 2	Above	-	2,25		9,2508	-3,5585	-0,6853	9,6560	-3,4115	3,1990	1,93	0,89
221117													
	test 1	Above	-	2,09		10,1044	-3,0062	-0,0783	10,2117	-2,8302	0,5328	1,89	0,87
	test 2	Above	-	2,09		10,1044	-3,0062	-2,7494	10,2117	-2,8302	-2,5424	1,88	0,91
	test 3	Above	-	2,70		10,1044	-3,0062	-1,8217	10,2117	-2,8302	-0,4888	1,31	0,39
221118													
	test 1	Above	-	2,94		10,0784	-3,5980	-2,5656	9,8824	-3,4013	-0,6671	1,70	0,78
	test 2	Above	-	3,12		10,0784	-3,5980	-2,3301	9,8824	-3,4013	-0,5521	1,57	0,67
	test 3	Above	-	3,22		10,0784	-3,5980	-2,2726	9,8824	-3,4013	-1,3464	1,26	0,38
221121													
	test 1	Below	0,15	3,89		10,1854	-3,6148	5,8155	10,1933	-3,3851	4,3529	0,94	0,08
	test 3	Below	0,16	3,40		10,1854	-3,6148	2,6594	10,1933	-3,3851	0,4851	1,58	0,66
	test 5	Below	0,42	3,84		10,1854	-3,6148	6,6225	10,1933	-3,3851	6,0117	1,37	0,43
	test 6	Below	0,45	3,98		10,1854	-3,6148	4,8364	10,1933	-3,3851	3,9750	1,40	0,51
221123													
	test 1	Above		3,54		10,7716	-3,1651	-1,8096	10,7716	-3,0131	-2,0426	1,66	0,80
	test 2	Below	0,09	3,54		10,7716	-3,1651	0,4260	10,7716	-3,0131	0,7268	1,66	0,80
	test 3	Below	0,14	3,69		10,7716	-3,1651	3,1551	10,7716	-3,0131	1,7606	1,63	0,75
	test 4	Below	0,24	3,66		10,7716	-3,1651	4,9275	10,7716	-3,0131	4,8164	1,75	0,85
	test 5	Below	0,37	3,66		10,7716	-3,1651	5,7118	10,7716	-3,0131	5,3268	1,48	0,58
221124													
	test 2	Below	0,46	3,38		8,9182	-3,2914	8,5602	8,7823	-3,1480	4,2254	1,01	0,11
	test 3	Below	0,375	3,02		8,9182	-3,2914	3,2744	8,7823	-3,1480	2,9552	1,58	0,67
	test 5	Below	0,29	2,71		8,9182	-3,2914	-1,3246	8,7823	-3,1480	-1,5707	1,53	0,64
221128													
	test 2	Above		2,35		10,7716	-3,5289	-0,6734	10,7716	-3,3937	0,7174	2,05	1,15
	test 4	Above		1,91		10,7716	-3,5289	0,1234	10,7716	-3,3937	0,3407	2,26	1,31
221129													

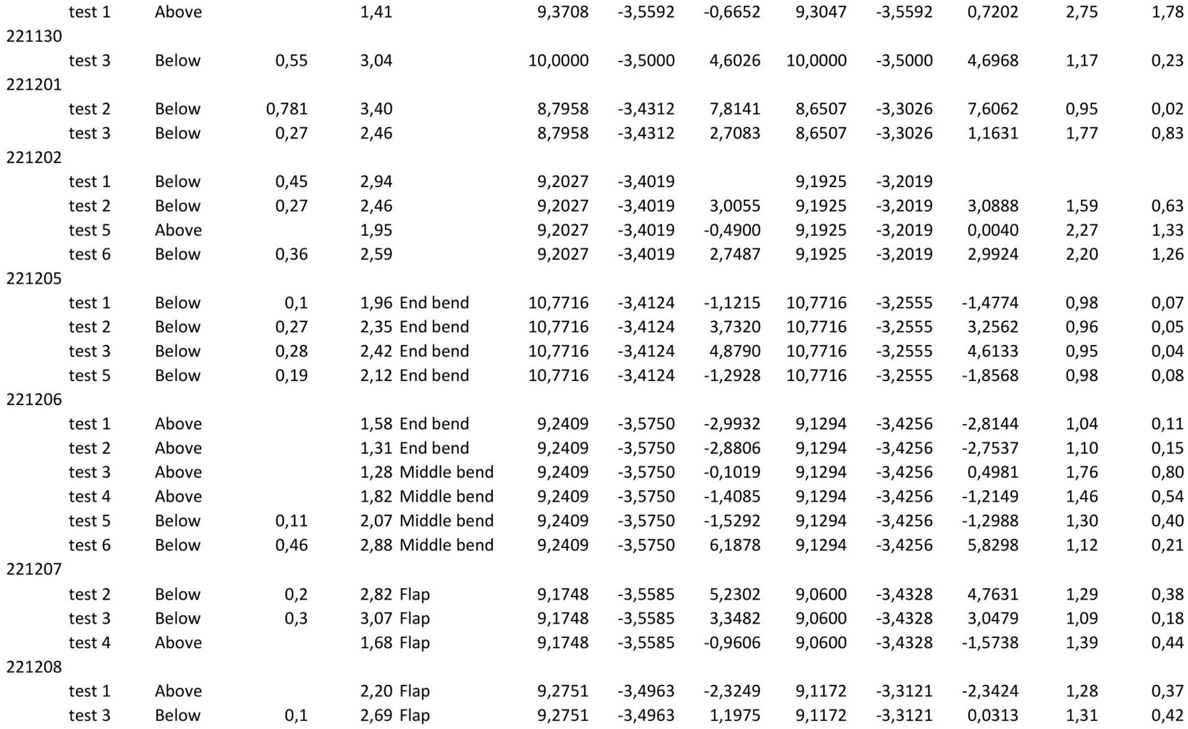

	test 1	Above		1,41		9,3708	-3,5592	-0,6652	9,3047	-3,5592	0,7202	2,75	1,78
221130													
	test 3	Below	0,55	3,04		10,0000	-3,5000	4,6026	10,0000	-3,5000	4,6968	1,17	0,23
221201													
	test 2	Below	0,781	3,40		8,7958	-3,4312	7,8141	8,6507	-3,3026	7,6062	0,95	0,02
	test 3	Below	0,27	2,46		8,7958	-3,4312	2,7083	8,6507	-3,3026	1,1631	1,77	0,83
221202													
	test 1	Below	0,45	2,94		9,2027	-3,4019		9,1925	-3,2019			
	test 2	Below	0,27	2,46		9,2027	-3,4019	3,0055	9,1925	-3,2019	3,0888	1,59	0,63
	test 5	Above		1,95		9,2027	-3,4019	-0,4900	9,1925	-3,2019	0,0040	2,27	1,33
	test 6	Below	0,36	2,59		9,2027	-3,4019	2,7487	9,1925	-3,2019	2,9924	2,20	1,26
221205													
	test 1	Below	0,1	1,96	End bend	10,7716	-3,4124	-1,1215	10,7716	-3,2555	-1,4774	0,98	0,07
	test 2	Below	0,27	2,35	End bend	10,7716	-3,4124	3,7320	10,7716	-3,2555	3,2562	0,96	0,05
	test 3	Below	0,28	2,42	End bend	10,7716	-3,4124	4,8790	10,7716	-3,2555	4,6133	0,95	0,04
	test 5	Below	0,19	2,12	End bend	10,7716	-3,4124	-1,2928	10,7716	-3,2555	-1,8568	0,98	0,08
221206													
	test 1	Above		1,58	End bend	9,2409	-3,5750	-2,9932	9,1294	-3,4256	-2,8144	1,04	0,11
	test 2	Above		1,31	End bend	9,2409	-3,5750	-2,8806	9,1294	-3,4256	-2,7537	1,10	0,15
	test 3	Above		1,28	Middle bend	9,2409	-3,5750	-0,1019	9,1294	-3,4256	0,4981	1,76	0,80
	test 4	Above		1,82	Middle bend	9,2409	-3,5750	-1,4085	9,1294	-3,4256	-1,2149	1,46	0,54
	test 5	Below	0,11	2,07	Middle bend	9,2409	-3,5750	-1,5292	9,1294	-3,4256	-1,2988	1,30	0,40
	test 6	Below	0,46	2,88	Middle bend	9,2409	-3,5750	6,1878	9,1294	-3,4256	5,8298	1,12	0,21
221207													
	test 2	Below	0,2	2,82	Flap	9,1748	-3,5585	5,2302	9,0600	-3,4328	4,7631	1,29	0,38
	test 3	Below	0,3	3,07	Flap	9,1748	-3,5585	3,3482	9,0600	-3,4328	3,0479	1,09	0,18
	test 4	Above		1,68	Flap	9,1748	-3,5585	-0,9606	9,0600	-3,4328	-1,5738	1,39	0,44
221208													
	test 1	Above		2,20	Flap	9,2751	-3,4963	-2,3249	9,1172	-3,3121	-2,3424	1,28	0,37
	test 3	Below	0,1	2,69	Flap	9,2751	-3,4963	1,1975	9,1172	-3,3121	0,0313	1,31	0,42

Figure E.1: Data normal tests

E.2. Sand tests

These numbers give again the date and number of the test that day. Followed by the weight before and after the jetting, succeeded by the time the pump was on. Next, it gives the water depth of the container followed by the depth of the frame during the subsequent test. Followed again by the maximum, minimum, and average voltage of that measurement.

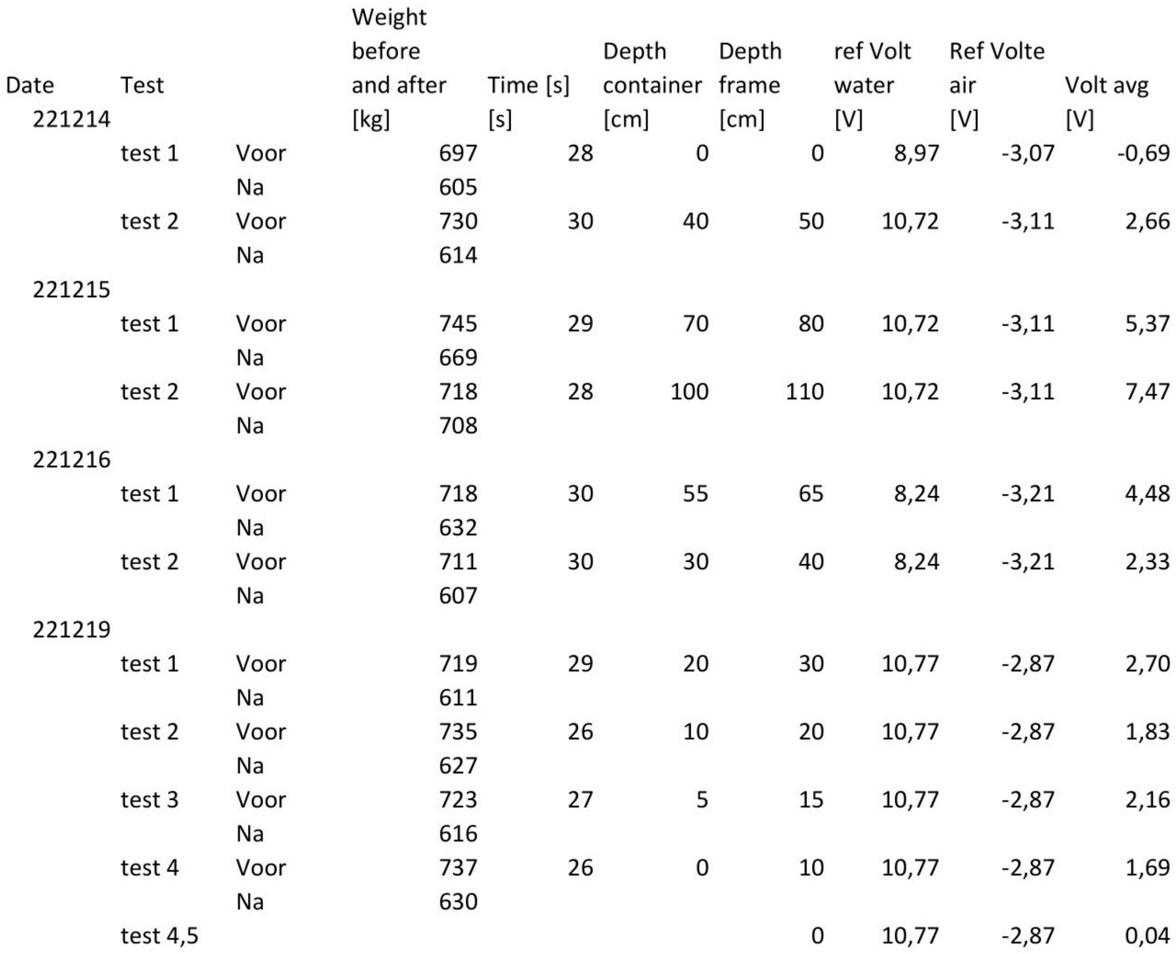

Date	Test		Weight before and after [kg]	Time [s] [s]	Depth container [cm]	Depth frame [cm]	ref Volt water [V]	Ref Volte air [V]	Volt avg [V]
221214									
	test 1	Voor	697	28	0	0	8,97	-3,07	-0,69
		Na	605						
	test 2	Voor	730	30	40	50	10,72	-3,11	2,66
		Na	614						
221215									
	test 1	Voor	745	29	70	80	10,72	-3,11	5,37
		Na	669						
	test 2	Voor	718	28	100	110	10,72	-3,11	7,47
		Na	708						
221216									
	test 1	Voor	718	30	55	65	8,24	-3,21	4,48
		Na	632						
	test 2	Voor	711	30	30	40	8,24	-3,21	2,33
		Na	607						
221219									
	test 1	Voor	719	29	20	30	10,77	-2,87	2,70
		Na	611						
	test 2	Voor	735	26	10	20	10,77	-2,87	1,83
		Na	627						
	test 3	Voor	723	27	5	15	10,77	-2,87	2,16
		Na	616						
	test 4	Voor	737	26	0	10	10,77	-2,87	1,69
		Na	630						
	test 4,5					0	10,77	-2,87	0,04

Figure E.2: Data sand tests

E.3. Profile tests

These data sets were used to create the profiles of the jets. First giving the set-up, vertical water depth, and distance from the nozzle to the measurement frame. Then the vertical location of the frame in mm as a distance from the jet center. Then it gives the pressures and average voltages corresponding to this location. On the bottom are the maximum and minimum voltages of these measurement points.

Set up	Corner	Location [mm]	P_abs [bar]	P_rel [bar]	Voltage_1 [V]	Voltage_2 [V]	Voltage_9 [V]	Voltage_10 [V]
water depth [m]	0,185	-20	0,975	0,069	1,187441	3,137251	1,035779	0,2035698
diagonal distance [m]	2,12	0	0,974	0,069	0,15776	1,899623	0,008688	-0,743661
		20	0,972	0,068	-0,81355	0,457526	-1,25441	-1,707126
		40	0,962	0,058	-1,38713	-0,64654	-1,88812	-2,106173
		60	0,961	0,056	-1,98532	-1,6545	-2,47861	-2,46031
		80	0,953	0,048	-2,2131	-2,01604	-2,664	-2,602658
		100	0,951	0,044	-2,42376	-2,3149	-2,85114	-2,711979
		120	0,947	0,038	-2,49012	-2,4255	-2,92617	-2,7828
		140	0,949	0,038	-2,53254	-2,4761	-2,96091	-2,807641
Max voltage [V]					10,77159	8,899416	10,07845	9,88238
Min Voltage [V]					-3,4335	-3,30224	-3,59798	-3,401259

Set up	Turb cor	Frame ve	P_abs	P_rel	Voltage_1	Voltage_2	Voltage_9	Voltage_10
water depth [m]	0,3	-120	0,902	0,000	9,40636	9,017384	8,026996	6,6923537
diagonal distance [m]	2,479	-100	0,907	0,005	8,403175	8,306764	7,248953	5,4701254
		-80	0,938	0,035	5,951856	6,670426	5,35738	4,0070292
		-60	0,982	0,079	4,50876	5,743406	4,370044	3,3078522
		-40	1,066	0,159	3,186652	4,865135	3,329804	2,7111869
		-20	1,191	0,281	2,272059	4,450288	2,630739	2,0247093
		0	1,223	0,315	1,553627	3,900041	1,786046	1,0915082
		20	1,134	0,230	0,890735	3,039519	0,945196	0,2022606
		40	1,035	0,133	0,757492	2,213111	0,430475	0,0284707
		60	0,973	0,074	1,078958	1,818361	0,43627	0,3387462
		80	0,937	0,037	1,881917	1,781945	0,657822	0,9349694
					10,77159	8,899416	10,07845	9,88238
Max voltage [V]					-3,4335	-3,30224	-3,59798	-3,401259
Min Voltage [V]								

Set up	Flap	Frame ve	P_abs	P_rel	Voltage_1	Voltage_2	Voltage_9	Voltage_10
water depth [m]	0	-20	1,203	0,299	-0,67296	-0,74316	-1,68979	-1,445033
diagonal distance [m]	2,119	-10	1,157	0,253	-1,93945	-1,08041	-2,28188	-2,547723
		0	1,204	0,301	-1,51745	-0,60472	-1,95802	-2,211818
		10	1,097	0,193	-2,17612	-1,44753	-2,54199	-2,746082
		20	1,037	0,132	-2,4566	-1,86432	-2,82471	-2,906013
		30	0,994	0,089	-2,63178	-2,25149	-3,00904	-3,017811
		40	0,962	0,057	-2,78564	-2,57987	-3,17882	-3,093133
Max voltage [V]					10,77159	8,899416	10,07845	9,88238
Min Voltage [V]					-3,4335	-3,30224	-3,59798	-3,401259

Set up	Flap	Frame ve	P_abs	P_rel	Voltage_1	Voltage_2	Voltage_9	Voltage_10
water depth [m]	0,1	-40	0,943	0,051	4,814746	6,345646	4,865339	3,6815995
diagonal distance [m]	2,668	-30	0,981	0,089	3,840041	5,545464	4,095147	3,0945289
		-20	1,063	0,167	2,769761	4,568327	3,167681	2,4969873
		-10	1,206	0,310	2,058711	4,012281	2,459783	1,4734165
		0	1,235	0,340	1,161063	3,379016	1,313791	0,19278
		10	1,164	0,273	0,440002	2,766295	0,517231	-0,571719
		20	1,058	0,171	-0,19586	1,750656	-0,47618	-1,149921
		30	1,005	0,120	-0,51595	0,991776	-1,00454	-1,427876
		40	0,964	0,079	-0,62935	0,275015	-1,39221	-1,635437
		50	0,945	0,061	-0,77302	-0,3412	-1,7235	-1,824581

		60	0,932	0,048	-0,72941	-0,7326	-1,9327	-1,921696
Max voltage [V]					10,77159	8,899416	10,07845	9,88238
Min Voltage [V]					-3,4335	-3,30224	-3,59798	-3,401259
Set up	Flap	Frame ve	P_abs	P_rel	Voltage_1	Voltage_2	Voltage_9	Voltage_10
water depth [m]	0	-50	1,009	0,120	-2,02565	-2,24358	-2,79517	-2,208215
diagonal distance [m]	2,343	-40	1,080	0,189	-1,48282	-1,71801	-2,43927	-1,831331
		-30	1,141	0,249	-1,06617	-1,26202	-2,08046	-1,534999
		-20	1,195	0,301	-1,01991	-0,9423	-1,93277	-1,476394
		-10	1,233	0,338	-0,8514	-0,55026	-1,68003	-1,574687
		0	1,240	0,344	-1,24634	-0,41863	-1,75241	-1,919904
		10	1,195	0,298	-1,72101	-0,73118	-2,09982	-2,382976
		20	1,143	0,246	-1,96469	-1,08041	-2,34225	-2,60049
		30	1,063	0,166	-2,37887	-1,68143	-2,77212	-2,906257
		40	1,015	0,118	-2,60138	-2,13747	-2,97913	-3,004867
		50	0,981	0,083	-2,75316	-2,41704	-3,11519	-3,081139
		60	0,957	0,059	-2,86654	-2,65881	-3,19823	-3,092884
		70	0,944	0,045	-2,92861	-2,80323	-3,2347	-3,117881
Max voltage [V]					10,77159	8,899416	10,07845	9,88238
Min Voltage [V]					-3,4335	-3,30224	-3,59798	-3,401259
Set up	Straight	Frame ve	P_abs	P_rel	Voltage_1	Voltage_2	Voltage_9	Voltage_10
water depth [m]	0	-50	1,077	0,085	-0,9975	-2,06582	-2,59296	-1,563453
diagonal distance [m]	1,409	-40	1,168	0,176	1,394308	-1,166	-1,59559	0,0416043
		-30	1,306	0,314	3,010699	0,103038	0,007247	1,5479456
		-20	1,570	0,579	3,970217	2,545078	2,5777	3,8519704
		-10	1,967	0,976	3,207437	4,864667	3,949182	4,2014564
		0	2,354	1,362	1,498814	6,109058	3,551449	2,9195948
		10	2,386	1,395	-0,0556	6,384162	1,356046	1,0581082
		20	2,155	1,163	-1,02139	5,299094	-0,4969	-0,695483
Max voltage [V]					10,77159	9,942582	9,318195	9,200424
Min Voltage [V]					-3,39534	-3,25915	-3,58482	-3,420339
Set up	Straight	Frame ve	P_abs	P_rel	Voltage_1	Voltage_2	Voltage_9	Voltage_10
water depth [m]	0	-50	1,105	0,179	-0,32831	-1,61541	-2,04483	-0,705357
diagonal distance [m]	1,91	-40	1,247	0,316	1,39435	-0,38548	-0,71707	1,1659803
		-30	1,447	0,510	2,278459	1,319565	0,887708	2,5045874
		-20	1,748	0,802	2,106673	3,071042	2,066904	3,110417
		-10	2,098	1,148	1,063831	4,670272	2,227082	2,5255831
		0	2,193	1,248	-0,01383	4,974629	0,940828	0,9500036
		10	2,009	1,070	-1,02212	4,425741	-0,54659	-0,377838
		20	1,664	0,728	-1,61082	2,762486	-1,72584	-1,527352
		30	1,371	0,437	-1,98893	0,969564	-2,46374	-2,427133
		40	1,215	0,281	-2,2733	-0,55096	-2,86056	-2,786806
		50	1,104	0,170	-2,42526	-1,51185	-3,07755	-2,999347
		60	1,057	0,122	-2,50992	-2,20236	-3,15186	-3,049118
		70	1,020	0,084	-2,63642	-2,57893	-3,2218	-3,114066
Max voltage [V]			Max voltage		10,59625	9,650785	9,015214	8,876388
Min Voltage [V]			Min Voltage		-3,39731	-3,27198	-3,58219	-3,430866
Set up	Straight	Frame ve	P_abs	P_rel	Voltage_1	Voltage_2	Voltage_9	Voltage_10
water depth [m]	0	-40	1,061	0,165	-0,33007	-1,50339	-1,97308	-0,946787
diagonal distance [m]	2,353	-30	1,187	0,287	1,208166	-0,43528	-0,74006	0,3777757
		-20	1,451	0,544	1,872562	1,384939	0,744007	1,8546615

		-10	1,653	0,742	1,425881	2,620327	1,327281	2,3257946
		0	1,920	1,007	0,420881	3,79763	0,995682	1,3699142
		10	1,942	1,032	-0,52422	3,735563	-0,04742	0,4059954
		20	1,821	0,914	-1,11372	3,126804	-1,1105	-0,515652
		30	1,681	0,775	-1,40145	2,585007	-1,45688	-1,13906
		40	1,409	0,505	-1,8253	1,013972	-2,26258	-2,061867
		50	1,316	0,411	-1,97174	0,485951	-2,4144	-2,347641
		60	1,098	0,194	-2,39663	-1,36221	-2,9688	-2,857068
		70	1,022	0,118	-2,55373	-2,1407	-3,10602	-3,02212
ax voltage [V]					10,59625	9,650785	9,015214	8,876388
in Voltage [V]					-3,39731	-3,27198	-3,58219	-3,430866
et up	Straight	Frame ve	P_abs	P_rel	Voltage_1	Voltage_2	Voltage_9	Voltage_10
ater depth [m]	0,37	-80	1,034	0,042	7,529779	7,696939	6,644665	5,3592788
iagonal distance [m]	3,669	-70	1,071	0,079	5,767269	6,330868	5,334464	4,5679586
		-60	1,096	0,104	5,428278	6,136812	5,145229	4,4062734
		-50	1,169	0,177	4,869937	5,717642	4,924416	4,4221525
		-40	1,221	0,229	4,43938	5,495482	4,670954	4,2706583
		-30	1,212	0,220	3,840414	5,042092	4,123581	3,800138
		-20	1,329	0,338	3,843473	5,146202	4,1316	3,8975766
		-10	1,347	0,355	3,488639	4,983203	3,853528	3,6492321
		0	1,410	0,419	3,256858	5,021362	3,676742	3,5659958
		10	1,385	0,393	3,215666	5,027007	3,625235	3,4029305
		20	1,237	0,245	3,39394	5,105604	3,728427	3,5165909
		30	1,243	0,251	3,212518	5,013975	3,64749	3,3916539
		40	1,165	0,173	3,03638	4,926127	3,538422	3,5040287
		50	1,119	0,127	2,962625	5,013608	3,595854	3,6132815
		60	1,086	0,094	2,830805	4,974011	3,554193	3,7829649
		70	1,061	0,069	2,908672	5,153	3,725255	4,0409454
		80	1,046	0,055	2,996813	5,347463	3,915365	4,2093321
		90	1,038	0,046	3,162952	5,41214	4,060759	4,3055927
ax voltage [V]					10,77159	8,899416	10,07845	9,88238
in Voltage [V]					-3,4335	-3,30224	-3,59798	-3,401259
et up	Straight	Frame ve	P_abs	P_rel	Voltage_1	Voltage_2	Voltage_9	Voltage_10
ater depth [m]	0,46	60	1,027	0,116	3,917373	5,541122	4,226111	4,2807701
iagonal distance [m]	3,375	50	1,043	0,132	3,578836	5,387714	3,925458	4,084523
		40	1,056	0,145	3,334171	5,345848	3,853195	4,1117675
		30	1,064	0,153	3,250193	5,178819	3,691432	3,8912185
		20	1,091	0,180	2,885143	5,080463	3,499725	3,710295
		10	1,065	0,154	2,724306	5,153635	3,544561	3,8704293
		0	1,049	0,138	2,851036	5,395718	3,730131	4,0979179
		-10	1,038	0,127	2,919386	5,437106	3,976728	4,1086699
		-20	0,993	0,082	3,353659	5,817586	4,362925	4,6312688
		-30	0,957	0,046	3,803088	6,34558	5,006875	5,0169964
		-40	0,947	0,036	3,940485	6,497566	5,165155	5,173706
		-50	0,937	0,026	4,320948	6,784645	5,595656	5,4590022
ax voltage [V]					10,24293	9,340894	8,65236	8,543142
in Voltage [V]					-2,82952	-2,64826	-3,07295	-2,905836
et up	Straight	Frame ve	P_abs	P_rel	Voltage_1	Voltage_2	Voltage_9	Voltage_10
ater depth [m]	0,29	-50	1,264	0,361	3,407464	2,9683	2,836597	2,6986325
iagonal distance [m]	2,712	-40	1,440	0,530	2,703316	3,503925	3,011661	2,8377985

		-30	1,778	0,864	1,319894	4,165043	2,341365	2,1963459
		-20	1,871	0,967	0,205491	4,30619	1,124897	0,7586281
		-10	1,779	0,878	0,063143	3,984899	0,830973	0,364578
		0	1,723	0,826	-0,30581	3,714786	0,391736	-0,113807
		10	1,302	0,415	-1,50125	1,164688	-2,00747	-2,029377
		20	1,161	0,276	-1,79613	-0,05675	-2,42578	-2,466882
		30	1,063	0,178	-2,02437	-1,10351	-2,72831	-2,706639
		40	0,982	0,097	-1,96449	-1,8759	-2,90636	-2,85852
		50	0,938	0,053	-1,80163	-2,28517	-2,97607	-2,90851
		60	0,915	0,028	-0,72462	-2,47551	-2,83288	-2,796068
Max voltage [V]					10,77159	8,899416	10,07845	9,88238
Min Voltage [V]					-3,4335	-3,30224	-3,59798	-3,401259
Set up	Straight	Frame ve	P_abs	P_rel	Voltage_1	Voltage_2	Voltage_9	Voltage_10
water depth [m]	0,27	-30	1,292	0,333	3,184225	4,781709	3,633086	3,7285887
diagonal distance [m]	2,464	-20	1,382	0,419	2,944621	4,729346	3,416977	3,551125
		-10	1,412	0,455	2,489032	4,880797	3,139322	3,1724695
		0	1,420	0,462	2,488568	4,820629	3,014995	2,9899583
		10	1,374	0,415	2,311264	4,916742	2,994659	2,9993539
		20	1,285	0,325	2,257016	4,581853	2,79441	2,8991672
		30	1,216	0,259	2,50059	4,559545	2,925188	3,1719804
		40	1,192	0,232	2,410386	4,476543	2,826188	3,092097
		50	1,117	0,158	2,85145	4,612094	3,211593	3,4202096
		60	1,068	0,109	3,518675	4,960938	3,852682	3,930972
Max voltage [V]					10,77159	8,899416	10,07845	9,88238
Min Voltage [V]					-3,4335	-3,30224	-3,59798	-3,401259
Set up	Straight	Frame ve	P_abs	P_rel	Voltage_1	Voltage_2	Voltage_9	Voltage_10
water depth [m]	0,375	50	1,065	0,140	3,504024	3,973642	3,125007	3,0064684
diagonal distance [m]	3,024	40	1,084	0,159	3,300294	4,037853	3,119192	2,9594661
		30	1,165	0,240	2,966112	3,829275	3,010158	2,7423373
		20	1,278	0,353	2,066341	3,975919	2,741704	2,3697211
		10	1,384	0,459	0,441385	3,968083	1,181419	0,7837832
		0	1,090	0,165	1,039194	2,756604	0,74822	1,6056592
		-10	1,010	0,085	2,46036	3,17322	1,954291	2,8184046
		-20	0,981	0,056	3,150615	3,574017	2,595184	3,2472619
		-30	0,941	0,016	6,203318	5,991401	5,361051	5,2075487
Max voltage [V]					10,77159	8,899416	10,07845	9,88238
Min Voltage [V]					-3,4335	-3,30224	-3,59798	-3,401259

Figure E.3: Data profile tests

F

Peristaltic hose pump data

A peristaltic hose pump was used to verify the air-water percentages. This pump pumps up a constant volume at every rotation. When a verification measurement is taken from stagnant water this can be compared to measurements of water with air mixed in. From this, the water and air percentages in the mixture can theoretically be determined.

The pump was used during the jetting tests to determine the water percentages at the jet location to verify the water percentages given by the conductivity sensors. This was done by zip-tying the tube to the frame with the opening of the hose next to the pitot tube. There was some uncertainty about whether the peristaltic pump prioritized water over air when taking in its constant volume. To determine this some tests were done, first in stagnant water, then in an air-water mixture from the cylinder tests.

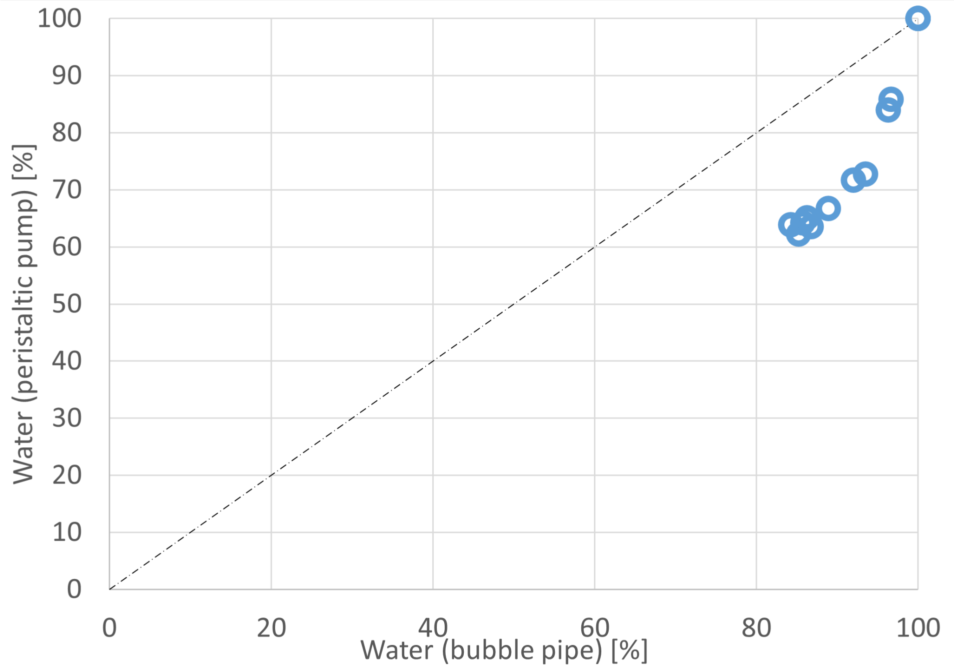

Figure F.1: Water percentage peristaltic pump and water percentage from cylinder

Figure F.1 shows the water percentage according to the peristaltic pump plotted against the water percentage according to the volume increase from the bubble pipe, with the raw data shown in Figure F.2. This graph shows that the peristaltic pump underestimated the water percentage for nearly all verified points. This can be due to the tube more easily sucking up air than water. The peristaltic pump was positioned vertically in the bubble pipe test as can be seen in the figure in Appendix K. This might have prioritized the rising bubble over the water. The peristaltic pump in the actual set-up next to the pitot tube might also have prioritized air, since the water passed the hose inlet with a velocity of $26,8 m/s$ which might have made it difficult for this pump to take in the water.

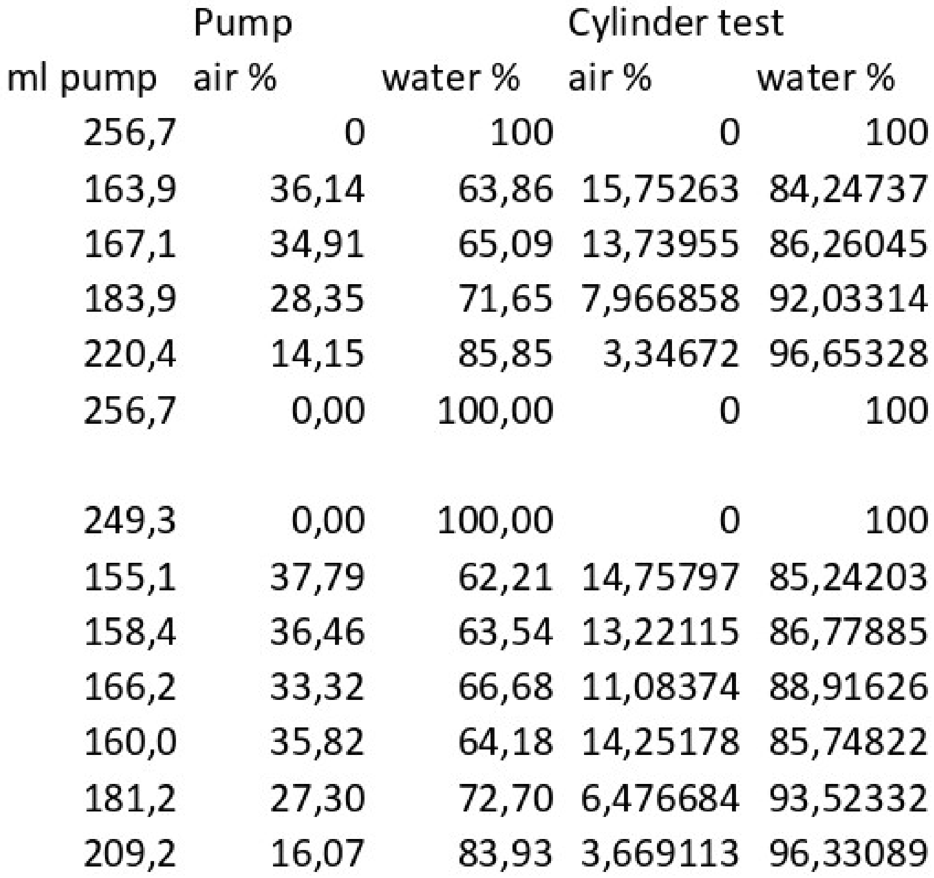

	Pump		Cylinder test	
ml pump	air %	water %	air %	water %
256,7	0	100	0	100
163,9	36,14	63,86	15,75263	84,24737
167,1	34,91	65,09	13,73955	86,26045
183,9	28,35	71,65	7,966858	92,03314
220,4	14,15	85,85	3,34672	96,65328
256,7	0,00	100,00	0	100
249,3	0,00	100,00	0	100
155,1	37,79	62,21	14,75797	85,24203
158,4	36,46	63,54	13,22115	86,77885
166,2	33,32	66,68	11,08374	88,91626
160,0	35,82	64,18	14,25178	85,74822
181,2	27,30	72,70	6,476684	93,52332
209,2	16,07	83,93	3,669113	96,33089

Figure F.2: Raw data from the peristaltic pump in the cylinder

Besides the data not being reliable the peristaltic hose pump had accuracy issues. When the stagnant water test was repeated multiple times for the same speed setting it returned different water volumes. The peristaltic pump in the experimental set-up was turned on for a constant amount of time, which was then compared to the zero measurement taken from stagnant water. During the bubble pipe test, when the peristaltic pump data were verified the time needed for 50 rotations was determined multiple times. The time needed differed between 19 to 22 seconds. Making the peristaltic hose pump unreliable and the data not usable.

G

Sand particle properties

Figure G.1 shows the sieve size and the percentage of sand that passes through it. Figure G.2 shows the diameters of the sand sample that was tested.

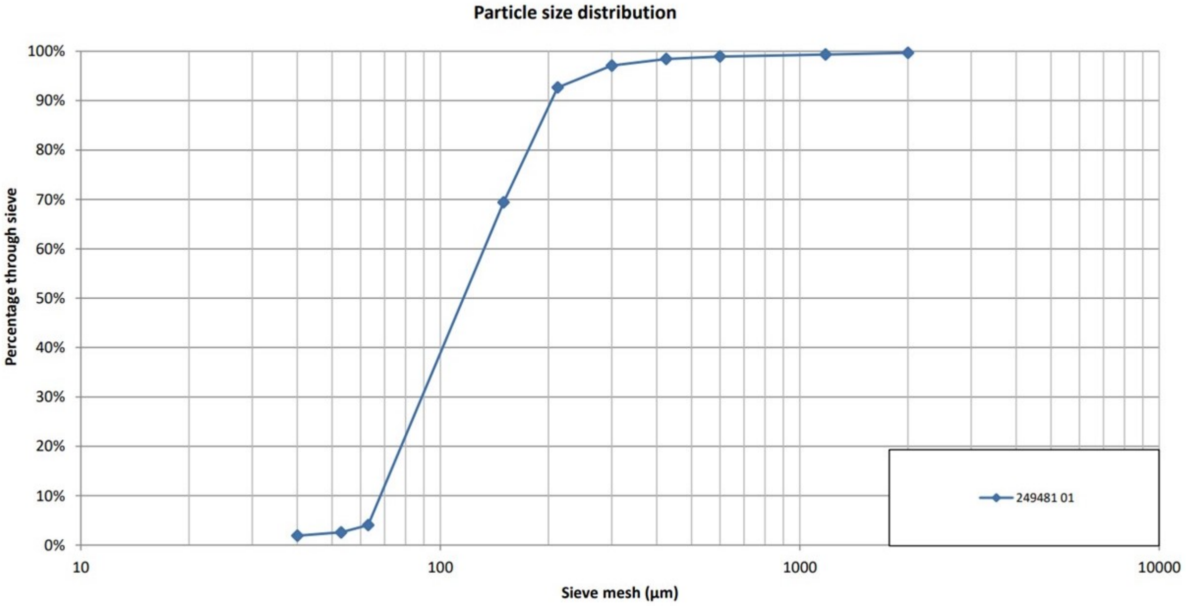

Figure G.1: Sieve size and percentage sand passed through

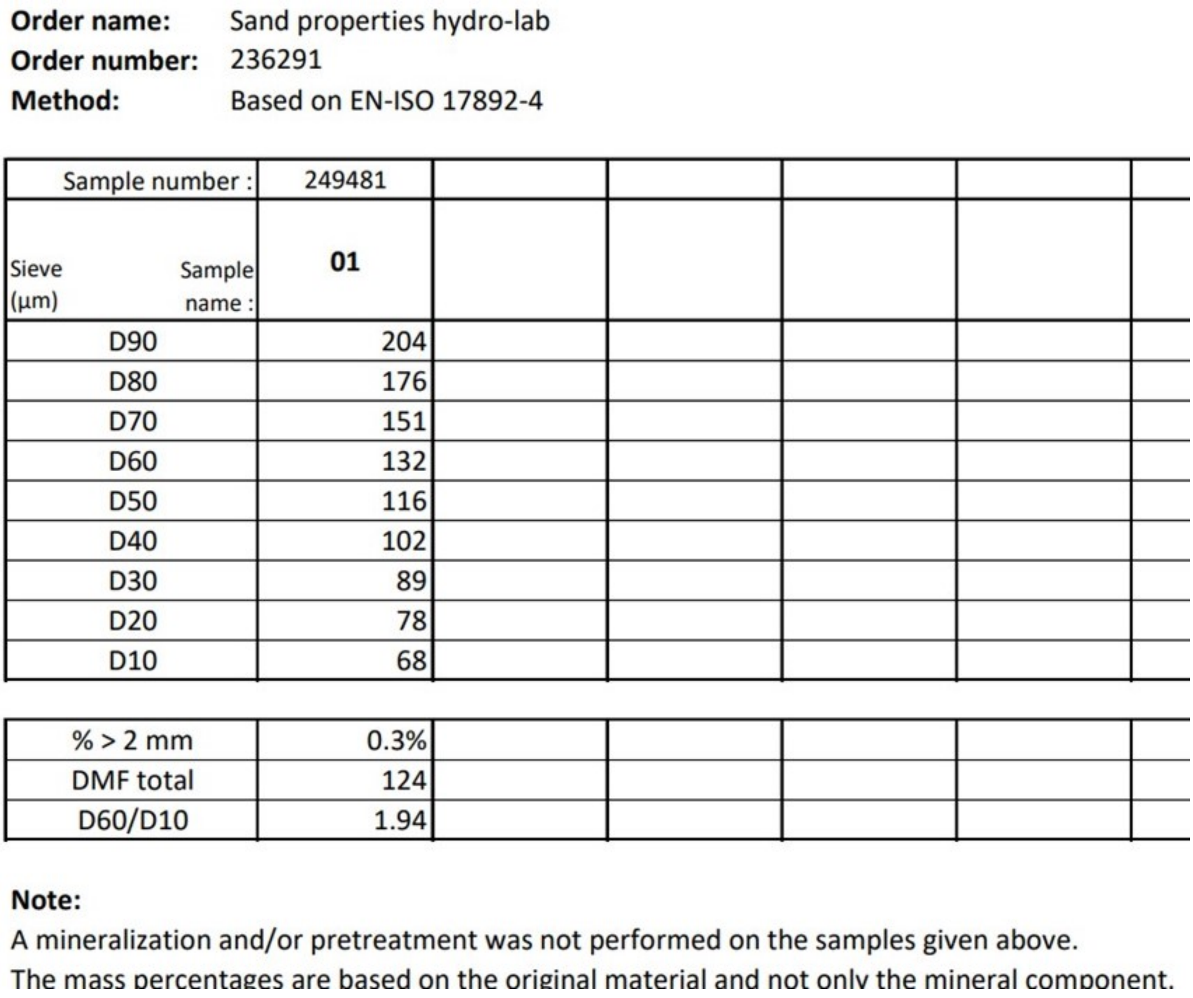

Order name: Sand properties hydro-lab
Order number: 236291
Method: Based on EN-ISO 17892-4

Sample number :	249481					
Sieve (µm) Sample name :	**01**					
D90	204					
D80	176					
D70	151					
D60	132					
D50	116					
D40	102					
D30	89					
D20	78					
D10	68					

% > 2 mm	0.3%					
DMF total	124					
D60/D10	1.94					

Note:
A mineralization and/or pretreatment was not performed on the samples given above.
The mass percentages are based on the original material and not only the mineral component.

Figure G.2: Sand diameter

H

Visual diameter approximations

Figure H.1 gives the estimated diameter at the distances from the nozzle.

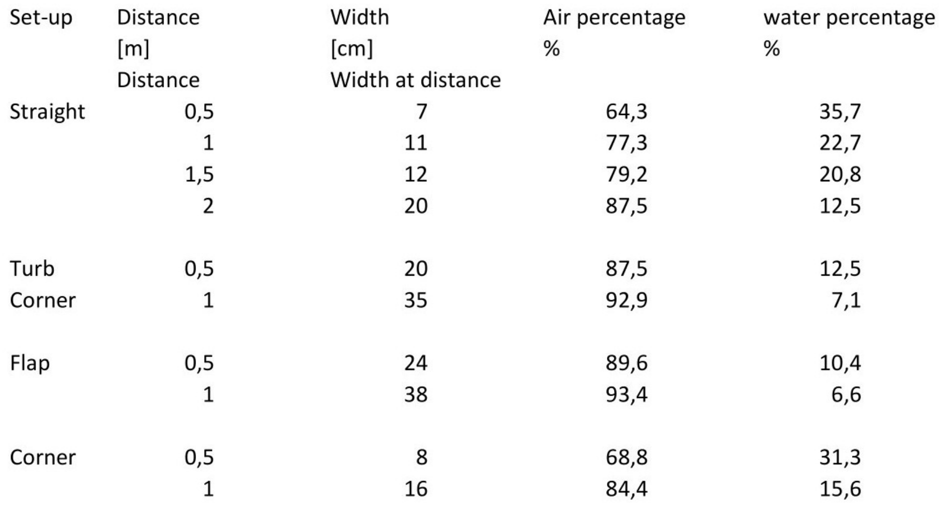

Set-up	Distance	Width	Air percentage	water percentage
	[m]	[cm]	%	%
	Distance	Width at distance		
Straight	0,5	7	64,3	35,7
	1	11	77,3	22,7
	1,5	12	79,2	20,8
	2	20	87,5	12,5
Turb	0,5	20	87,5	12,5
Corner	1	35	92,9	7,1
Flap	0,5	24	89,6	10,4
	1	38	93,4	6,6
Corner	0,5	8	68,8	31,3
	1	16	84,4	15,6

Figure H.1: Visual diameters

Figure H.2 shows four images of the straight jet set up at a distance of 0.5, 1, 1.5 and 2 meters distance in the direction of the jet.

(a) $0.5m$ from the nozzle in the direction of the jet

(b) $1m$ from the nozzle in the direction of the jet

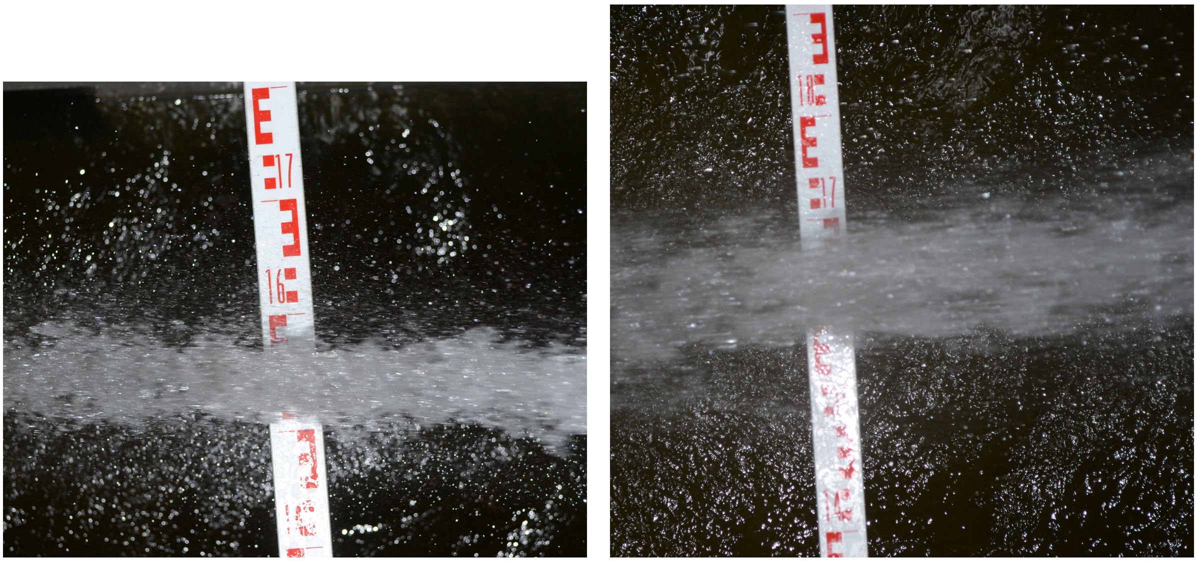

(c) $1.5m$ from the nozzle in the direction of the jet

(d) $2m$ from the nozzle in the direction of the jet

Figure H.2: Jet diameter from the straight set-up at four different distances

I

Bubble pipe test

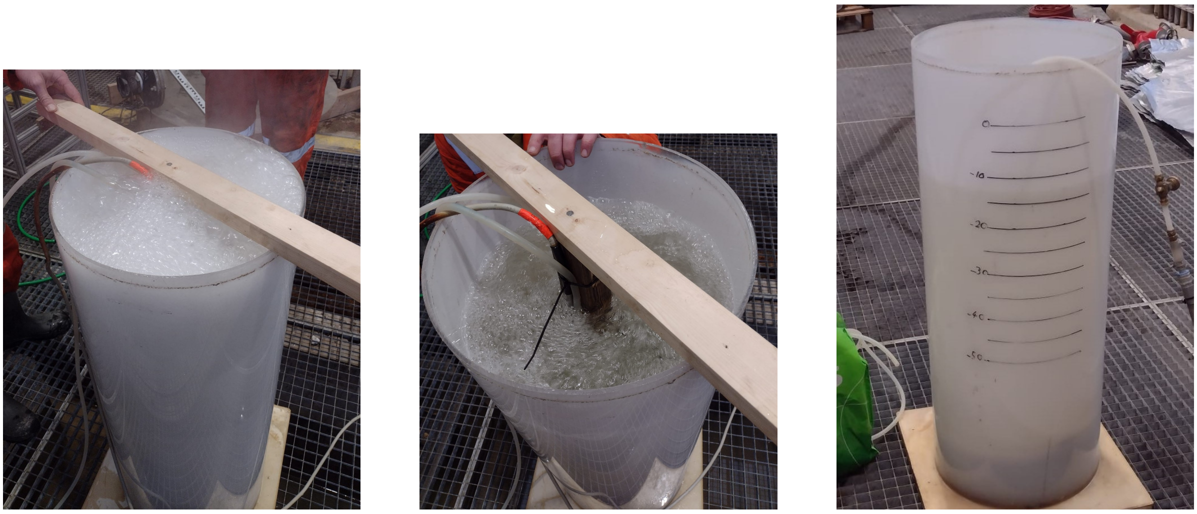

(a) Cylinder during a test

(b) Small amount of air in the cylinder

(c) The cylinder in rest

Figure I.1: Images of the bubble pipe test

For the cylinder test where the air was pumped into a known water volume the cylinder as shown in Figure I.1c was used. As visible in Figure I.1a more air is pumped into the water volume than was pumped in the cylinder in Figure I.1b. The conductivity rod is connected to a piece of wood together with the peristaltic pump to be able to connect the volume of water pumped with the voltage measured by the rod. This test was repeated multiple times with varying air concentrations to create the points used to calibrate the rods with conductivity sensors.

Figure I.2 shows the raw data from the cylinder test next to the same data in a graph. Where the x-axis shows the water percentage, between 80% to 100% and the y-axis shows the corresponding voltage percentage determined from the average volt measurements using the maximum and minimum value measured that day.

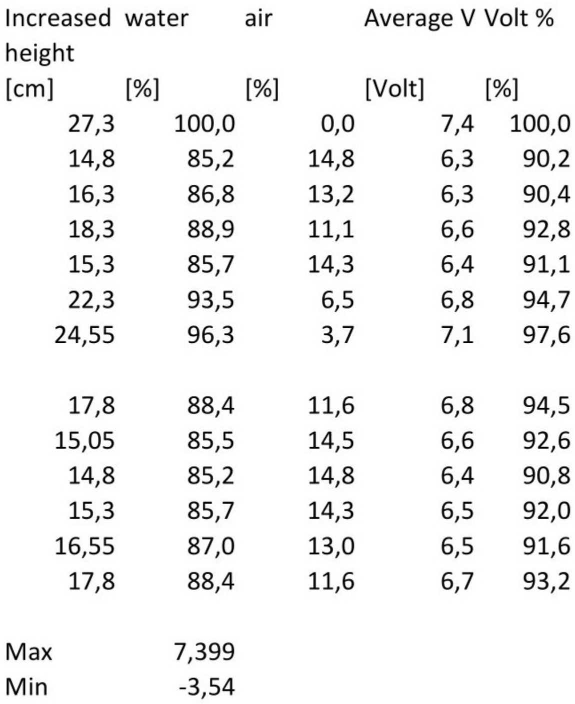

Increased height [cm]	water [%]	air [%]	Average V [Volt]	Volt % [%]
27,3	100,0	0,0	7,4	100,0
14,8	85,2	14,8	6,3	90,2
16,3	86,8	13,2	6,3	90,4
18,3	88,9	11,1	6,6	92,8
15,3	85,7	14,3	6,4	91,1
22,3	93,5	6,5	6,8	94,7
24,55	96,3	3,7	7,1	97,6
17,8	88,4	11,6	6,8	94,5
15,05	85,5	14,5	6,6	92,6
14,8	85,2	14,8	6,4	90,8
15,3	85,7	14,3	6,5	92,0
16,55	87,0	13,0	6,5	91,6
17,8	88,4	11,6	6,7	93,2
Max	7,399			
Min	-3,54			

(a) Raw data cylinder test

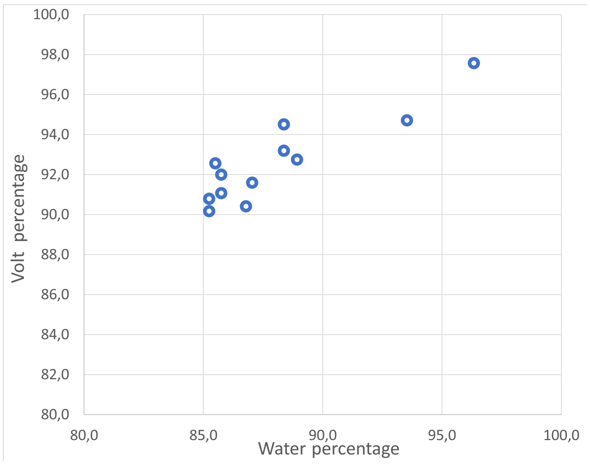

(b) Water percentage plotted against volt percentage

Figure I.2: Data from the cylinder test

J

Gravel test

The gravel used for the different gravel tests is shown in Figure J.2 with size decreasing from left to right. These gravels were first dried in an oven at 100 degrees Celsius for 24 hours to remove all the moisture and cooled before use to make sure the water temperature was not influenced by the temperature of the gravels. The idea of this test was comparable with the tests in the cylinder as shown in Appendix I. These rocks made it possible to measure water percentages that were not reachable using the cylinder tests.

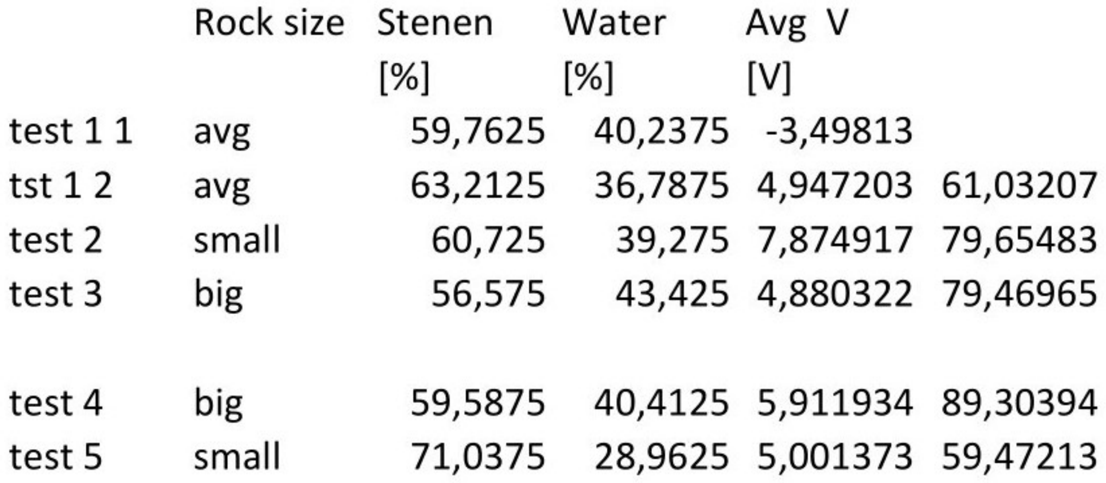

	Rock size	Stenen [%]	Water [%]	Avg V [V]	
test 1 1	avg	59,7625	40,2375	-3,49813	
tst 1 2	avg	63,2125	36,7875	4,947203	61,03207
test 2	small	60,725	39,275	7,874917	79,65483
test 3	big	56,575	43,425	4,880322	79,46965
test 4	big	59,5875	40,4125	5,911934	89,30394
test 5	small	71,0375	28,9625	5,001373	59,47213

Figure J.1: Raw data gravel tests

(a) Largest gravel size

(b) Medium gravel size

(c) Smallest gravel size

Figure J.2: Rocks used for the gravel tests

K

Bubble size image

As mentioned the bubbles visible in the cylinder all had roughly the same sizes. Figure K.1 shows an underwater picture during the test where the same can be seen for the inclined plunging jet.

Figure K.1: Still image of bubbles during testing

L

High speed imaging

Figure L.1 gives the first three and the last images used in the high speed imaging. The distance covered was 0.799m in 29 frames. The used camera had an fps of 960 frames per second. Which resulted in a velocity of 26.45 m/s

(a) 1st frame

(b) 2nd frame

(c) 3rd frame

(d) 29th (last) frame

Figure L.1: Four frames from the high speed imaging

Figure L.2 shows the raw data used for the points of high speed imaging in the data sets. For both the distances of 1.9 and 2.3 meter.

Distance: 1,9

Air [%]	Water [%]	Avg Volt {V}	Volt [%]
95,1	4,87	-2,63	7,0
79,7	20,33	-0,67	18,9
65,3	34,65	4,81	57,4
82,1	17,94	-0,85	17,5
96,1	3,86	-2,99	4,6
99,6	0,45	-3,12	2,5
100,0	0,04	-3,20	2,0
99,5	0,48	-2,93	4,9
88,7	11,32	-1,48	13,8
75,9	24,11	0,12	25,5
72,3	27,66	0,34	26,4
90,1	9,85	-2,03	11,4
98,6	1,43	-3,25	3,8
99,9	0,12	-3,10	2,4
100,0	0,00	-2,99	2,6
98,9	1,11	-2,79	4,9

(a) Raw data high speed imaging 1.9 m

Distance: 2.3

Air [%]	Water [%]	Avg Volt {V}	Volt [%]
93,1	6,9	-2,7	6,5
80,8	19,2	-0,9	17,3
71,9	28,1	5,4	61,6
82,4	17,6	-0,3	21,0
94,1	5,9	-3,0	4,3
98,8	1,2	-3,1	2,6
99,9	0,1	-3,2	2,3
98,7	1,3	-2,9	4,9
91,9	8,1	-2,7	5,3
83,1	16,9	-0,7	20,0
71,8	28,2	0,7	29,0
82,1	17,9	-0,9	19,0
94,0	6,0	-3,0	5,3
98,8	1,2	-3,0	2,8
100,0	0,0	-2,9	3,4
99,0	1,0	-3,0	3,4

(b) Raw data high speed imaging 2.3 m

Figure L.2: Raw data high speed imaging

M

Conductivity sensor factor clarification

The factor applied was found after determining the velocity and volumetric flow rate of a the jet at a distance of $2.3m$ from the jet nozzle in jet traveling direction. The pressure measured using the pitot tube and the water percentage are shown in Figure M.1. The water percentage was determined using the measured pressure and the constant velocity of $26,8m/s$ determined using the high speed images.

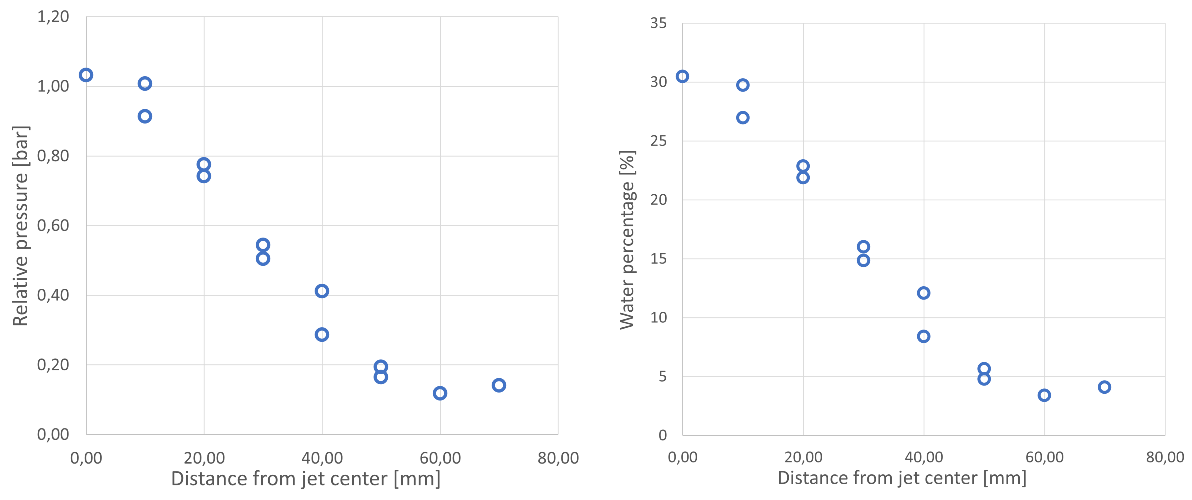

(a) Relative pressure

(b) Water percentage

Figure M.1: Pressure and water percentage of jet

When using the visually determined water velocity and the pressure measured by the pitot tube the water percentage can be determined. When this was done for the entire width of the jet and used to calculate the volumetric flow rate of the jet it turned out to be much higher than the volumetric flow rate at the nozzle. Figure M.2a gives the water percentage according to Archie's law as a function of the distance of the jet center.

Figure M.2a has most of the measurement points on the trend line, with the first one being a large outlier. This point is significantly far of the other points that it is most likely a measurement fault.

Taking the diameter of the jet the water percentage could be plotted for certain distances from the jet center, as shown in Figure M.2a. Integrating the water percentage over the surface area of the ring around the jet allowed for the calculation of the volumetric flow rate over the entire surface of the jet. The surface areas with the corresponding water percentages can be integrated to find the total water volume over the entire jet surface, where the outer edges weighed heavier, since the surface area was larger there. Calculating the flow rate using these water percentages and surface areas resulted in a significant overestimation of the volumetric flow rate of the jet, where the surface underneath this plotted line corresponded to a volumetric flow rate of $142\ \frac{m^3}{hr}$. The volumetric flow rate at the nozzle is

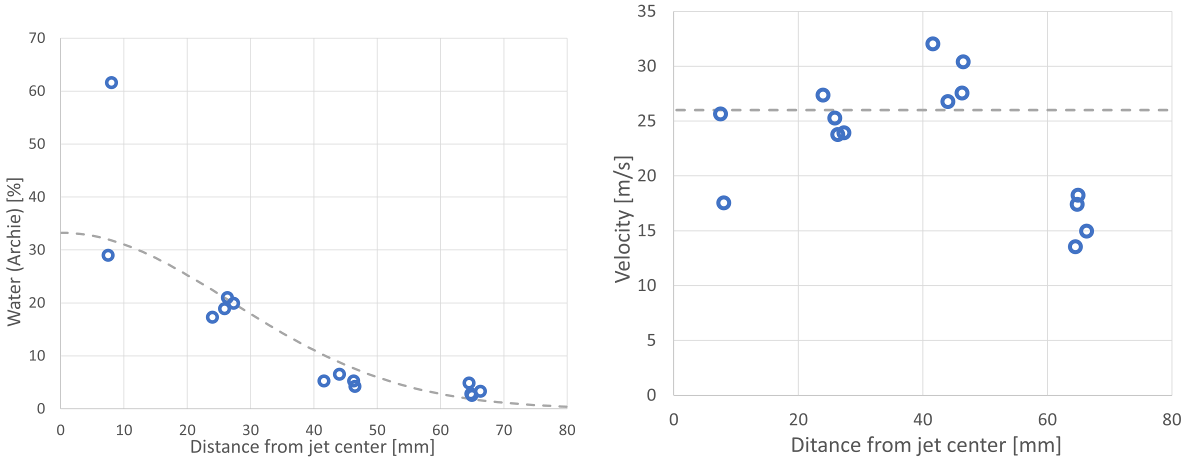

(a) Volumetric flow rate

(b) Velocity profile

Figure M.2: Graphs for the jet with no factor

known and should be constant over the length of the jet. With the calculated volumetric flow rate more than 3 times as large as the established volumetric flow rate of $41\ \frac{m^3}{hr}$ the possibility of a factor over the measurements was considered.

To have the calculated volumetric flow rate match the volumetric flow determined by the flow rate meter a factor had to be applied somewhere in the interpretation of the data. The pressure measured by the pitot tube was more likely to be inaccurate than the velocity according to the high speed imaging, due to possible pressure measure errors for the pitot tube while in air, as mentioned in Chapter 9. This is why a factor of 0.5 was applied to the pressure given by the pitot tube.

The calculated volumetric flow rate with this factor corresponds with the determined volumetric flow rate, where the graph for this is given in Figure M.3a. Where the surface area beneath the line matched the nozzle exit flow rate of $41\ \frac{m^3}{hr}$.

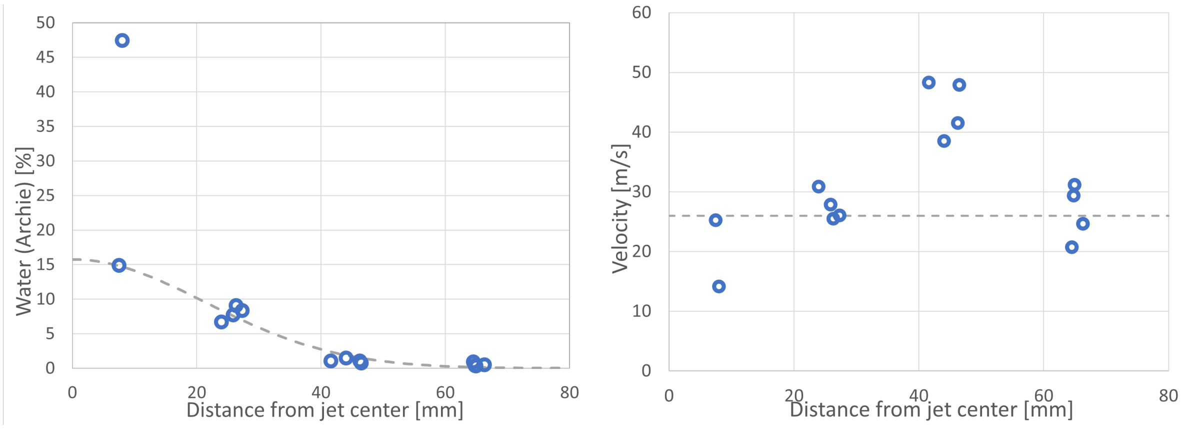

(a) Volumetric flow rate

(b) Velocity profile

Figure M.3: Graphs for the jet with a factor of 0.5

As shown in Figure M.3b the velocity calculated when this factor was applied was larger than the velocity when calculated without the factor. When comparing Figure M.3a and Figure M.3b it is noticeable that the velocity is significantly overestimated when the water percentage is low, 5% or less.

Without the factor the calculated volumetric flow rate did not match the determined volumetric flow rate, but the velocity was close to the theoretical data. The opposite was true for the calculation when the factor of 0.5 was included, where the volumetric flow rate matched but the velocity was somewhat overestimated. As was stated in this report at low water percentages the calculated voltage percentage interpretation could overestimate the velocity. For the calculations including the factor at the center, jet measurements were still relatively close to the $26,8\ \frac{m}{s}$, but became unreliable at further distances where the water percentages decreased below 5%.

N

Erosion graph data

The graph from Chapter 7.7 shows the production as a function of the vertical water depth. Where the functions of Winterwerp, van Rijn (2018), and Cheng are plotted. These functions are based on the points given in Figure N.1. The points here are not lined up, this is because the calculated production is determined from the water percentage and pressure. These two values were in the experiment not always accurately lined up with the theory. Figure N.2 shows the raw data used to calculate the van Rijn, Winterwerp, and Chang production.

$$v_e = \frac{E - S}{\rho_s(1 - n_0 - C_{nb})} \qquad E = \phi_p \rho_s \sqrt{g\Delta D} \tag{N.1}$$

Using the acquired data shown in Figure N.2 the velocity was calculated using the pressure and water percentage. With the pick-up functions of Van Rijn (2018), Winterwerp and Chang given in Formula N.2.

$$\phi_p = 0.00033 D_*^{0,3} \frac{1}{\theta}\left(\frac{\theta - \theta_{cr}}{\theta_{cr}}\right)^{1.5} \qquad \phi_p = 0.012 D_*^{0.3}(\theta^{0.5} - 1.3) \qquad \phi_p = 0.0001 D_*^{2.5}\left(F_* exp\left(-\frac{40}{F_*}\right)\right) \tag{N.2}$$

Where θ is the shields parameter, θ_{cr} is the critical shields parameter, according to [Brownlie, 1981], D_* is the dimensionless particle parameter and F_* is the densiometric Froude number as shown in Formula N.3.

$$\theta_{cr} = 0.22 R_p^{0.6} + 0.06 \exp(-17.77 R_p^{-0.6}) \qquad \theta = \frac{\tau}{g(\rho_s - \rho_w)D} \qquad D_* = \sqrt[3]{\frac{\Delta g}{v^2}} D \qquad F_* = \frac{u}{\sqrt{\Delta f D}} \tag{N.3}$$

Where R_p is the particle Reynolds number,Δ is the specific density and τ is the shear stress, as shown in Formula N.4

$$R_p = \frac{D\sqrt{\Delta g D}}{v} \qquad \Delta = \frac{\rho_s - \rho_w}{\rho_w} \qquad \tau = \frac{f}{8}\rho_m u^2 \tag{N.4}$$

The values used to solve these equations and use the resulting pick-up functions in Formula N.1 are given in Table N.1. Where besides the constants the velocity and mixture density is shown to be the variables that change at increasing water depths. The velocity and water percentage are given in Figure N.2 and together with the formulas mentioned in this appendix result in the graph shown in Figure N.1.

Using these pick-up function values the erosion, E, was calculated which in turn resulted in the erosion velocity, ve, also shown in Formula N.1.

Where S is the settling flux and is taken as 0. To determine the volume of sand eroded during the 30 second erosion test a spherical erosion crater was assumed. Taking an initial radius for this sphere, which was chosen as equal to the nozzle radius of $1.25cm$, and adding the erosion velocity times the

	Symbol	Value	Unit
Gravitational Acceleration	G	9.81	$[m/s^2]$
Density Sand	ρ_s	1522	$[kg/m^3]$
Density Water	ρ_w	1000	$[kg/m^3]$
Particle Diameter	D	0.000116	$[m]$
Friction Factor	f	0.03	[-]
Kinematic Viscosity	v	10^{-6}	$[m^2/s]$
Bed Porosity	n_0	0.4	[-]
Near Bed Concentration	c_{nb}	0	[-]
Time	t	30	$[s]$
Initial Radius	r_i	0.0125	$[m]$
Velocity	u	Variable	$[m/s]$
Mixture Density	ρ_m	Variable	$[kg/m^3]$

Table N.1: Table containing the constants used for the production calculations

time resulted in an estimation for the size of the radius of the resultant crater. The volume of this crater is calculated using the formula for the volume of a sphere times 0.5. The production per second is taken as the volume divided by the erosion times, which in this case is 30 seconds, as shown in Formula N.5.

$$r_r = r_i + v_e t \qquad 0.5V_{sphere} = \frac{2}{3}\pi r_e^3 \qquad P = \frac{0.5V_{sphere}}{t} \tag{N.5}$$

Where r_r is the resulting radius, r_i is the initial radius and P is the production.

As mentioned in Chapter 3.9 the friction factor was determined through a Moody diagram by use of the relative roughness and the Reynolds number, which resulted in a friction factor of 0.03.

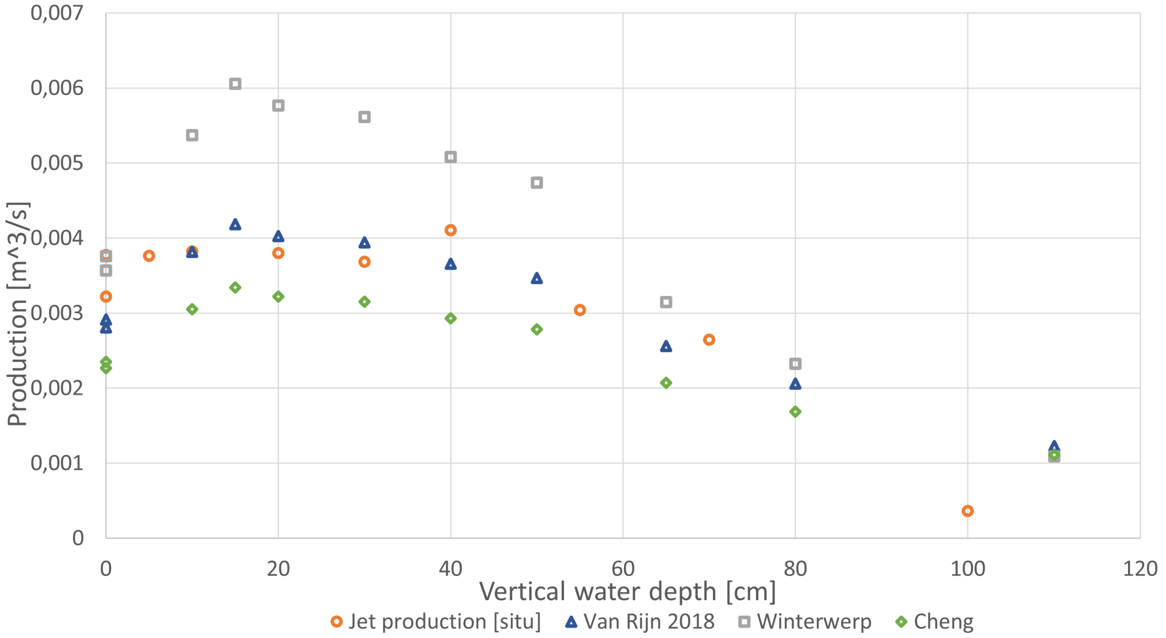

Figure N.1: Jet production at increasing water depths

The calculated points in Figure N.1 first move slightly upwards before they start decreasing. This can be verified with the raw data in Figure N.2. It is likely that the increase is due to the first few measurements being above water due to the air sheath forming around the jet and pitot tube and the actual waterline penetration of the jet is not at the 0 mark but later, as shown in Figure 5.1c. The pitot tube likely measures different in water and air making the transition between the two somewhat unclear, as discussed in Chapter 9.

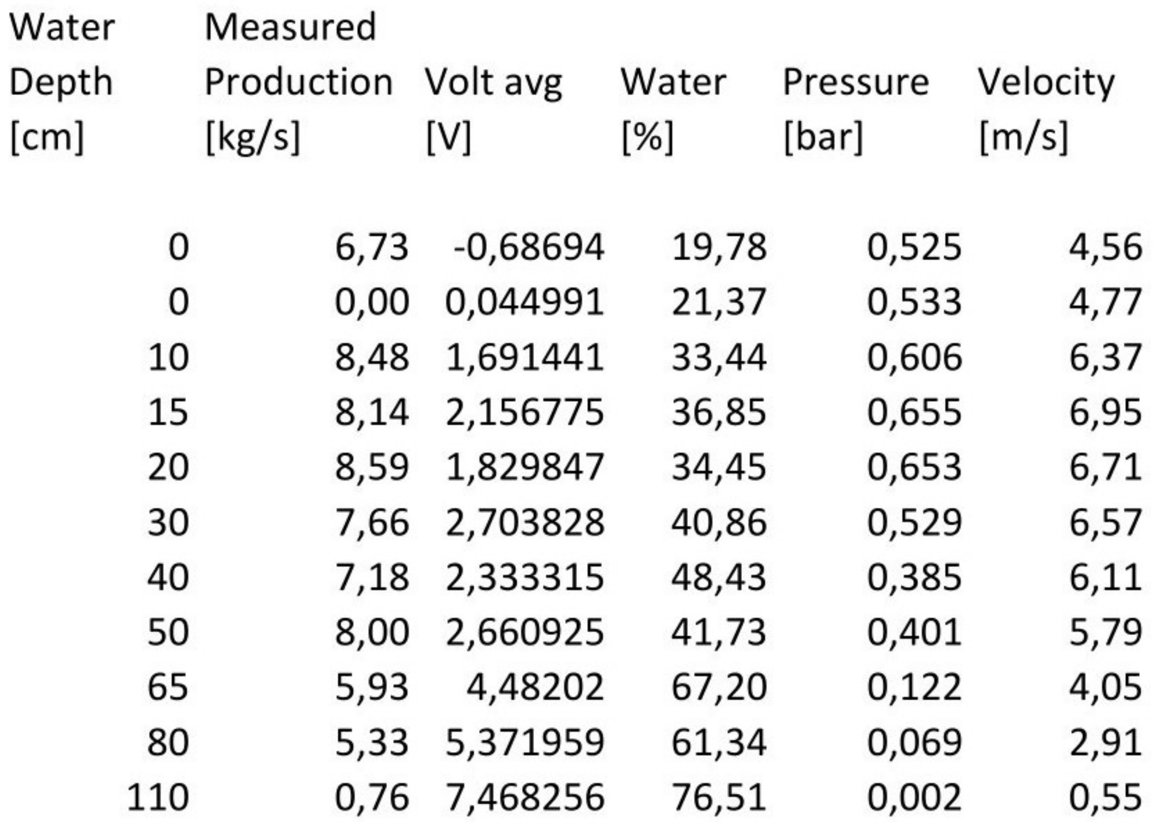

Water Depth [cm]	Measured Production [kg/s]	Volt avg [V]	Water [%]	Pressure [bar]	Velocity [m/s]
0	6,73	-0,68694	19,78	0,525	4,56
0	0,00	0,044991	21,37	0,533	4,77
10	8,48	1,691441	33,44	0,606	6,37
15	8,14	2,156775	36,85	0,655	6,95
20	8,59	1,829847	34,45	0,653	6,71
30	7,66	2,703828	40,86	0,529	6,57
40	7,18	2,333315	48,43	0,385	6,11
50	8,00	2,660925	41,73	0,401	5,79
65	5,93	4,48202	67,20	0,122	4,05
80	5,33	5,371959	61,34	0,069	2,91
110	0,76	7,468256	76,51	0,002	0,55

Figure N.2: Raw data from the erosion tests

O

Full graphs for all set-ups

The graphs in the report did not show some points that were deemed to be inaccurate or untrustworthy. Most notably due to low water percentages that resulted in unexpectedly high velocities, as can be seen in Figure O.1. The end bend had the most points that were left out in the report and shown here in the appendix. This is due to the edges of the jet having an unexpectedly high velocity from the measured water percentage and pressure.

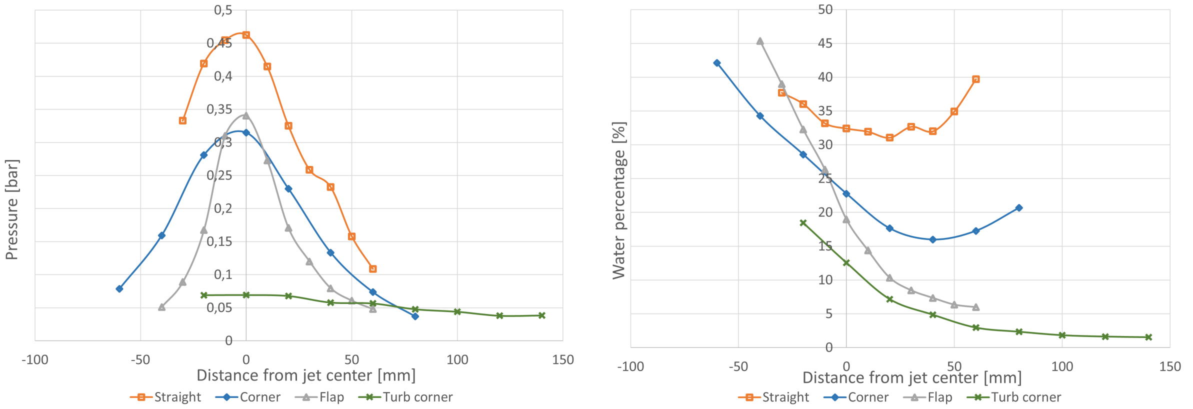

(a) Pressure profile (b) Water percentage profile

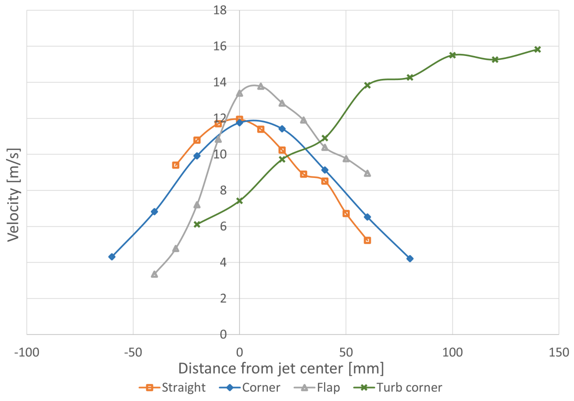

(c) Velocity profile

Figure O.1: Full jet profiles at a distance below water in direction of the jet

P

Non optimized velocity graphs

The velocity graphs shown in the report are optimized. Where the peak of the density and pressure graph are placed on top of each other for the resulting velocity graph. Th graphs shown in Figure P.1 are the result when the pressure and density from the same measurement location are used to calculate the velocity graph. Most notably for the straight set-up velocity profile above water, given in Figure P.1a. This one has a kind of wave where the left part likely underestimates the velocity and the right segment overestimates it, since the velocity was determined to be around $26,8m/s$ using high speed imaging.

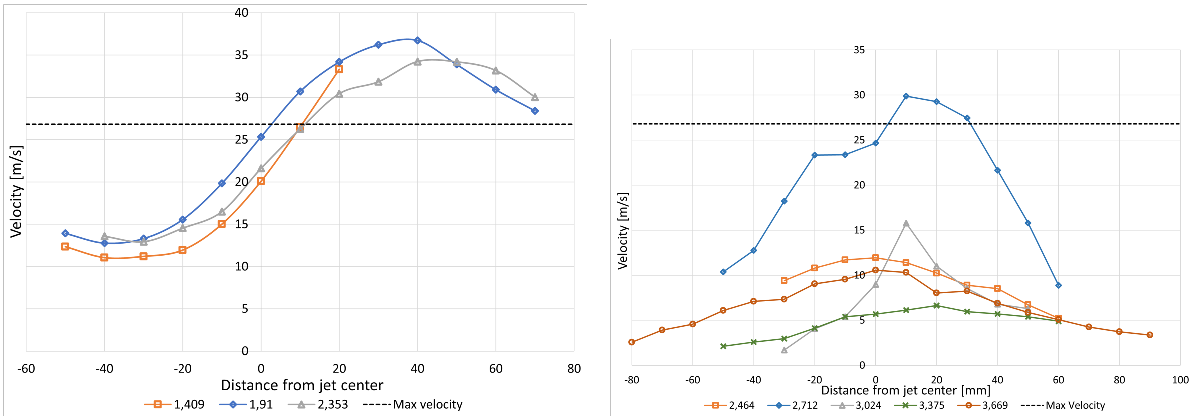

(a) Velocity profile above water

(b) Velocity profile below water

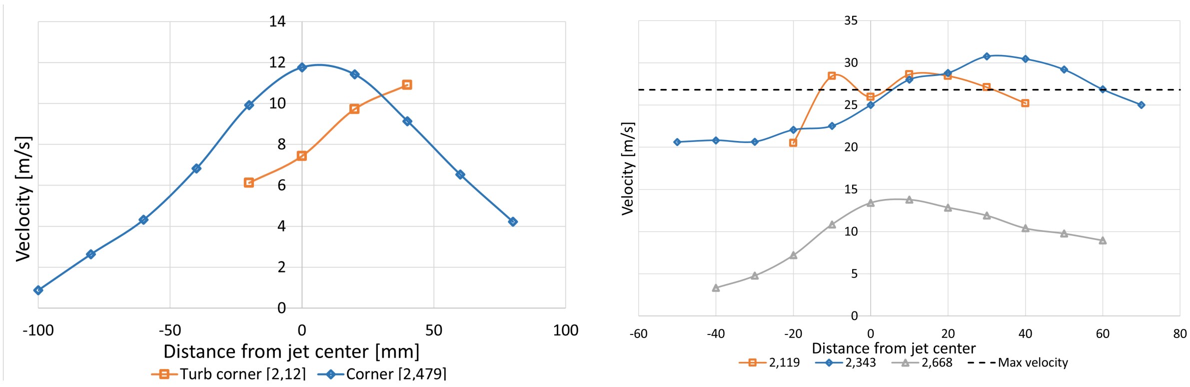

(c) Velocity profile bends

(d) Velocity profile flap

Figure P.1: Velocity profile without moved percentage profile

Q

Pictures of the jet in the air

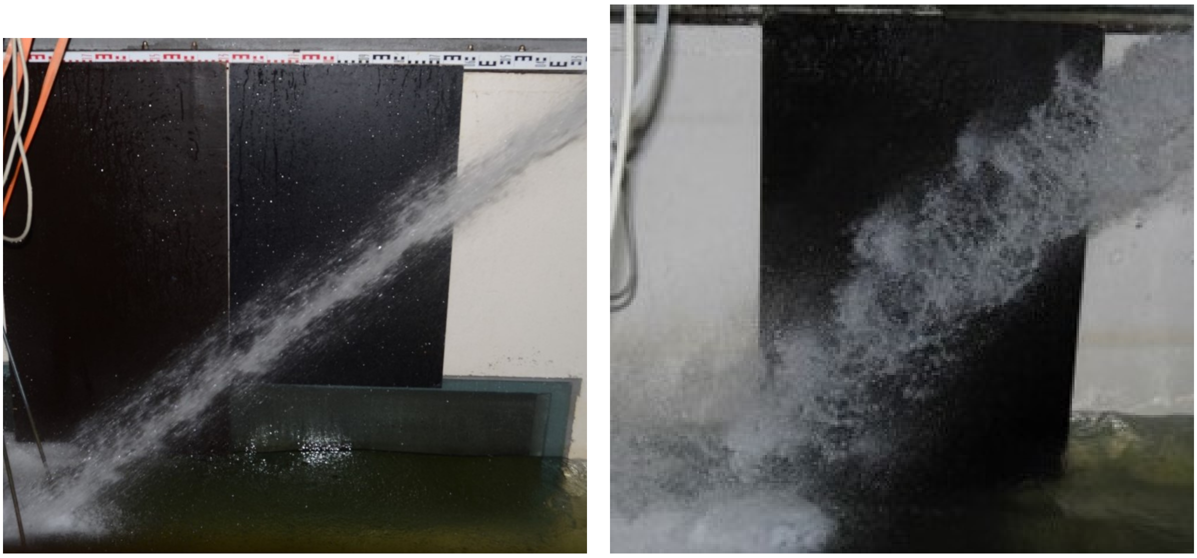

(a) Straight

(b) Middle bend

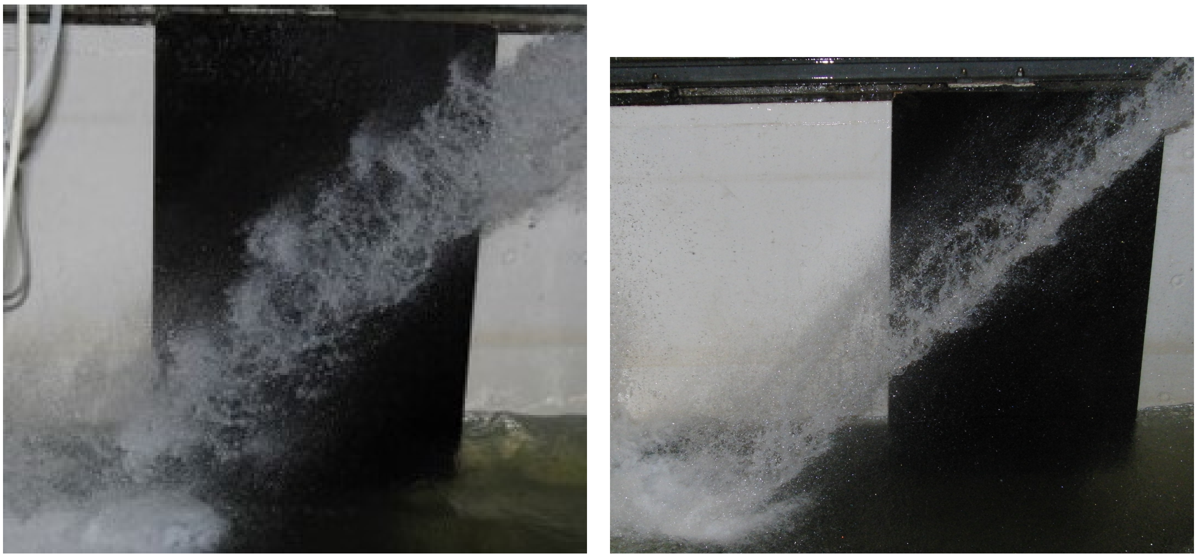

(c) End bend

(d) Flap

Figure Q.1: Side view from the four jet set-ups

In Figure Q.1 high shutter speed images of the four different jet set-ups are shown. The black boards behind the jet were placed there to increase the contrast and make the jet more visible when looking at it. Here the air entrainment into the jet is visible and shows how there is much more air in the end bend set-up jet, Figure Q.1c, than in the straight jet, Figure Q.1a. What is somewhat less visible is the flatness of the jet with the flap attached to the nozzle, Figure Q.1d. The other three jets were roughly circular, but the jet with the flap was significantly flatter due to the flap pushing the water jet down. From these pictures, it looks like the flap is somewhat comparable to the set-up with the middle bend, which was not the case.

R

Full graph both bend set-ups

The graphs in the report did not show some points that were deemed to be inaccurate or untrustworthy. Most notably due to low water percentages that resulted in unexpectedly high velocities. Here the profiles from Chapter 7.4 are plotted with the initially removed segments. As visible in FigureR.1 the low water percentage with a low-pressure results in high velocities at the edges of the jet, which is highly unlikely.

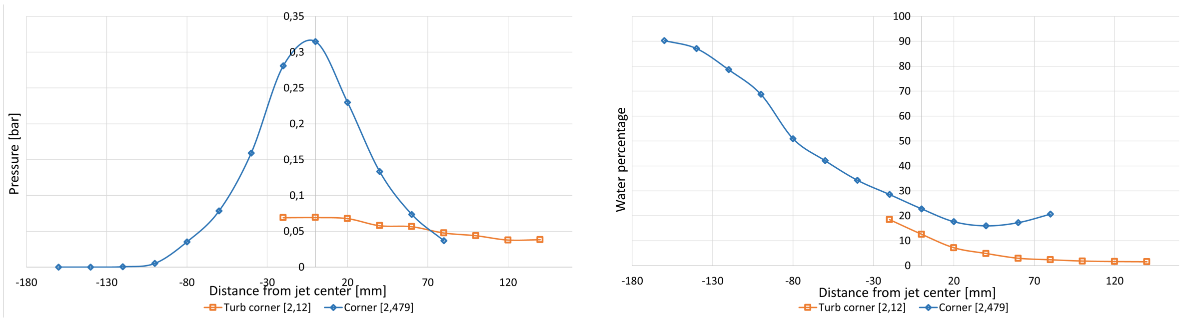

(a) Pressure profile

(b) Water percentage profile

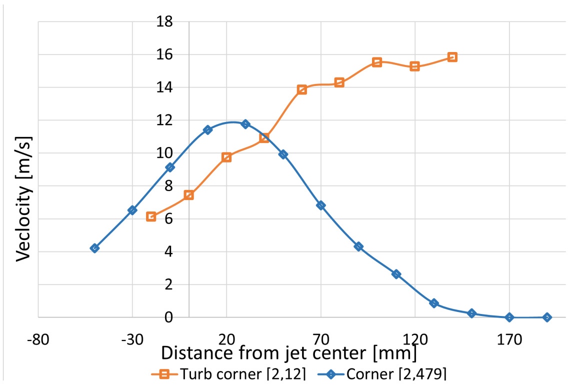

(c) Velocity profile

Figure R.1: Full graphs for the bend set-ups above water

S

Pictures of the nozzles

As visible in Figure S.1 the nozzle is not entirely concentric but has a small straight part at the end. This most likely also somewhat influenced the jet at the nozzle exit. In this figure, the jet at the exit of the nozzle is shown. It is visible that it influences the jet and its further trajectory. With the width increase of the straight, Figure S.1a, and middle bend, Figure S.1b, being somewhat comparable. The diameter of the jet from the end bend, Figure S.1c, increased after a small constant width. The flap, Figure S.1d, increased instantly due to the flap pushing down and flattening the jet right as it exits the nozzle.

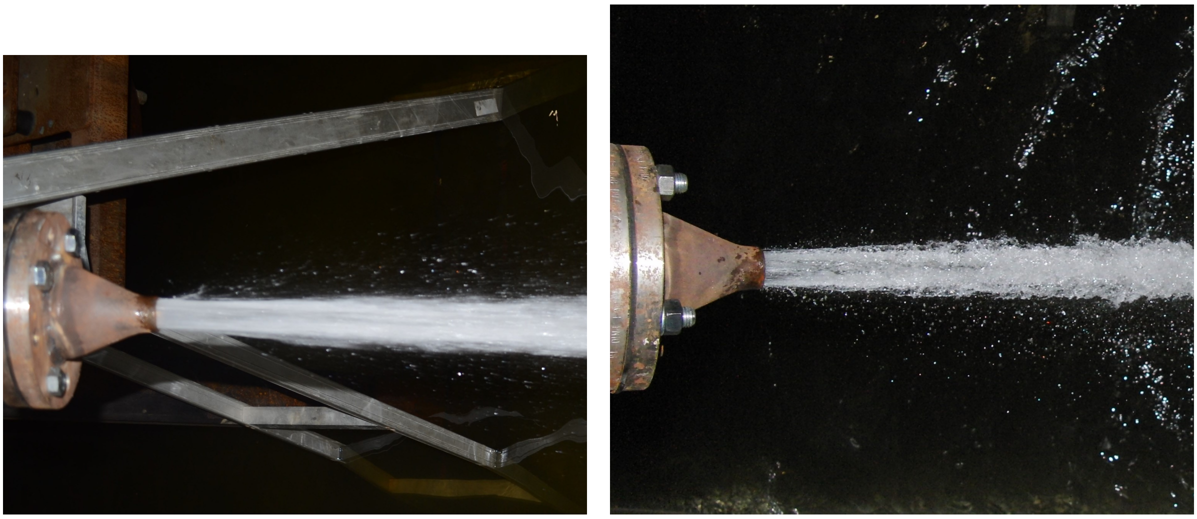

(a) Nozzle during the straight set-up

(b) Nozzle during the middle bend set-up

(c) Nozzle during the end bend set-up

(d) Nozzle during the flap set-up

Figure S.1: Close up from the nozzles during the four set-ups

Bibliography

Archie, G. E. (1942). The electrical resistivity log as an aid in determining some reservoir characteristics. *Transactions of the AIME*, *146*(01), 54–62.

Bhagat, R. K., Wilson, D. I., & Linden, P. (2020). Experimental evidence for surface tension origin of the circular hydraulic jump. *arXiv preprint arXiv:2010.04107*.

Biń, A. K. (1993). Gas entrainment by plunging liquid jets. *Chemical Engineering Science*, *48*(21), 3585–3630.

Brandt, M. J., Johnson, K. M., Elphinston, A. J., & Ratnayaka, D. D. (2016). *Twort's water supply*. Butterworth-Heinemann.

Brownlie, W. R. (1981). Prediction of flow depth and sediment discharge in open channels.

Chanson, H., Aoki, S., & Hoque, A. (2006). Bubble entrainment and dispersion in plunging jet flows: Freshwater vs. seawater. *Journal of Coastal Research*, *22*(3), 664–677.

Cheng, N., Wei, M., Chiew, Y., Lu, Y., & Emadzadeh, A. (2020). Combined effects of mean flow and turbulence on sediment pickup rate. *Water Resources Research*, *56*(2), e2019WR026181.

den Adel, H. (1987). Heranalyse doorlatendheidsmetingen door middel van de forch- heimer relatie. *Technical Report Techical Rep. No. CO-272550/56„ GeoDelft, Deltares, Delft, The Netherlands*.

Deshpande, S., & Trujillo, M. F. (2013). Distinguishing features of shallow angle plunging jets. *Physics of Fluids*, *25*(8), 082103.

Esmailizadeh, L., & Mesler, R. (1986). Bubble entrainment with drops. *Journal of colloid and interface science*, *110*(2), 561–574.

Grant, R. P., & Middleman, S. (1966). Newtonian jet stability. *AIChE Journal*, *12*(4), 669–678.

Heijmeijer, O. A., Nobel, A. J., Keetels, G., & Van Rhee, C. (2022). High-velocity erosion of sand. *Journal of Hydraulic Engineering*, *148*(5), 04022005.

Lewis, T., Abt, S. R., Wittler, F., & Annandale, G. (1999). Predicting impact velocities of developed jets. *Water international*, *24*(3), 255–265.

Lubking, P. (2000). Luchtinslag tijdens het beladen van een sleephopperzuiger. *Msc Thesis, Delft University of Technology*.

Maxwell, J. (1881). *A treatise on electricity and magnetism: Pt. iii. magnetism. pt. iv. electromagnetism* (Vol. 2). Clarendon press.

Morgan, M. N., & Baines-Jones, V. (2009). On the coherent length of fluid nozzles in grinding. *Key Engineering Materials*, *404*, 61–67.

Nobel, A. J. (2013). On the excavation process of a moving vertical jet in cohesive soil. *PhD, Delft University of Technology*.

Rajaratnam, N., & Albers, C. (1998). Water distribution in very high velocity water jets in air. *Journal of hydraulic engineering*, *124*(6), 647–650.

Roy, A., & Kumar, K. (2018). Experimental studies on hydrodynamic characteristics using an oblique plunging liquid jet. *Physics of Fluids*, *30*(12), 122107.

Smit, A. (2007). Air entrainment with plunging jets: Experimental study about air entrainment with free overfall jets from circular channels and air bubble intake with submersible pumps in sewer sumps. *Msc Thesis, Delft University of Technology, Civil Engineering and Geosciences, Hydraulic Engineering*.

Sun, Q., Yuan, H., Jiang, L., Xu, G., & Zhang, X. (2020). Numerical simulations of air cavities in inclined plunging jets. *Mathematical Problems in Engineering*, *2020*.

Talmon, A. (2011). Application of electrical resistance tomography in a sandslurry loop. *CEDA Dredging Days 2011: Dredging and Beyond, Rotterdam, the Netherlands-Proceedings 10-11 Nov*.

Tjaden, B., Cooper, S. J., Brett, D. J., Kramer, D., & Shearing, P. R. (2016). On the origin and application of the bruggeman correlation for analysing transport phenomena in electrochemical systems. *Current opinion in chemical engineering*, *12*, 44–51.

Trettel, B. (2020). Turbulent jet breakup: Theory and data. *PhD, Texas University at Austin*.

Van de Sande, E., & Smith, J. M. (1976). Jet break-up and air entrainment by low velocity turbulent water jets. *Chemical Engineering Science*, *31*(3), 219–224.

van de Sande, E. (1974). Air entrainment by plunging water jets. *PhD, Delft University of Technology*.

Van Rhee, C. (2010). Sediment entrainment at high flow velocity. *Journal of hydraulic engineering*, *136*(9), 572–582.

van Rijn, L. C., Bisschop, R., & Rhee, C. v. (2019). Modified sediment pick-up function. *Journal of Hydraulic Engineering*, *145*(1), 06018017.

Vinke, F. (2009). Water jets surrounded by an air film. *Msc Thesis, Delft University of Technology*.

Vlasblom, W. J. (2003). Designing dredging equipment. *Lecture notes (WB3408b)*.

Winterwerp, J. C., Bakker, W. T., Mastbergen, D. R., & van Rossum, H. (1992). Hyperconcentrated sand-water mixture flows over erodible bed. *Journal of Hydraulic Engineering*, *118*(11), 1508–1525.